Coherent Control of Ultracold Polar Molecules

GREGORY, PHILIP,DAVID

How to cite:

GREGORY, PHILIP,DAVID (2018) *Coherent Control of Ultracold Polar Molecules*, Durham theses, Durham University. Available at Durham E-Theses Online: http://etheses.dur.ac.uk/12484/

Coherent Control of Ultracold Polar Molecules

Philip David Gregory

This thesis presents the development of a toolbox for the coherent control of ultracold polar molecules. Such systems of molecules promise the creation of long-lived, highly dipolar quantum gases with applications spanning the fields of quantum state controlled chemistry, quantum information, quantum simulation, and precision measurement. However, the addition of vibrational and rotational degrees of freedom leads to molecular systems being significantly more complex than their widely used atomic counterparts. In this work we demonstrate full control of the quantum state down to the hyperfine level of an optically trapped sample of ultracold bosonic ^{87}Rb^{133}Cs molecules, and exploit that control to begin an investigation into the collision processes which take place in an ultracold molecular gas.

We create a sample of up to ~ 4000 optically trapped molecules in their rovibronic and hyperfine ground state. We characterise the molecules by measuring their temperature, binding energy, and molecule-frame electric dipole moment.

We perform spectroscopy of the first rotationally excited state with hyperfine state resolution using microwaves to determine accurate values of rotational and hyperfine coupling constants. We use coherent π pulses to perform complete transfer population between selected hyperfine levels of the ground, first-excited, and second-excited rotational states.

We investigate the effect of the off-resonant light of our optical dipole trap on the rotational and hyperfine structure of the molecules. Through a combination of high-resolution microwave spectroscopy and parametric heating measurements, we characterise the polarisability of the ^{87}Rb^{133}Cs molecule. We demonstrate that coupling between neighbouring hyperfine states manifests in rich structure with many avoided crossings in any rotational state other than the ground state. This coupling may be tuned by rotating the polarisation of the linearly polarised trapping light.

Finally, we study the lifetime of polar bosonic ^{87}Rb^{133}Cs molecules in our 3D optical dipole trap. We examine the lifetime of the molecules as a function of dipole trap intensity, magnetic field, and hyperfine and rotational state. Despite the chemical stability of the ^{87}Rb^{133}Cs molecule, we observe lifetimes of ~ 1 s corresponding to 2-body decay rates close to the universal limit.

Coherent Control of Ultracold Polar Molecules

Philip David Gregory

A thesis submitted in partial fulfilment
of the requirements for the degree of
Doctor of Philosophy

Department of Physics
Durham University

March 2017

Contents

Page

Abstract **i**

Contents **ii**

List of Figures **v**

List of Tables **vii**

Declaration **viii**

Acknowledgements **ix**

1 Introduction **1**
- 1.1 Why Cold Molecules? . . . 1
- 1.2 Creating Ultracold Molecules - An Overview . . . 2
- 1.3 Proposed Applications . . . 5
  - 1.3.1 Quantum Computing . . . 5
  - 1.3.2 Quantum Simulation . . . 7
  - 1.3.3 Precision Measurement . . . 9
- 1.4 Thesis Overview . . . 10
- 1.5 Publications . . . 12

2 Theory **14**
- 2.1 Choosing the Molecule - ^{87}Rb^{133}Cs . . . 14
- 2.2 Creating an Ultracold Atomic Mixture . . . 16
  - 2.2.1 Magnetic Levitation . . . 17
  - 2.2.2 Optical Trapping and Evaporation . . . 18
- 2.3 Magnetoassociation . . . 19
  - 2.3.1 Feshbach Resonances and Scattering Theory . . . 20
  - 2.3.2 Molecule Production on a Feshbach Resonance . . . 26
  - 2.3.3 Control of the Feshbach State . . . 27
- 2.4 Stimulated Raman Adiabatic Passage (STIRAP) . . . 29
  - 2.4.1 STIRAP in an Idealised 3-Level System . . . 29
  - 2.4.2 Efficiency of STIRAP . . . 31
- 2.5 Structure of Diatomic Molecules . . . 32

2.5.1 Hund's Cases and Electronic Structure 34
2.5.2 Vibrational Structure 36
2.5.3 Rotational and Hyperfine Structure 36
2.6 Polar Molecules 39
2.6.1 Polar Molecules in DC Electric Fields 40
2.6.2 Polar Molecules in Microwave Fields 42
2.6.3 Interacting Dipoles 43

3 Experimental Apparatus **46**
3.1 Vacuum System 46
3.2 Laser Systems 47
3.2.1 Cooling, Optical Pumping, and Imaging 48
3.2.2 Optical Trapping 49
3.2.3 STIRAP 53
3.3 Magnetic Fields 58
3.3.1 Magnetic Field Calibration 58
3.4 Electric Fields 60
3.5 Microwave Sources 65

4 Creation and Characterisation of Ultracold ^{87}Rb^{133}Cs **68**
4.1 Feshbach Association 69
4.2 Transfer to the Ground State 72
4.3 Imaging 77
4.4 Temperature 78
4.5 Binding Energy 80
4.6 Electric Dipole Moment 85
4.7 Summary 87

5 Coherent Control of the Rotational and Hyperfine State **88**
5.1 Quantum Numbers and Allowed Transitions 89
5.2 Spectroscopy of $N = 1$ 91
5.3 Coherent Population Transfer 100
5.4 Superpositions of Molecule States 104
5.5 Summary 109

6 Polarisability, Trapping, and the AC Stark Effect **110**
6.1 The AC Stark Effect in Molecules 111
6.2 Anisotropic Component of Polarisability $\alpha^{(2)}$ 114
6.3 Isotropic Component of Polarisability $\alpha^{(0)}$ 118
6.4 Tuning Avoided Crossings and Experimental Considerations . 119
6.5 Summary 122

7 Lifetimes and Collisions of Ultracold Molecules **124**
7.1 Collision Processes Between Ultracold Molecules 125
7.1.1 Sticky Collisions 127
7.2 Experimental Measurements of Molecule Loss 129

7.2.1 Dependence on Optical Trap Laser Intensity 131
7.2.2 Magnetic Field Dependence in $N = 0$ 132
7.2.3 Lifetime in a Range of Rotational and Hyperfine States 134
7.3 Collisions Between Atoms and Molecules 135
7.4 Summary 136

8 Conclusion 137
8.1 Summary 137
8.2 Outlook 139
8.2.1 Optical Lattices 139
8.2.2 Other Bialkali Species 140
8.2.3 Optical Tweezers 141
8.2.4 Molecular Quantum Gas Microscope 142
8.3 Concluding Remarks 145

A Collision Heating Rates 146

Bibliography 148

List of Figures

Figure Page

1.1 Overview of method to produce ultracold molecules 4
1.2 Proposed apparatus for quantum computation 6
1.3 Mott insulator ordering on a 2D lattice 8

2.1 Potential wave barrier and scattering length tunability. 21
2.2 Scattering lengths for Rb-Rb, Cs-Cs, and Rb-Cs collisions . . 24
2.3 Association and dissociation scheme 26
2.4 Near-threshold ^{87}Rb^{133}Cs molecular states. 27
2.5 Configuration and pulse sequence for STIRAP 30
2.6 Overview of molecule energy levels 33
2.7 Hund's cases relevant to ^{87}Rb^{133}Cs 35
2.8 Hyperfine and Rotational Zeeman Structure of ^{87}Rb^{133}Cs . . . 38
2.9 Stark map for rigid rotor polar molecule. 42
2.10 Dipole moment in the rigid rotor model. 43
2.11 Theory for two interacting dipoles 44

3.1 Vacuum system 47
3.2 Energy level scheme for the D$_2$ lines in ^{87}Rb and ^{133}Cs atoms . 48
3.3 Dipole trapping and STIRAP optical layout 50
3.4 Measurement of dipole trap beam crossing angle 51
3.5 Measurement of trap frequency in the optical trap 52
3.6 Molecular transitions for STIRAP 54
3.7 STIRAP laser system schematic 55
3.8 STIRAP pulse sequence control scheme 57
3.9 Breit Rabi diagrams for ground state ^{87}Rb and ^{133}Cs atoms . . 59
3.10 Magnetic field calibration example 60
3.11 Electrode array for DC electric fields 61
3.12 Simulating the electric potential across the cell 62
3.13 Switching of high voltages 63
3.14 980 MHz $\lambda/4$ monopole antenna design 66

4.1 Feshbach association sequence 69
4.2 Stern-Gerlach separation of atoms and molecules 70
4.3 Transfer between levitated and unlevitated traps 71
4.4 One- and two-photon spectroscopy of STIRAP transitions . . 73

4.5 STIRAP transfer to the rovibronic ground state 75
4.6 Rabi oscillations on pump and Stokes transitions 76
4.7 In-situ absorption images of dissociated molecules 77
4.8 Time of flight expansion of atoms 79
4.9 Time of flight expansion of molecules 81
4.10 Referencing STIRAP light to the optical frequency comb . . . 82
4.11 Binding energy measurement scheme 83
4.12 Electric dipole moment of ^{87}Rb^{133}Cs 86

5.1 Coherent population transfer scheme and selection rules 90
5.2 Early microwave spectroscopy results 92
5.3 Fourier-transform limiting of Microwave Spectroscopy 93
5.4 Microwave Spectroscopy of $N = 1$ at 181.5 G 94
5.5 Zeeman shift of transition frequencies $N = 0$ and $N = 1$ 95
5.6 Changing the hyperfine state in $N = 0$ 101
5.7 Transfer of molecules between $N = 0, 1$ and 2 102
5.8 Two-photon transfer of molecules between $N = 0$ and 2 103
5.9 Superposition of states from short microwave pulses 105
5.10 Loss of contrast in Rabi oscillations 106
5.11 Ramsey spectroscopy on the Bloch sphere 107
5.12 Ramsey interferometry between two rotational levels 108

6.1 Coordinate system for AC Stark effect measurements 112
6.2 AC Stark shift of $N = 0$ to 1 transitions for $\beta = 90°$ 114
6.3 AC Stark shift of $N = 0$ to 1 transitions for $\beta = 0°$ 115
6.4 Dependence of AC Stark shift on laser polarisation 117
6.5 Measurement of the isotropic component of polarisability . . . 118
6.6 Parametric heating to determine isotropic polarisability 119
6.7 Tuning avoided crossings by varying laser polarisation 120
6.8 Effect of magnetic field on AC Stark shift 121

7.1 Formation of molecular collision complexes 127
7.2 Example lifetime results for molecules in $N = 0$ 129
7.3 Dependence of molecule loss rate on trap laser intensity 131
7.4 Dependence of the molecule loss rate on magnetic field 133
7.5 Lifetimes in a range of rotational and hyperfine states 134

8.1 Design of molecule tweezer experiment 142
8.2 Typical Quantum Gas Microscope Apparatus 143
8.3 Molecular microscope trapping scheme 144

List of Tables

2.1 Comparison of bialkali dimers. 15
2.2 Magnetic Moments and Levitation Gradients 18
2.3 Rigid rotor probability distribution. 40

4.1 Example calculation of binding energy 84

5.1 Microwave transition frequencies between $N = 0$ and $N = 1$. . . 96
5.2 Fitted molecular constants for ^{87}Rb^{133}Cs 97
5.3 State composition of relevant $N = 0$ hyperfine states 98
5.4 State composition of relevant $N = 1$ hyperfine states 99

Declaration

I confirm that no part of the material offered has previously been submitted by myself for a degree in this or any other University. Where material has been generated through joint work, the work of others has been indicated.

Philip David Gregory

Durham, November 2017

Acknowledgements

The work presented in this thesis is the culmination of 4 years of running and maintaining a complex and sophisticated apparatus, which would never have been possible without the fantastic team of students and researchers whom have worked on or around the project both past and present. In particular I must thank my supervisor, Simon Cornish, for his guidance and support. Simon's attention to detail and enthusiasm for his work have been an inspiration. I am hugely grateful for the opportunities which he has given me, and without him, none of this would have been possible.

I would like to thank the many members of the RbCs team, especially my fellow PhD student Pete Molony. His prowess and understanding of experimental physics was critical in getting the experiment to where it is today. In addition, he along with Michael Köppinger, Bo Lu and Zonghua Ji gave me the best introduction to the experiment possible, and I am indebted for all of their hard work and patience. I must also thank Avinash Kumar for his time on the project, working with Pete and I on optimising and characterising the ground state transfer. I am sure that the experiment is now left in good hands, with new PhD student Jake Blackmore and post docs Liz Bridge and Rahul Sawant.

The rest of 'Cornish Division' have been equally invaluable. Steve Hopkins has been a huge help in all things technical, while Anna Marchant was always willing to solve problems regardless of how many times per day I had to knock on the door to the Solitons lab! The current group of Ana Rakonjac, Alex Guttridge, Oliver Wales, Dani Pizzey, Mew Ratkata, Prosenjit Majumder, and Zenghkun Fu have all been of great help, not least in the creation of some really delicious baked goods. I would also like to thank in particular Stefan Kemp and Kirsteen Butler for my time with them in the YbCs lab, and their teaching me the ropes as a summer student.

The whole of AtMol has been fantastic, always providing a friendly and supportive place to work. Furthermore, I am extremely grateful to Steve Lishman and the rest of the mechanical workshop for their understanding and excellent work throughout this project.

Close collaboration with theory has been fundamental to all of the work shown in this thesis. Jeremy Hutson and his group have been crucial in providing a solid foundation on which we have built the experiment. Special thanks must go to Jesus Aldegunde for his calculations of the rotational and hyperfine energy structure used throughout this work.

I am eternally grateful to my friends both old and new. First of all I must thank Ian Critchley, who has been my close friend for the longest time. You have always been there for me and, whether it's just for a quick meet at the pub or a holiday in Scotland, you never fail to make me feel better about life. Huge thanks have to go to Glasto Team Alpha, especially Matt Hill and Dave Phillips for their showing me where the true fun is to be had in board games, live music, and kegs of beer. I am also thankful for the friends that I have made as part of the Van Mildert College MCR, in particular Blythe Goulet and Chris Vidler for too many fun memories to count.

Finally, I have thank my Mum, my Dad, my sister Cathy and brother-in-law Was for their reassurance and encouragement throughout my 8 years in Durham. Without them I am not sure where I would be.

Last but not least, thank you Sarah, for getting me to the end.

...also the cats (I guess).

Chapter 1

Introduction

1.1 Why Cold Molecules?

Experiments with atomic gases cooled to ultracold temperatures have proved to be enormously successful, and besides furthering our understanding of atomic systems outright [1–6], have found applications in many areas of research including many-body physics [7], quantum optics and quantum information processing [8, 9], and simulation of condensed-matter physics problems [10, 11]. However, the interactions between ground state atoms typically used in experiments are dominated by contact interactions which are only effective over short range. There is currently great interest in producing ultracold gases with dominant dipole-dipole interactions as they are, in contrast, long range and tunable. Such a dipolar gas may be realised in an atomic system either by using highly magnetic species such as Erbium [12, 13] or Dysprosium [14], or by using atoms in highly excited electronic states known as Rydberg atoms [15]. Each of these systems however has its drawbacks, as in the former case the dipole moment of each atom is still relatively small, while the latter's electronically excited states are short-lived. Polar molecules offer a fascinating middle ground between these two systems, as their electric dipole moments may be larger than the equivalent magnetic moments available in atoms, yet chemically stable species offer the hope of long lifetimes. As a result, many applications have been proposed for systems of ultracold polar molecules which include but are not limited to the fields of quantum-state-controlled chemistry [16, 17], quantum simulation [18–22], quantum information [23, 24], and precision measurement of fundamental constants [25]. It is only recently, however, that a few such molecules have been successfully trapped at ultracold temperatures making them available for experimental study [26–32].

The success of ultracold atomic systems stems from the development of a varied range of tools to carefully control both the motion and internal quantum state of the system. Similar tools and control must emerge in molecular systems if this new field is to flourish. Controlling the motion requires cooling of the molecules to ultracold temperatures in combination with confinement to an optical trap. The level of confinement required may vary depending upon the application, from a 3D trap where collisions between molecules are allowed in any direction, to a 3D lattice where single molecules are pinned to individual lattice sites and interactions must proceed over relatively long range. Control of the internal quantum state on the other hand requires detailed understanding of the rich and complex structure of the molecules, which is often hard to predict with theory alone. In this work, we will develop these tools for ultracold polar ^{87}Rb^{133}Cs molecules, though the techniques described may be applied to any bialkali molecule system. In addition, we will demonstrate the use of these tools to investigate the ultracold chemistry undergone during collisions of these bosonic molecules in a 3D optical trap.

1.2 Creating Ultracold Molecules - An Overview

Laser cooling has proved to be an incredibly powerful and robust tool for controlling the motion of atoms [33]. The method relies upon the repeated absorption and emission of photons by each atom in the ensemble being cooled. Each time a photon is absorbed, the atom of mass m experiences a momentum kick along the $\vec{k}$-vector of the light which changes the velocity of the atom by the recoil velocity $v_r = \hbar|\vec{k}|/m$. Some time later, the atom spontaneously emits a photon again experiencing another momentum kick. However, this spontaneous emission is spatially symmetric and over many absorption/emission cycles this second kick has no net effect on the atom's motion. Overall therefore, each atom experiences a time-averaged force in the direction of the light.

In order for this process to work, we require the presence of sufficiently *closed* transitions, which can allow the atom to scatter multiple photons while always returning to the same initial quantum state. In order to appreciably reduce the velocity of an atom, we typically need to scatter of the order of $> 10^5$ photons[1]. In atoms, such transitions are usually easy to find by making use of the angular momentum selection rules and choosing the correct laser polarisation[2]. However, the addition of rotational and vibrational degrees of freedom, means that even simple diatomic molecules possess a highly complex internal structure [34–38]. Sufficiently closed transitions are therefore difficult to find though recent experimental results have shown great progress [39–45].

Besides laser cooling, there are a multitude of alternative approaches which promise to efficiently cool molecules [46], though we only have time to briefly mention a few here. Molecular beams produced by laser ablation, or by supersonic expansion of molecules in a carrier gas for instance, can produce molecules with a high average but small distribution of velocities. Deceleration of such beams may be achieved using Stark [47, 48] or Zeeman [49–52] deceleration to velocities low enough for loading into a stationary trap for evaporative cooling. Another option is to use buffer gas cooling, which involves sympathetic cooling of molecules via collisions with a cold atomic gas (usually helium) [53–56]. Molecules cooled in this way are often used to form a cold molecular beam as they exit from the buffer gas cell through a small aperture. A promising technique to cool polyatomic molecules to low temperatures is that of optoelectric cooling [41, 57–59]. Here electrostatic trapping fields are used to remove the energy of polar molecules in a Sisyphus type process.

---

[1] For ^{87}Rb at a velocity of 300 m s^{-1}, the atomic momentum is $p_{\text{atom}} = 87u \times 300$ m s$^{-1} \simeq 4.3 \times 10^{-23}$ kg m s^{-1}. For cooling on the D$_2$ transition, the photon momentum is $p_{\text{photon}} = h/ \sim 780$ nm$\simeq 8.5 \times 10^{-28}$ kg m s^{-1}. The minimum total number of photons required to reduce the atoms velocity to zero is therefore $p_{\text{atom}}/p_{\text{photon}} \simeq 5 \times 10^4$

[2] Even in completely closed atomic transitions, off-resonant excitation can lead to population build up in dark states. Each additionally populated state requires a repump laser to return the population back to the cycling cooling transition. Systems requiring only one or two repumping lasers are common in atomic systems.

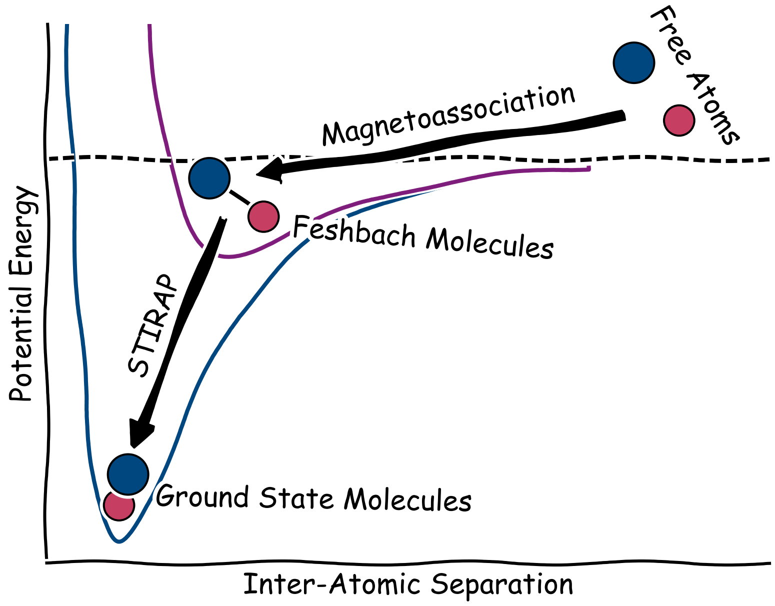

Figure 1.1: Overview of the method we use to produce ultracold molecules. Free atoms are associated into a weakly bound molecular state by magnetoassociation on an interspecies Feshbach resonance. These molecules are then transferred to the rovibronic ground state optically by stimulated Raman adiabatic passage (STIRAP).

So far we have only discussed techniques which attempt to *directly* cool molecules, beginning the process at high temperature. An alternative approach however, is to exploit the relative simplicity and wealth of experience that surrounds the cooling of atoms, and create ultracold molecules from a pre-cooled atomic sample. This so-called *indirect* method is implemented by either using an optical process (photo-association [60–64]) or via a magnetic Feshbach resonance to couple the free-atomic state to a bound molecular state [65].

In the work described in this thesis we apply the latter approach, where weakly-bound molecules are first created by magnetoassociation on a magnetic Feshbach resonance. These molecules are then subsequently transferred into their rovibrational ground state by stimulated Raman adiabatic passage (STIRAP) as shown in Fig. 1.1 [66, 67]. This approach was pioneered in polar molecules using fermionic KRb at JILA, Colorado [68]. Unfortunately, this system has the drawback that the exchange interaction $2\text{KRb} \rightarrow \text{K}_2 + \text{Rb}_2$

is exothermic [69]. This renders KRb molecules unstable [70] which leads to significant molecule losses [71, 72]. Confinement of the molecules in a three-dimensional optical lattice eliminates this reaction however [73], and has led to a series of ground-breaking insights into dipolar spin-exchange reactions [74]. There are currently a number of groups now pursuing this method of molecule production with molecules which are collisionally stable [69]. Yet despite the successful application of this technique in several systems [28–30, 32, 71] during the production of this thesis, the study of dipole-dipole interactions has so far been restricted to those early works.

1.3 Proposed Applications

At present, the proposals for systems of ultracold polar molecules are varied and span a number of highly active areas of research. As a result, it would be impossible to discuss every proposal made to date in the context of an introduction to the field. In this section therefore, we present case studies with reference to a few specific high impact papers which propose uses for ultracold polar molecules in the fields of quantum computing, quantum simulation, and precision measurements. In addition, the field of ultracold polar molecules may make significant contributions to the study of quantum-state-controlled chemistry [16, 17]. Such applications will be discussed more heavily in the later chapters of this thesis regarding collisions of ultracold molecules.

1.3.1 Quantum Computing

Proposal from D. DeMille, *Phys. Rev. Lett.* **88**, 067901 (2002) [23].

Here we describe a quantum computer where the qubits consist of the electric dipole moments of individual polar molecules, which can be oriented along or against an externally applied electric field. Transfer between qubit states, specifically different rotational states of the molecule, can be driven directly by microwave fields. The molecules are trapped in a 1D trap array, and interactions between neighbouring sites are mediated by the dipole-dipole interaction. By applying a spatially varying electric field, single sites may be

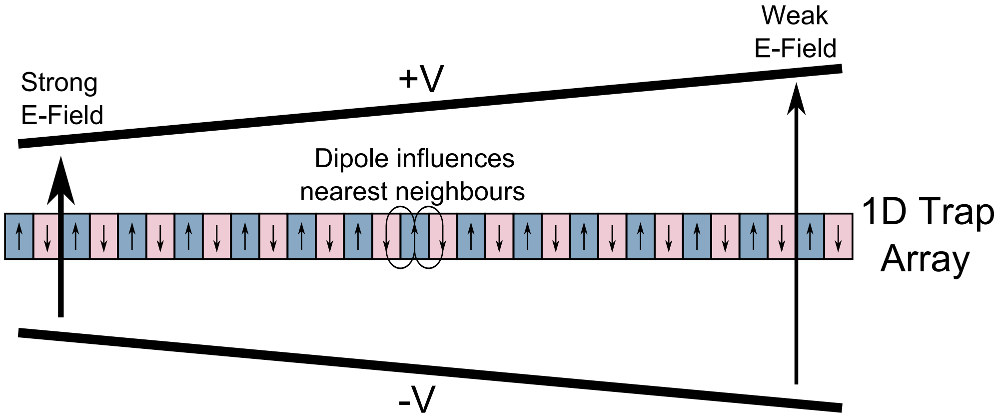

Figure 1.2: Proposed experimental apparatus for quantum computing using polar molecules as outlined in [23]. Qubit states correspond to electric dipole moments oriented up or down relative to the applied E-field.

individually addressed spectroscopically as the energy levels for each molecule will be uniquely DC Stark shifted depending on its position in the trap array. The basic experimental apparatus required is shown in Fig. 1.2.

The *quantum*[3] controlled-NOT (CNOT) logic gate along with single qubit rotations around the Bloch sphere forms a universal gate set. Any arbitrary computation can be carried out using some sequence of only these two operations. Realising such a gate operation therefore is a necessary condition for creating a quantum computer. The scheme for a CNOT gate operations in the architecture described here is essentially the same as that described for two quantum dots by Barenco *et al.* [75], and also similar in concept to the principle of Rydberg Blockade for highly excited atoms [76]. The process relies on the fact that in the presence of an externally applied electric field, the charge distribution of the molecular ground state is shifted in the direction of the applied field, while the charge distribution of the first excited state is shifted in the opposite direction. The electric field from this shifted charge distribution in one molecule may shift the energy levels of its neighbours, and the direction of this shift depends on the state of the neighbouring molecule. Hence, the resonant frequency to transfer one molecule between qubit states

---

[3] Note, that here we are discussing specifically *quantum* logic gates. The quantum CNOT gate must be distinguishable from the classical CNOT gate which can be performed on existing computers. Specifically, the quantum gate is sensitive to the phase between the qubits which would be irrelevant to classical operation [75].

depends upon the qubit state of its neighbours in the 1D array. This is exactly the condition we require to implement CNOT gate operations.

In the original paper by DeMille, the KCs molecule[4] is specifically considered though the concept is the same for other polar molecules including RbCs. In particular, the parameters important for determining the interaction strength between molecules are the lattice spacing and the dipole moment. The lattice spacing is determined by the wavelength and crossing angle of the interfering trapping beams and is therefore independent of the choice of molecule. The predicted dipole moment of RbCs is 1.28 D [80] (1.92 D for KCs). As the interaction strength is proportional to the effective dipole moment d_{eff}^2, we can therefore expect that for a given lattice spacing the interaction strength for RbCs will be approximately ∼50% that of an equivalent system using KCs. A more detailed analysis of the effective interaction strength between two RbCs molecules is given in 2.6.3.

Further work by Yelin *et al.* [24] shows how the dipole-dipole interactions may be switched 'on' and 'off' by the selective excitation of molecules to different quantum states. In this way, superposition states of neighbouring rotational levels become *strongly*-interacting qubits which can be used for computation. Meanwhile, superpositions of hyperfine states in the same rotational level are *weakly*-interacting and may be used as long-lived quantum memory [81].

1.3.2 Quantum Simulation

Proposal from R. Barnett *et al.*, *Phys. Rev. Lett.* **96**, 190401 (2006) [18].

Understanding complex quantum systems is best achieved by first examining a more simple yet still fundamentally quantum system. A variety of systems including but not limited to ultracold atomic gases [82], ensembles of trapped ions [83], photonic systems [84] and superconducting circuits [85] are all in development for use as quantum simulators. The work we will examine here, by Barnett *et al.* describes how a mixture of dipolar molecules in the lowest $N = 0$ and first excited $N = 1$ rotational states may be used to

---

[4] Fledgling KCs mixture experiments have begun at our group in Durham and in Innsbruck [77, 78] inspired by predictions of promising Feshbach resonances [79] and a large accessible dipole moment of ∼1.92 D [80].

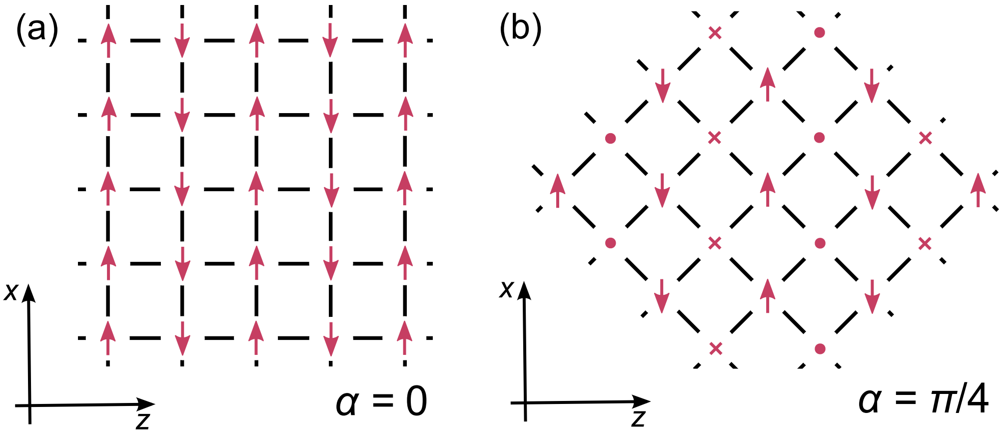

Figure 1.3: The ordering wave vector as the lattice is tilted by an angle α as shown in [18]. The system is prepared in a superposition of the $|N=0, M_N=0\rangle$ and $|N=1, M_N=1\rangle$ rotational and hyperfine states. A magnetic field is applied along the z-axis to lift the degeneracy of the $N=1, M_N=-1,0,1$ hyperfine levels. The angle α is that between one of the axes of the lattice and the magnetic bias field.

simulate a range of Mott insulating and superfluid phases. In particular, this proposal shows that a mixture of rotational states can exhibit long-range dipolar interactions even in the absence of an external electric field.

In one example given in this work, we consider a single layer of a 3D optical lattice in the xz plane with a single polar molecule at the centre of each site. A magnetic bias field is applied along z to break the degeneracy between $M_N = 0, \pm 1$ hyperfine state components, and we consider a rotation of the lattice with respect to that magnetic field by an angle α. The molecules are prepared in a superposition of $N = 0$ and $N = 1, M_N = 1$ states. When the magnetic field is parallel to one of the axes of the lattice (i.e. $\alpha = 0$), the molecules are allowed to rotate freely in the xy plane. For this case, the dipoles will choose to point head to tail along the bonds perpendicular to the magnetic field, while alternating antiferromagnetically in the other direction as shown in Fig. 1.3(a). If we rotate the lattice such that $\alpha = \pi/2$, a more complex pattern emerges as can be seen in Fig. 1.3(b). Further study shows the result of melting the Mott insulator to enter the superfluid state, and how the ordering wave vector is affected by this change.

More proposals for quantum simulation with ultracold polar molecules can be found in [19–22].

1.3.3 Precision Measurement

For an introduction to this topic, see T. E. Wall, *J. Phys. B: At. Mol. Opt. Phys.* **49**, 243001 (2016) [25].

Molecules not only offer a rich and complex internal structure, they also couple strongly to both DC and AC electric fields making them very useful for probing fundamental physics. At present, there is significant interest in measurements of the electric dipole moment of the electron; the electron is predicted to be slightly aspheric leading to it possessing a dipole moment, however it has so far proved to be too small to detect. In addition, the exact value of the dipole moment has significant implications for distinguishing between different models of particle physics. The exceptionally high internal effective electric field found in molecules offers an incredibly sensitive probe with which to measure the electric dipole moment of the molecule. Measurements have been performed using YbF at Imperial College, London [86] and in ThO by the ACME collaboration [87]. The lowest sensitivity measurement so far was performed in ThO and found a dipole moment $d_e = -2.1 \pm 3.7_{\text{stat}} \pm 2.5_{\text{syst}} \times 10^{-29}$ $e{\cdot}$cm [87]. This value is still consistent with zero but puts an upper limit on the dipole moment which can be reduced with ever increasing experimental precision.

Molecules are also critical in the search for variation of fundamental constants with varying time, position or local density of matter. Truppe *et al.* performed spectroscopy of microwave transitions on a pulsed beam of cold CH molecules for comparison with those measured from sources of CH in the Milky Way [88]. By doing this, a limit on the variation of the fine structure constant and electron-to-proton mass ratios between the high- and low-density environments of the Earth and the interstellar medium were found which are at present only limited by the current astrophysical measurements.

The precision of each of these measurements relies upon the available interaction time with the sample of molecules - the longer the interaction time, the higher the precision. In addition, low temperatures are necessary to minimise thermal broadening of the measured transitions. Trapped samples of molecules at ultracold temperatures are therefore required for the highest precision; learning to produce and control ultracold molecules is the next step to enhance the precision of these important measurements.

1.4 Thesis Overview

This thesis is structured as follows:

In chapter 2, we give an overview of the theoretical background required to understand the results presented in this thesis. This includes a discussion of why we choose to work with ^{87}Rb^{133}Cs, the key steps to producing ground state molecules from an atomic mixture, the structure of diatomic molecules, and interactions specifically relevant to polar molecules.

In chapter 3, we describe the experimental apparatus with particular attention paid to modifications made over the course of this work. In particular, we discuss the addition of DC electric fields and MW fields which are both used to probe the molecule's electric dipole moment and internal structure.

In chapter 4, we demonstrate that our apparatus can produce 4000 optically trapped ^{87}Rb^{133}Cs molecules in their rovibronic and hyperfine ground state. We characterise the molecules by measuring their temperature, binding energy, and electric dipole moment.

In chapter 5, we show that we can coherently control the rotational and hyperfine state of the molecules using externally applied microwaves. We begin by performing spectroscopy of the first rotationally excited state with hyperfine state resolution. By fitting theory to experimental measurements, we obtain new values for the rotational constant, scalar spin-spin coupling constant, electric quadrupole coupling constants, and nuclear g-factors (including shielding) for the molecule. We then proceed to use this knowledge of the internal structure of the molecule to change both the rotational and hyperfine state of the molecule using coherent π-pulses - transferring the population with 100% efficiency between hyperfine states in the ground, first-excited, and second-excited rotational states.

In chapter 6, we investigate the effect of the far-off-resonant light of our optical dipole trap on the molecules. Following a discussion of the difference between the polarisability of atoms and molecules, we use a combination of spectroscopic measurements and parametric heating to completely characterise the polarisability of the molecule at a wavelength of 1550 nm. We find that the trapping light couples neighbouring hyperfine states, giving rich and complex structure with many avoided crossings as a function of laser intensity. This coupling may be tuned by varying the angle between the laser polarisation and the applied magnetic field.

In chapter 7, we measure the lifetime of the molecules in our 3D optical dipole trap. We observe loss of molecules which leads to a lifetime in the trap of around 1 s. We investigate the loss rate of the molecules as a function of dipole trap laser intensity, magnetic field, and rotational and hyperfine state. The possible loss processes are discussed, though it is not possible to determine which is dominant in our experiment at this time. We outline the next step in our experiment - to investigate the collisions between atoms and molecules.

1.5 Publications

The following publications have been prepared during the course of this work:

- **Creation of ultracold ^{87}Rb^{133}Cs Molecules in the Rovibrational Ground State**
  Peter K. Molony, Philip D. Gregory, Zonghua Ji, Bo Lu, Michael P. Köppinger, C. Ruth Le Sueur, Caroline L. Blackley, Jeremy M. Hutson, and Simon L. Cornish.
  Phys. Rev. Lett. **113**, 255301 (2014).

- **Repeated Output Coupling of Ultracold Feshbach Molecules from a Cs BEC**
  M. P. Köppinger, P. D. Gregory, D. L. Jenkin, D. J. McCarron, A. L. Marchant, and S. L. Cornish.
  New J. Phys. **16**, 115016 (2014).

- **A Simple, Versatile Laser System for the Creation of Ultracold Ground State Molecules**
  P. D. Gregory, P. K. Molony, M. P. Köppinger, A. Kumar, Z. Ji, B. Lu, A. L. Marchant, and S. L. Cornish.
  New J. Phys. **17**, 055006 (2015).

- **Absolute Absorption on the Potassium D Lines: Theory and Experiment**
  Ryan K. Hanley, Philip D. Gregory, Ifan G. Hughes, and Simon L. Cornish.
  J. Phys. B: At. Mol. Opt. Phys. **48**, 195004 (2015).

- **Measurement of the Binding Energy of Ultracold ^{87}Rb^{133}Cs Molecules using an Offset-Free Optical Frequency Comb**
  Peter K. Molony, Avinash Kumar, Philip D. Gregory, Russel Kliese, Thomas Puppe, C. Ruth Le Sueur, Jesus Aldegunde, Jeremy M. Hutson, and Simon L. Cornish. *Phys. Rev. A* **94**, 022507 (2016).

- **Production of Ultracold ^{87}Rb^{133}Cs in the Absolute Ground State: Complete Characterisation of the STIRAP Transfer**
  Peter K. Molony, Philip D. Gregory, Avinash Kumar, C. Ruth Le Sueur, Jeremy M. Hutson, and Simon L. Cornish.
  ChemPhysChem **18**, 3811 (2016).

- **Controlling the Rotational and Hyperfine State of Ultracold ^{87}Rb^{133}Cs Molecules**
  Philip D. Gregory, Jesus Aldegunde, Jeremy M. Hutson, and Simon L. Cornish.
  Phys. Rev. A **94**, 041403(R) (2016).

- **ac Stark Effect in Ultracold Polar ^{87}Rb^{133}Cs Molecules**
  Philip D. Gregory, Jacob A. Blackmore, Jesus Aldegunde, Jeremy M. Hutson, and Simon L. Cornish.
  Phys. Rev. A **96**, 021402(R) (2017).

Chapter 2

Theory

In this chapter we will discuss the necessary theory to understand the rest of the work presented in this thesis and the Rb-Cs mixtures experiment in general. We begin by discussing a few of the considerations which must be made when choosing a molecule to study in an experiment such as ours (2.1). Following this, we will outline some of the processes which we use to create and trap an ultracold atomic mixture from which we can associate molecules (2.2). We will then give a brief introduction to the theory of scattering between ultracold atoms and how molecules can be associated by magnetoassociation on a magnetic Feshbach resonance (2.3). Next we will explain how the process of Stimulated Raman Adiabatic Passage between molecular states works (2.4) before reviewing the structure of diatomic molecules (2.5). Finally, we will consider interactions between polar molecules, and between polar molecules and external electric fields (2.6).

2.1 Choosing the Molecule - ^{87}Rb^{133}Cs

As has been discussed in the introduction, the key property of diatomic molecules which we aim to exploit is that they can possess a large permanent electric dipole moment. This property is only available to heteronuclear molecules (as opposed to homonuclear molecules) and so an appropriate mixture of atoms must be selected as the starting point for any experiment such as ours.

	d_0 **(D)**	B_v **(GHz)**	$E_{\mathbf{crit}}$ **(kV cm^{-1})**	**Stable**
LiNa	0.53	11.22	36.1	N
LiK	3.50	7.68	4.3	N
LiRb	4.13	6.45	3.1	N
LiCs	5.48	5.61	2.0	N
NaK*	2.75	2.85	2.0	Y
NaRb*	3.33	2.10	1.3	Y
NaCs	4.60	1.74	0.7	Y
KRb*	0.62	1.16	3.74	N
KCs	1.92	0.90	1.0	Y
RbCs*	1.26	0.51	0.80	Y

Table 2.1: Molecule frame dipole moment d_0, rotational constant B_v, and critical electric field (E_{crit}) for a range of bialkali molecular dimers. Stability of each combination against exchange collisions of the form $2XY \rightarrow X_2 + Y_2$ is also shown. Data from [69, 80, 92, 93]. *Dimers which have been produced in their rovibronic ground state at ultracold temperatures at time of writing [28–30, 32, 71].

To implement an indirect cooling method, the chosen constituent atoms for the molecule must be suitable for laser cooling and trapping. We therefore limit our search to alkali metal species, though a growing number of molecule experiments are beginning to use other species such as alkaline earths [89–91] as laser cooling is applied to more varied and complex systems.

It is also necessary that the system possesses either an experimentally accessible broad inter-species Feshbach resonance or strong optical coupling to the molecular states. The prediction of positions of inter-species Feshbach resonance is not trivial, though reasonable estimations can be made using the molecular potentials attained from spectroscopic work [79, 94]. In addition, recent theoretical work has suggested that it is possible to ‘create’ Feshbach resonances at an arbitrary magnetic field by dressing the molecular state with a strong resonant RF field [95].

A complete comparison of the various bialkali dimers available can be seen in table 2.1. The ^{87}Rb^{133}Cs molecule we use in our experiment has many beneficial properties[1]. For example, it is chemically stable - the atom exchange reaction 2RbCs→Rb_2 + Cs_2 is endothermic [69]. This property is crucial to avoid large losses of molecules through chemically reactive collisions, and many of the possible combinations do not fulfil this criteria. In addition, the large electric dipole moment of 1.26 D is aligned by a relatively small electric field gradient.

2.2 Creating an Ultracold Atomic Mixture

The experimental sequence for producing an ultracold mixture of ^{87}Rb and ^{133}Cs atoms has been developed over a number of years by previous students working on the experiment [96–101]. A good understanding of the physics behind the techniques employed is highly important to the continuous running of the experiment and correct optimisation of this sequence is the key to producing a large number of molecules.

The experimental sequence has many stages. First we load both species into a magneto-optical trap (MOT) where the Rb and Cs are slightly separated by addition of a Rb 'pusher' beam. The MOTs are then fully overlapped in a compressed-MOT stage before performing optical molasses and optical pumping to the magnetically trappable $|f = 1, m_f = -1\rangle$ and $|f = 3, m_f = -3\rangle$ states for Rb and Cs respectively. Both species are then loaded into the same magnetic quadrupole trap where we perform forced-RF evaporation to cool the Rb, and the Cs is cooled sympathetically. Cooling in the magnetic trap is limited by Majorana losses and so both species are transferred into a magnetically levitated crossed optical dipole trap. Here the spins of both species are flipped so that they occupy the $|f = 1, m_F = 1\rangle$ and $|f = 3, m_f = 3\rangle$ hyperfine ground states (which are not magnetically trappable). Both species are evaporatively cooled in this levitated potential down to high phase-space densities. In this section we will only discuss the key components towards the end of this sequence; specifically magnetic levitation (2.2.1) and optical trapping (2.2.2), as they are also relevant to the

---

[1] Beside the excellent properties of the molecule, ^{87}Rb may offer the most well documented route to ultracold temperatures being the first element to ever be cooled to quantum degeneracy [1].

molecule work presented later.

Before proceeding further we note that during evaporation we selectively remove the most energetic atoms in order to reduce the temperature of the remaining sample. It is therefore not possible to simply optimise routines for highest number or lowest temperature of atoms as lower temperatures necessitates the removal of atoms. The quantity which we wish to maximise in our atomic mixture is the phase-space density (PSD)

$$\mathrm{PSD} = n_0 \lambda_{\mathrm{dB}}^3, \tag{2.1}$$

where n_0 is the peak density in the sample and λ_{dB} is the thermal de Broglie wavelength. When the PSD ~ 2.612, the ensemble forms a Bose-Einstein condensate.

2.2.1 Magnetic Levitation

The interaction between the magnetic moment of an atom or molecule with an applied magnetic field gradient generates a force which can be used to cancel the force due to gravity and hence ‘levitate’ the sample. This makes experiments which require the ultracold gas to be monitored in free space for long periods of time (e.g. time of flight expansion measurements) possible as without this levitation the atoms would fall out of the imaging region. In addition, it can be used to cancel the gravitational sag in a weak optical trap or separate an initially mixed sample of atoms or molecules with different ratios of magnetic moment to mass.

In order to exactly cancel the force due to gravity the following condition must be satisfied

$$mg = \nabla(\vec{\mu} \cdot \vec{B}). \tag{2.2}$$

The left hand side of this equation is the force due to gravity on a particle of mass m, while the right hand side is the force on a particle with magnetic moment $\vec{\mu}$ in an applied magnetic field $\vec{B}$ [102]. In theory, the magnetic moment of an atom depends upon the magnetic field owing to the quadratic nature of the Zeeman effect. However, in a typical experiment at high field and for relatively small changes in magnetic field the magnetic moment can be

Species	m (a.u.)	B (G)	μ (μ_B)	$\partial\vec{B}/\partial\vec{z}$ (G/cm)
^{87}Rb $\lvert f=1, m_f=1\rangle$	87	0	-0.50	30.5
^{133}Cs $\lvert f=3, m_f=3\rangle$	133	0	-0.75	31.1
^{87}Rb^{133}Cs $\lvert -1(1,3)s(1.3)\rangle$	220	185	-1.33	29.1
^{87}Rb^{133}Cs $\lvert -6(2,4)d(2,4)\rangle$	220	181.5	+1.50	-25.8
^{87}Rb^{133}Cs $\lvert -2(1,3)d(0,3)\rangle$	220	181.0	-0.84	46.0
^{87}Rb^{133}Cs Ground State	220	181.5	0.005	7700

Table 2.2: Levitation gradients $\partial\vec{B}/\partial\vec{z}$, magnetic moments μ, and masses m for the different species and states relevant to the work presented in this thesis. State notation for molecules in Feshbach states is explained in section 2.3.3. ^{87}Rb^{133}Cs Molecules in the rovibronic and hyperfine ground state have a negligible magnetic dipole moment when compared to atoms or Feshbach molecules as only the small nuclear magnetic moments can contribute.

assumed to be constant and so Eq. 2.2 can be rewritten to give the magnetic field gradient required to exactly levitate a given atom or molecule

$$\frac{\partial\vec{B}}{\partial\vec{z}} = \frac{mg}{\mu}, \tag{2.3}$$

where $\vec{z}$ is the unit vector in the vertical direction, and $\mu = \pm|\vec{\mu}|$ is the magnitude of the dipole moment where the sign indicates whether it is oriented parallel or antiparallel to the applied field. It is most important in our experiment that the gradient required to levitate atomic ^{87}Rb and ^{133}Cs in their respective Zeeman hyperfine ground states is roughly the same which allows us to ensure the two species are well overlapped. This field gradient is different from that required for the available states of the molecules. See Table 2.2 for a summary of the field gradients required to levitate both the relevant atomic and molecular states relevant to our experiment.

2.2.2 Optical Trapping and Evaporation

The optical dipole trap is the final trap in which our atomic mixture and created molecules are confined. The maximum depth achievable in such a trap is typically quite low $\sim 10\mu$K, which necessitates the pre-cooling of the atoms via the techniques described earlier in this section. Optical dipole traps rely upon the electric dipole moment induced by the AC electric field of a laser beam, and the interaction of that induced dipole moment with the intensity gradient of the light. The optical potential due to this interaction is given by [103]

$$U_{\mathrm{dip.}}(r) = -\frac{1}{2\epsilon_0 c}\mathrm{Re}(\alpha)I(r) \approx \frac{3\pi c^2\Gamma}{2\omega_0^3}\frac{I(r)}{\Delta}, \tag{2.4}$$

where $\mathrm{Re}(\alpha)$ is the real part of the complex polarisability α, $I(r)$ is the intensity of the light field, ω_0 is the resonant transition frequency, Δ is the detuning of the laser frequency from the transition, and Γ is the decay rate from the excited state. Heating and loss of atoms can be caused by scattering of the light by the atoms. The scattering rate Γ_{sc} is related to the imaginary part of the complex polarisability $\mathrm{Im}(\alpha)$ [103],

$$\Gamma_{\mathrm{sc}} = \frac{1}{\hbar\epsilon_0 c}\mathrm{Im}(\alpha)I(r) \approx \frac{3\pi c^2}{2\hbar\omega_0^3}\left(\frac{\Gamma}{\Delta}\right)^2 I(r). \tag{2.5}$$

From Eq. 2.4 and 2.5 it can be seen that the dipole potential scales as I/Δ whereas the scattering rate scales as I/Δ^2. It is therefore beneficial to operate a dipole trap using very high intensity laser light which is far-detuned from any resonant transitions in order to minimise scattering for a given potential depth. This is particularly important to remember in our experiment as both molecules and atoms use the same optical trapping light and scattering must be minimised throughout the experiment. The polarisability of $^{87}\mathrm{Rb}^{133}\mathrm{Cs}$ molecules is investigated in more detail in chapter 6.

Evaporation is performed in the optical dipole trap by reducing the intensity of the trapping beams. This reduces the depth of the trap and allows the most energetic atoms in the sample to leave the trap.

2.3 Magnetoassociation

The two methods which are typically employed to associate atoms to form molecules are photoassociation and magnetoassociation. *Photoassociation* is a process in which two colliding atoms absorb a photon to form a molecule in a highly excited state [64]. Molecules formed by this approach will quickly decay to a lower energy state of which there are a large number available. It can therefore be difficult to ensure all molecules formed are in the same state, i.e. it is hard to create a sample with a high state coherence. Recent work has shown that a sample of ^{87}Rb^{133}Cs molecules where 33% of the molecules occupy the rovibronic ground state may be created using this approach [31]. Samples of ^{7}Li^{133}Cs molecules have also been produced in this way [27]. *Magnetoassociation* on the other hand is a process whereby atoms are made to follow an avoided crossing between the free atomic state and a molecular bound state by the adiabatic ramping of an applied magnetic field over a Feshbach resonance[2]. All molecules produced by this process occupy the same state (though they may need to be separated from the remaining unbound atoms in the sample). It is this process which we use in our work and we will discuss in more detail here.

2.3.1 Feshbach Resonances and Scattering Theory

Atoms or molecules in an ultracold gas may interact with each other through both elastic and inelastic collisions. Elastic collisions allow processes such as evaporative and sympathetic cooling and are 'good' for efficient cooling and trapping, while inelastic collisions are responsible for trap loss and can be thought of as 'bad'. It is therefore important in experiments that the ratio of the elastic and inelastic collision rates are kept favourable, with elastic collisions being the desired dominant process. At ultracold temperatures, interactions can be effectively described by a single parameter - the s-wave scattering length a, and control of this parameter may be achieved by varying the magnetic field in close proximity to magnetic Feshbach resonances. Such control is the key to our experiment where we need to engineer the interactions between atoms throughout cooling and association. Here, we will briefly examine where this single parameter comes from and the origin of magnetic Feshbach resonances. It is important to note that this is far from a thorough treatment of either of these topics, and far more details may be

---

[2] The association of molecules using a resonant RF field at a fixed magnetic field close to an interspecies Feshbach resonances is also sometimes referred to as magnetoassocition. The method of sweeping the magnetic field over the resonance is the one which we employ in our experiment, and we will only use magnetoassociation to refer to this method here.

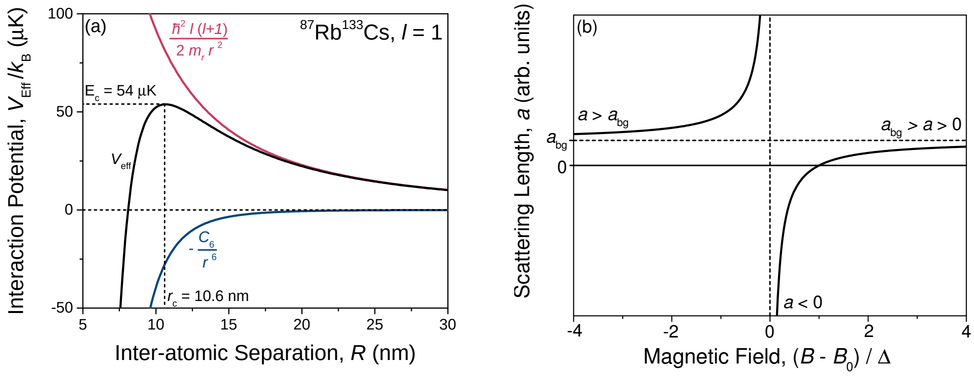

Figure 2.1: Potential wave barrier and tunability of scattering length close to a Feshbach resonance. (a) Effective potential barrier for p-wave collisions. The effective potential between two colliding particles is described by Equation 2.11. For any partial wave $l > 0$, this effective potential forms a barrier. At temperatures below this barrier height, that potential wave will no longer contribute to the collision. For $l = 1$ in ^{87}Rb^{133}Cs, this barrier height is equal to 54 μK and so below this temperature only s-wave collisions may occur. (b) Generalised diagram of a Feshbach resonance described by equation 2.15 with a non-zero positive background scattering length. By tuning the magnetic field close to the resonance, the scattering length may be controlled.

found in the wealth of review articles and textbooks which are already in publication [104–111].

To understand why we can describe collisions between atoms using only a single parameter a, we must first look at the scattering cross section σ. This quantity can be derived by considering two colliding particles as a superposition of plane-waves in a spherically symmetric interaction potential as shown in [100]. The general equation for the scattering cross section is given for angular momentum quantum numbers (partial waves) l by

$$\sigma = \frac{4\pi}{k^2} \sum_l (2l+1) \sin^2 \delta_l(k), \tag{2.6}$$

where $k = |\vec{k}|$ is the amplitude of the incident wave vector and δ_l is the phase shift between the incoming and outgoing plane waves. However, this is only necessarily applicable to distinguishable particles.

In the case of indistinguishable particles, the scattering wave function must be (anti-)symmetric for bosons (fermions) and their scattering wave functions have the form $\Psi(\vec{r}_1, \vec{r}_2) = \epsilon \cdot \Psi(\vec{r}_2, \vec{r}_1)$ with $\epsilon = +1(-1)$ for bosons (fermions).

This wave function can be written in terms of plane waves

$$\Psi_{\vec{k}}(\vec{r}) = e^{i\vec{k}\vec{r}} + \epsilon e^{-i\vec{k}\vec{r}} + \big(f(k,\theta) + \epsilon f(k,\pi-\theta)\big)\frac{e^{ikr}}{r}, \tag{2.7}$$

with differential cross section

$$\frac{d\sigma}{d\Omega} = |f(k,\theta) + \epsilon f(k,\pi-\theta)|^2, \tag{2.8}$$

where $f(k,\theta)$ is the scattering amplitude and θ ranges from 0 to $\pi/2$. The scattering amplitude may be written in terms of Legendre polynomials [100] and therefore have a parity of $(-1)^l$ which leads to a cancellation of all odd (even) partial wave contributions for bosons (fermions). In addition, the contribution of even partial waves is doubled for the bosonic case, which we can show by expanding equation 2.8,

$$\frac{d\sigma}{d\Omega} = |f(k,\theta)|^2 + |f(k,\pi-\theta)|^2 + f^*(k,\theta)f(k,\pi-\theta) + f(k,\theta)f^*(k,\pi-\theta). \tag{2.9}$$

Here, the final two terms indicate interference in the bosonic case which leads to a factor of two increase in the scattering cross section for identical bosons, i.e.

$$\sigma = \frac{2\times 4\pi}{k^2}\sum_{l_{\text{even}}}(2l+1)\sin^2\delta_l(k). \tag{2.10}$$

Note, that in a mixture experiment such as ours where collisions may occur between different bosons, *both* even and odd partial waves contribute and this doubling does not happen. In this case, the scattering cross section is identical to Eq. 2.6 with the sum being over all available partial waves.

The availability of partial waves is dependent upon the temperature of the gas. Non-zero partial wave contributions give rise to a centrifugal term $\hbar^2 l(l+1)/(2m_r r^2)$ which leads to an effective barrier superimposed on the long range part of the interaction potential

$$V_{\text{eff}}(r) = -\frac{C_6}{r^6} + \frac{\hbar^2 l(l+1)}{2m_r r^2}, \tag{2.11}$$

where r is the separation between the two particles and C_6 is the dispersion coefficient between the colliding atoms. This effective potential for a mixture of Rb and Cs is shown in Fig. 2.1(a), where for Rb-Cs collisions $C_6 = 5693\ E_\text{h}\ a_0^6$ [94]. If the temperature of the gas is lower than the barrier height for a given partial wave, that partial wave cannot contribute to the scattering cross section. The barrier for p-wave[3] ($l = 1$) has a height of 54 µK in Rb-Cs, and hence for all temperatures lower than this only s-wave ($l = 0$) scattering is present. This occurs at a higher temperature for Rb-Rb and Cs-Cs collisions as the lowest non-zero partial waves are d-wave ($l = 2$). These d-wave partial waves are frozen out below temperatures of 412 µK, 180 µK, and 282 µK for Rb-Rb, Cs-Cs, and Rb-Cs collisions respectively [94, 100, 112, 113].

It follows from equation 2.6 that the scattering cross section for a purely s-wave collision is[4]

$$\sigma = \frac{2 \times 4\pi}{k^2} \sin^2 \delta_0(k). \tag{2.12}$$

The scattering phase shift scales as $\delta_l \propto k^{2l+1}$ at low energies where the relative wave vector $k \to 0$. The s-wave scattering length can therefore be defined as

$$a = -\lim_{k \to 0} \frac{\tan \delta_0(k)}{k}. \tag{2.13}$$

The resulting scattering cross section at the limit where $ka << 1$ is therefore [105, 106]

$$\sigma = \frac{2 \times 4\pi a^2}{1 + k^2 a^2} \approx 2 \times 4\pi a^2, \tag{2.14}$$

which depends only upon the scattering length a. In this limit, collisions between particles is equivalent to a collision between two hard spheres with radii equal to the scattering length. A positive scattering length indicates repulsive interactions, while a negative scattering length indicates attractive interactions.

Feshbach resonances offer a powerful method for tuning the scattering length by varying the magnitude of an applied magnetic field B. They arise due to the presence of molecular bound states with different magnetic moments to the free atomic state. The application of a magnetic field therefore Zeeman shifts both the atomic and molecular state energies, but each is shifted by a different amount. A Feshbach resonance occurs when a molecular state and atomic state have the same energy, and this generates an avoided crossing

---

[3] Partial waves are commonly labelled using spectroscopic notation where $l = 0, 1, 2, 3...$ are referred to as $s, p, d, f....$

[4] The factor of two in equation 2.12 should only be included for collisions between identical bosons. when there are two species involved, this factor of two is not necessary!

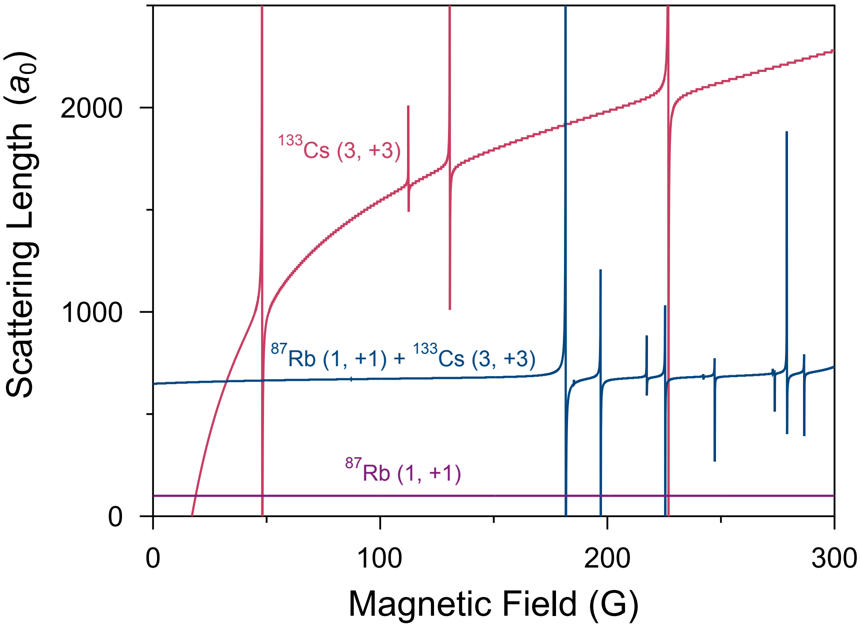

Figure 2.2: Scattering lengths for ^{87}Rb-^{87}Rb, ^{133}Cs-^{133}Cs, and ^{87}Rb-^{133}Cs ground-state atomic collisions with varying magnetic field. Labels in parenthesis are (f, m_f).

between the molecular (bound) and atomic (unbound) states. This avoided crossing may be adiabatically followed to create molecules as we will discuss in section 2.3.2, and also causes a pole in the scattering length of the form

$$a(B) = a_{\mathrm{bg}} \left(1 - \frac{\Delta}{B - B_0} \right), \tag{2.15}$$

where B_0, Δ are the centre and width of the resonance in magnetic field and a_{bg} is the background scattering length in the absence of the resonance. An example of a Feshbach resonance of the form given in Equation 2.15 is shown in Fig. 2.1(b). At the centre of the resonance the scattering length tends asymptotically to $\pm\infty$, and close to the resonance the scattering length can effectively by tuned to any value both positive and negative depending on the choice of magnetic field. Such control is critical in for example, the Bose-Einstein condensation of ^{133}Cs [114, 115] and ^{85}Rb [116, 117], and in the formation and study of bright matter-wave solitons [118, 119].

The scattering lengths of the atomic scattering partners relevant to our experiment are shown in Fig. 2.2. The contrast between the two species we use in our experiment is quite clear. The scattering length for ^{87}Rb-^{87}Rb collisions is reasonably low, yet high enough to enable efficient evaporative cooling, and is independent of magnetic field. The simplicity of ^{87}Rb is one of the primary reasons that it has long been favoured in many ultracold atom experiments. The scattering length for ^{133}Cs-^{133}Cs on the other hand is negative (attractive) at low magnetic fields and becomes very large and positive (repulsive) at high magnetic fields. A large number of wide Feshbach resonances are present, which can enable control of the intraspecies scattering. However, this must be done at very specific and well controlled magnetic fields. In our experiment, we perform the evaporative cooling with ^{133}Cs close to the zero-crossing at $\sim$ 17 G for this reason. Specifically there is a window between 21-25 G where ^{133}Cs may be condensed. Here, the scattering length varies between approximately 200-400 a_0 and there is a minimum in the recombination rate due to the existence of Efimov physics[5] (when $a \approx 210 a_0$, $B \approx 21$ G) [99, 120].

The interspecies scattering is important both for the pre-cooling of the atomic mixture and the production of molecules. The interspecies scattering length is relatively high $\sim$ 650 a_0, which enables the sympathetic cooling of ^{133}Cs, though also leads to a high 3-body loss rate. In addition, at high phase-space densities, this strong repulsive interaction leads to phase separation [115] which restricts the production efficiency of molecules by magnetoassociation. The two lowest field interspecies magnetic Feshbach resonances are those relevant to our molecule production and are discussed more in section 2.3.3. There is a rich structure of interspecies Feshbach resonances we do not presently use above $B \approx 200$ G, which may be useful in future experiments.

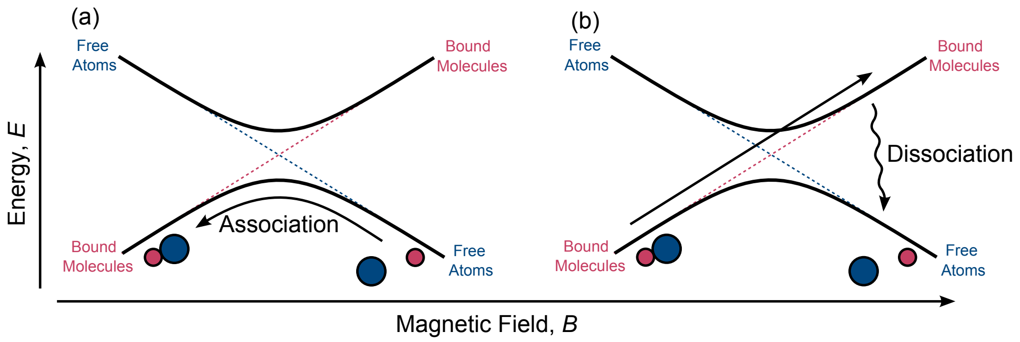

Figure 2.3: Scheme for association of atoms into molecules and dissociation of molecules back to atoms on a Feshbach resonance. (a) Ramping the magnetic field down slowly allows the avoided crossing between the free atom and bound molecule states to be followed, associating atoms into molecules. (b) To dissociate the molecules, the avoided crossing does not need to be followed as the molecule state is above the dissociation energy.

2.3.2 Molecule Production on a Feshbach Resonance

Molecules can be formed by adiabatically following the avoided crossing between the free atomic state and the bound molecular state as shown in Fig. 2.3. In the case depicted, at fields below the resonance the molecular state lies below the atomic state while above the resonance the atomic state is the lower in energy. We can therefore associate molecules by ramping the magnitude of the applied magnetic field down across the resonance (from high to low field). Dissociation may be performed by ramping the field in the opposite direction, however in this case the avoided crossing does not need to be followed as above the resonance the molecular state will spontaneously decay down to the energetically favourable atomic state within a short time (see Fig. 2.3(b)).

The efficiency of magnetoassociation is strongly dependent on the phase-space density of the initial atomic ensemble [121] and the adiabaticity of the state transfer. Maximum phase-space density is achieved by cooling the

---

[5] Efimov states are weakly-bound trimer states which may exist even where there are no bound dimer states. In particular, these states appear near to the resonance condition for two-body interactions (i.e. near to Feshbach resonances). The existence of such states leads to an enhancement of the three-body recombination loss in the atomic sample. In order to efficiently cool ^{133}Cs, we ideally want to minimise loss by such processes, and this was found to be achievable experimentally when the scattering length is 210 a_0 by Kraemer *et al.* [120]

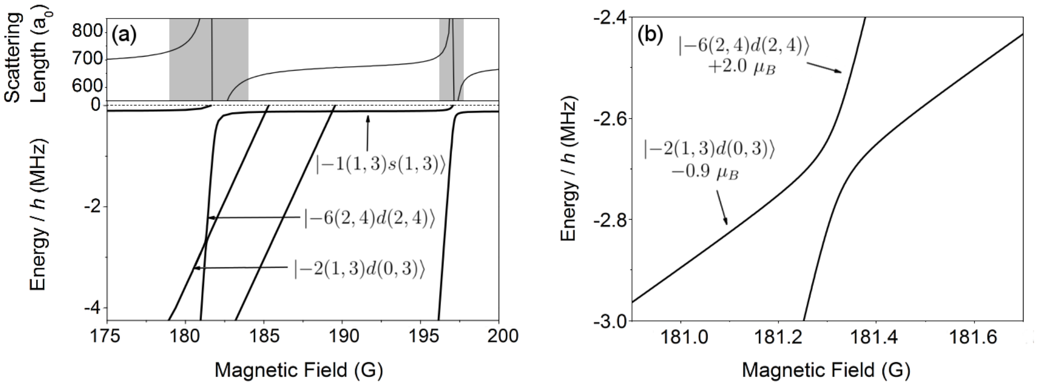

Figure 2.4: Near-threshold ^{87}Rb^{133}Cs molecular states. (a) Upper panel: the interspecies scattering length between ^{87}Rb and ^{133}Cs, the grey regions highlight the locations of the two Feshbach resonances in the relevant magnetic field region. Molecules are associated on the higher-field resonance at 197 G. Lower panel: Weakly-bound states relevant to the Feshbach association sequence. (b) The avoided crossing between the $|{-6}(2,4)d(2,4)\rangle$ and $|{-2}(1,3)d(0,3)\rangle$ states which is followed both during the association sequence and following the transfer to a pure optical dipole trap for ground state transfer.

atoms to degeneracy but for a mixture of ^{87}Rb and ^{133}Cs, this does not lead to efficient magnetoassociation. This is due to the large inter-species scattering length which renders the two species immiscible [115]. Maximum efficiency is therefore achieved at high phase-space density provided that the atomic populations can be well overlapped. The avoided crossing at a Feshbach resonance can be described using the Landau-Zener model and are characterised by two parameters: the coupling strength V and the difference in magnetic moment between the states $\Delta\mu$. The coupling strength is defined as one-half the energy splitting between the two states at the crossing point. We can then define the critical ramp speed

$$\dot{r_c} = \frac{2\pi V^2}{\hbar|\Delta\mu|}. \tag{2.16}$$

In order to adiabatically follow the avoided crossing and efficiently create molecules, the magnetic field must be ramped over the crossing at a rate $\ll \dot{r_c}$.

2.3.3 Control of the Feshbach State

Control of the molecular state in the near-dissociation states is critical in our experiment, and such control requires detailed knowledge of the energies and positions of avoided crossings between those states. All bound state energies presented in this work have been calculated by Jeremy Hutson's group at Durham University using the BOUND [122] and FIELD [123] packages for the MOLSCAT program [124] as modified to handle collisions in external magnetic fields [125]. The accuracy of these calculations is dependent upon how well known the potential energy curves are, which is determined by the available spectroscopic work [126] and experimentally determined positions of Feshbach resonances [127–129].

The near dissociation states are labelled as $|n(f_{\mathrm{Rb}}, f_{\mathrm{Cs}})L(m_{f_{\mathrm{Rb}}}, m_{f_{\mathrm{Cs}}})\rangle$. Here n is the vibrational label for the particular hyperfine (f_{Rb}, f_{Cs}) manifold, counting down from the least-bound state which has $n = -1$, and L is the quantum number for rotation of the two atoms about their centre of mass[6]. All of the relevant Feshbach states to this work have $M_{\mathrm{tot}} = 4$, where $M_{\mathrm{tot}} = M_F + M_L$ and $M_F = m_{f_{\mathrm{Rb}}} + m_{f_{\mathrm{Cs}}}$. These near-theshold molecular states may be seen in Fig. 2.4(a). Note that in ^{87}Rb^{133}Cs, the $|-1(1,3)s(1,3)\rangle$ bound state runs parallel and very close to the dissociation energy, with a binding energy of only $\sim$ 150 kHz. It is the presence of this state that is responsible for the high inter-species scattering length between ^{87}Rb and ^{133}Cs atoms. Association on the Feshbach resonance at $\sim$ 197 G directly couples molecules into this state.

Control of the Feshbach state may be achieved by manipulation of the applied external magnetic field. By sweeping the magnetic field either slowly or quickly, the avoided crossings between states may be adiabatically followed or non-adiabatically 'jumped' across. The critical ramp speed which determines whether an avoided crossing will be followed is the same as that presented in the previous subsection in equation 2.16. We can therefore transfer molecules out of the initial $|-1(1,3)s(1,3)\rangle$ state by reducing the field to reach an adjacent Feshbach resonance at $\sim$ 181 G where there exists a wide avoided crossing which leads into the $|-6(2,4)d(2,4)\rangle$ state[7]. This state allows the Feshbach molecules to be bound by $\sim$MHz. In our experiment we utilise

---

[6] For more details about good quantum numbers in molecules, see section 2.5.1

[7] Note that the -6 in this state indicates that the state is a lower vibrational state than the other two Feshbach states discussed. This is because its vibrational state is counted from the higher (2,4) threshold.

both the $|{-6}(2,4)d(2,4)\rangle$ and $|{-2}(1,3)d(0,3)\rangle$ states, the avoided crossing between these two states is shown more closely in Fig. 2.4(b) and has a critical ramp speed of ~ 70 G ms^{-1} [130].

2.4 Stimulated Raman Adiabatic Passage (STIRAP)

The process of magnetoassociation produces molecules weakly bound by only a few MHz which are relatively short lived. In addition, the electric dipole moment scales with inter-atomic separation as $d \propto r^{-7}$, and so molecules in these weakly bound states have a negligible electric dipole moment as their inter-atomic separation is large. Transfer to a more deeply bound state requires a coherent process which is state-selective, efficient and able to remove the ~ 5500 K binding energy with no heating of the molecule sample. STIRAP offers a robust method of transferring populations between quantum states [131, 132] which has been shown to be highly effective at transferring molecules to more tightly bound states in systems of both homonuclear [133] and heteronuclear molecules [26].

2.4.1 STIRAP in an Idealised 3-Level System

To achieve STIRAP in our system, we must couple both the initial weakly bound Feshbach state $|F\rangle$ and the rovibrational ground state $|G\rangle$ to a common excited state $|E\rangle$[8]. We label the optical coupling fields between $|F\rangle \leftrightarrow |E\rangle$ as the 'pump' and between $|G\rangle \leftrightarrow |E\rangle$ as the 'Stokes'. The coupling directly between states $|F\rangle$ and $|G\rangle$ is forbidden by selection rules, and so we can model this system as a three level Λ-type system as shown in

---

[8] The available intermediate excited states have very short lifetimes and have multiple decay routes open to them. Any molecules which are transferred to this excited state will therefore be lost from the experiment and so population of this state must be avoided for efficient and coherent transfer.

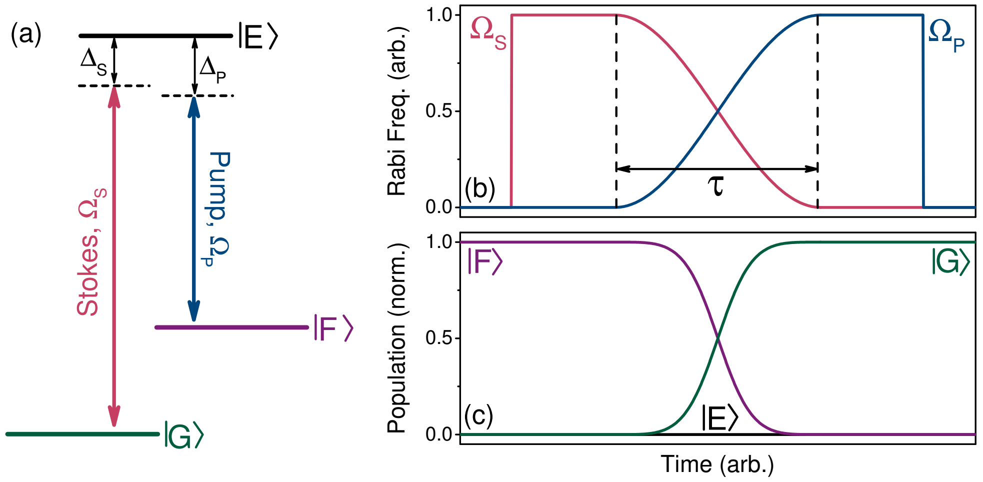

Figure 2.5: Configuration and pulse sequence for STIRAP in an idealised 3-level system. (a) Generalised 3-level Λ-type system. The coupling between the levels is given by two optical laser fields labelled as the 'pump' and 'Stokes' as outlined in the main text. (b) Pulse sequence for STIRAP to transfer molecules directly from state $|F\rangle$ to $|G\rangle$. The time for transfer is defined by the time τ. (c) Time evolution of the populations of the three states during the pulse sequence given in (b).

Fig. 2.5(a). The Hamiltonian for such a system is

$$\hat{H} = \frac{\hbar}{2}\begin{pmatrix} 0 & \Omega_{\mathrm{P}}(t) & 0 \\ \Omega_{\mathrm{P}}(t) & 2\Delta_{\mathrm{P}} & \Omega_{\mathrm{S}}(t) \\ 0 & \Omega_{\mathrm{S}}(t) & 2(\Delta_{\mathrm{P}}-\Delta_{\mathrm{S}}) \end{pmatrix}, \tag{2.17}$$

where $\Omega_{\mathrm{P}}(t)$, $\Omega_{\mathrm{S}}(t)$ are the driven Rabi frequencies, and Δ_{P}, Δ_{S} are the detunings from resonance of the pump and Stokes laser fields respectively. If we set both laser fields on two-photon resonance ($\Delta_{\mathrm{P}} = \Delta_{\mathrm{S}} = \Delta$), it can be shown that there are three analytic eigenstates for this Hamiltonian:

$$|a^+\rangle = \sin\theta\sin\phi\,|F\rangle + \cos\phi\,|E\rangle + \cos\theta\sin\phi\,|G\rangle\,, \tag{2.18a}$$

$$|a^0\rangle = \cos\theta\,|F\rangle - \sin\theta\,|G\rangle\,, \tag{2.18b}$$

$$|a^-\rangle = \sin\theta\cos\phi\,|F\rangle - \sin\phi\,|E\rangle + \cos\theta\cos\phi\,|G\rangle\,. \tag{2.18c}$$

Here, we have defined two mixing angles θ and ϕ which are defined by

$$\tan\theta = \frac{\Omega_{\mathrm{P}}}{\Omega_{\mathrm{S}}}, \tag{2.19}$$

$$\tan 2\phi = \frac{\sqrt{\Omega_{\mathrm{P}}^2 + \Omega_{\mathrm{S}}^2}}{\Delta}. \tag{2.20}$$

The eigenstate we are interested in for STIRAP is $|a^0\rangle$ (Eq. 2.18b) which describes a dark state with no intermediate state $|E\rangle$ component, as it is this state which facilitates the direct transfer between states $|F\rangle$ and $|G\rangle$.

The sequence in which the pump and Stokes lasers are pulsed on in STIRAP is often referred to as 'counter-intuitive', as the Stokes laser is active before the pump as shown in Fig. 2.5(b). However the reason for this ordering is simply a result of the necessity to initialise the molecules into the dark state. If we first consider the situation where only the Stokes laser is active, the state mixing angle θ is therefore zero and the dark state $|a^0\rangle \equiv |F\rangle$. The other two eigenstates in contrast have no $|F\rangle$ component in this circumstance. We therefore know that the molecules all populate the eigenstate $|a^0\rangle$ only. Transfer of molecules to state $|G\rangle$ is then just a case of reducing the Stokes intensity while increasing the pump intensity slowly such that the dark state is adiabatically transformed from state $|F\rangle$ to state $|G\rangle$. When only the pump laser is active, the state mixing angle θ is equal to $\pi/2$ and the dark state is entirely composed of the destination state $|G\rangle$. The time evolution of the population in the three available states throughout the STIRAP pulse sequence described in shown in Fig. 2.5(c). The sequence is completely reversible, and is used to transfer molecules back to the Feshbach state at the end of the experiment for dissociation and imaging.

2.4.2 Efficiency of STIRAP

If the population is held in the dark state throughout the transfer, the efficiency of STIRAP is 100%. In practice however, the efficiency of the transfer (P) when on two-photon resonance is reduced due to non-adiabaticity of the dark state evolution, and limitations imposed by laser decoherence, such that [134]

$$P = \exp\left(-\frac{\pi^2\gamma}{\Omega_0^2\tau} - \frac{D\tau}{2}\right). \tag{2.21}$$

Here, γ is the natural linewidth of the state $|E\rangle$, D is the linewidth associated with the frequency difference between the two lasers, τ is the transfer time (as shown in Fig. 2.5 (b)) and Ω_0 is the reduced Rabi frequency. The reduced Rabi frequency is defined as $\Omega_0 = \sqrt{\Omega_\mathrm{p}^2 + \Omega_\mathrm{S}^2}$, where Ω_p and Ω_S are the peak Rabi frequencies of the pump and Stokes transitions respectively. By minimizing the two contributions to the exponential in equation 2.21 we are able to derive the necessary condition for efficient transfer [135]:

$$\frac{\Omega_0^2}{\pi^2\gamma} \gg \frac{1}{\tau} \gg D. \tag{2.22}$$

The natural linewidth is dependent on the excited state chosen; the range of values for this term are therefore limited by the range of states accessible to the laser system. The importance of this term in defining the efficiency of the transfer highlights the need for a thorough molecular spectroscopy search in order to identify the best state to use, namely a state with high Ω_0^2/γ. This gives the first criterion which the STIRAP laser system must fulfil; it must be possible to tune both of the lasers over a wide overlapping frequency range in order to maximize the range in which a suitable excited state can be found.

In practice, Ω_0^2/γ is limited by the available laser intensity. This sets the *minimum* duration for the transfer required to remain adiabatic. This in turn sets the maximum linewidth allowed to maintain coherence of the dark state. Therefore, the second criterion is that the linewidth D associated with the frequency difference between the two lasers is minimised as this sets the *maximum* duration over which the transfer may be performed. As both of our STIRAP lasers are frequency stabilised to the same cavity we can expect that the frequency noise from the lasers are correlated, which helps to minimise this linewidth. Measuring this linewidth is non-trivial, though experimental measurements on the pump light using delayed self-heterodyne interferometry suggest a laser linewidth on each laser of the order of ~ 100 Hz [130]. In our experiment we find transitions which allow pulse durations on the order of ~ 10 μs. This indicates that the maximum linewidth for efficient transfer must be on the order of kHz.

2.5 Structure of Diatomic Molecules

Due to the additional degrees of freedom available, molecules possess not only electronic energy states, but also rotational and vibrational states. Each degree of freedom operates on a different energy scale. To drive transitions between electronic energy states requires energies in the optical or near-infra-red regime (~ 100 THz). Meanwhile vibrational transitions take place in the infra-red (~ 1 THz) and rotational transitions using microwaves (~ 1 GHz)

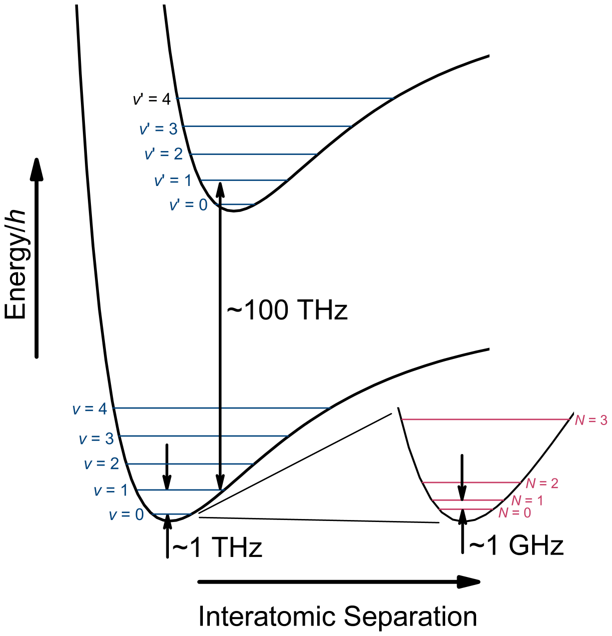

Figure 2.6: Illustration of the different energy levels present in molecules with the required energies for transitions between each labelled. Good quantum numbers which may be used to describe each of these states are discussed in the main text. Hyperfine structure is not shown; each rotational level is in fact split into $(2N+1)(2I_{\mathrm{Rb}}+1)(2I_{\mathrm{Cs}}+1)$ as explained in section 2.5.3.

(see Fig. 2.6). Here we will investigate each of these degrees of freedom with particular attention made to the notation used to accurately describe each of these levels.

In order to simplify our discussion of molecular structure, we must first make two key assumptions. The first is that when we associate atoms into molecules, the inner electron shells are unperturbed. Only the outer valence electrons are therefore distributed throughout the molecule to give the binding force [106]. The second is known as the *Born-Oppenheimer approximation* which allows us to approximate the nuclei as being at fixed positions within the molecule. This approximation requires that the masses of the nuclei are much larger than that of the electron and so the motion of the nuclei is therefore slow compared to that of the electron.

2.5.1 Hund's Cases and Electronic Structure

Good quantum numbers rely upon the way in which the electronic and nuclear angular momenta couple to each other. For a ^{87}Rb^{133}Cs molecule, there are various sources of angular momenta which have quantum numbers associated with them: [36]

L - Electronic orbital angular momentum; $\vec{L} = \vec{l_{\mathrm{Rb}}} + \vec{l_{\mathrm{Cs}}}$.

S - Electronic spin angular momentum; $\vec{S} = \vec{s_{\mathrm{Rb}}} + \vec{s_{\mathrm{Cs}}}$.

J - Total angular momentum; $\vec{J} = \vec{L} + \vec{S} + \vec{R}$.

N - Total angular momentum excluding electron spin; $\vec{N} = \vec{J} - \vec{S}$.

R - Rotational angular momentum of the nuclei; $\vec{R} = \vec{J} - \vec{S} - \vec{L}$.

I - Total Nuclear spin angular momentum; $\vec{I} = \vec{I_{\mathrm{Rb}}} + \vec{I_{\mathrm{Cs}}}$.

These sources of angular momenta may couple in a variety of ways which are described by the Hund's coupling cases. There are a total of five possible coupling cases though only the cases (a) and (c) are relevant for the description of the ^{87}Rb^{133}Cs molecule. These cases are shown schematically in Fig. 2.7.

In Hund's case (a), the orbital angular momentum $\vec{L}$ strongly couples to the internuclear axis by electrostatic forces and the electron spin angular momentum $\vec{S}$ is in turn strongly coupled to $\vec{L}$ through spin-orbit coupling. The projections of $\vec{L}$ and $\vec{S}$ onto the internuclear axis are given as $\vec{\Lambda}$ and $\vec{\Sigma}$ respectively and their sum is $\vec{\Omega} = \vec{\Lambda} + \vec{\Sigma}$. The rotational angular momentum of the nuclei $\vec{R}$ is coupled to $\vec{\Omega}$ and together they form the total angular momentum $\vec{J}$. Good quantum numbers for this case are $\Lambda, \Sigma, S, J, \Omega$.

In Hund's case (c), the coupling between $\vec{L}$ and $\vec{S}$ is stronger than the interaction with the internuclear axis. Their individual projections onto the internuclear axis are therefore not defined and we instead couple $\vec{L}$ and $\vec{S}$

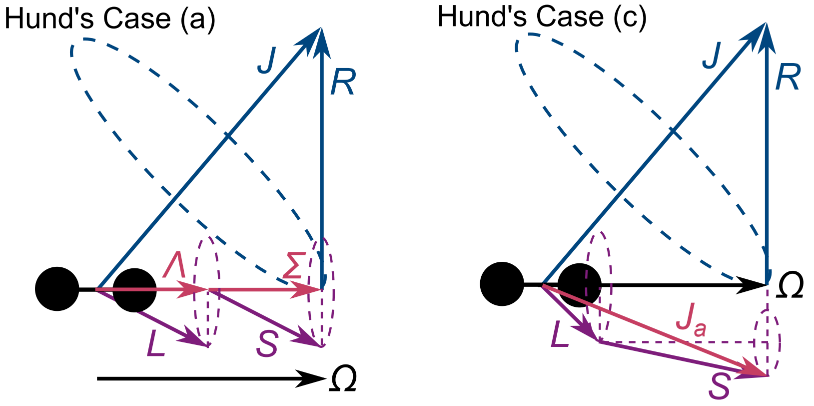

Figure 2.7: Coupling of angular momentum in Hund's cases (a) and (c) which are relevant to the ^{87}Rb^{133}Cs molecule.

to form the vector $\vec{J_a} = \vec{L} + \vec{S}$. The projection of this sum $\vec{J_a}$ onto the internuclear axis defines $\vec{\Omega}$ which couples to the rotational momentum $\vec{R}$ to form the total angular momentum $\vec{J}$. Good quantum numbers for this case are J_a, Ω, J.

The electronic states of the molecule can be fully described by the notation

$$^{2S+1}\Lambda^{\pm}_{\Omega}. \tag{2.23}$$

In analogy with the case of spectroscopic notation for atoms, the quantum number Λ is given the label Σ, Π, Δ... for $\Lambda = 0, 1, 2$.... The superscript $^{\pm}$ refers to the reflection symmetry in an arbitrary plane which contains the internuclear axis. This notation is often preceded by a term value equivalent to the principle quantum number in atoms, where X denotes the ground state.

The Feshbach states lie in a shallow triplet $a^3\Sigma^+$ potential while the rovibronic ground state $X^1\Sigma^+$ has singlet character. Our transfer between these two states relies on the fact that not all states in our system are well described by a single Hund's case, as the selection rule $\Delta S = 0$ would deny coupling between these levels. Fortunately, strong spin-orbit coupling causes mixing of the $A^1\Sigma^+$ and $b^3\Pi^+$ states [136–139] and common vibrational levels of the two states exist that have mixed singlet and triplet character. It is one these levels which we use as an intermediate levels in our STIRAP [29, 130, 140].

2.5.2 Vibrational Structure

The internuclear potential of a diatomic molecule is roughly harmonic near the bottom of the well. We can hence approximate molecular vibrations as the solutions to a simple harmonic oscillator with an added correction term to account for the anharmonicity of the potential at higher energies. Given this approximation, the vibrational energy can be written for a given wavenumber (ω_e) and associated energy

$$E(v) = \omega_e(v + \frac{1}{2}) - \omega_e\chi_e(v + \frac{1}{2})^2, \tag{2.24}$$

where v is the vibrational quantum number and χ_e is an constant which describes the anharmonicity of the molecular potential. We expect that low-lying vibrational levels will be evenly spaced by the energy determined by the wavenumber. In ^{87}Rb^{133}Cs, this spacing between the vibrational ground state and first vibrationally excited state $v = 0 \rightarrow v = 1$ has been measured to be 1.49270 THz (or 49.7911 cm^{-1}). In addition, the highest vibrational level in the electronic ground state has been determined to be either $v = 136$ or $v = 137$ by experimental measurements using the technique of laser-induced fluoresence combined with Fourier-transform spectroscopy [141].

2.5.3 Rotational and Hyperfine Structure

A diatomic molecule such as ^{87}Rb^{133}Cs is allowed to rotate around any axis which passes through its centre of mass. At low rotational energies, the behaviour of the molecule may be likened to that of a rigid rotor and in this case the separation of rotational levels is defined by the rotational constant B_v of the molecule such that

$$E(N) = B_vN(N + 1), \tag{2.25}$$

where N is the rotational quantum number. In ^{87}Rb^{133}Cs, this rotational constant has been previously measured to be 490.155(5) MHz [141] by spectroscopic measurements, and we present an improved measurement of this quantity later in this work. A real molecule however is not rigid and when it rotates, an apparent centrifugal force acts on the atoms to increase the internuclear separation. This centrifugal distortion becomes greater as the rotational energy of the molecule increases and leads to a rotational energy level structure of the form

$$E(N) = B_v N(N+1) - D_v N^2(N+1)^2 + ..., \tag{2.26}$$

where D_v is the centrifugal distortion constant. Note there are higher order terms available in this expression [142] but these are not experimentally relevant to the low-lying rotational levels investigated in this work. The centrifugal distortion constant for ^{87}Rb^{133}Cs has been previously measured as 213.0(3) Hz [141]. This is a relatively small correction, being six orders of magnitude smaller than the rotational constant.

The hyperfine structure of a single rotational level in a diatomic molecule is tremendously complicated and the number of levels depends upon the magnetic field and the spins of the component nuclei. The nuclear spins of ^{87}Rb^{133}Cs are $I_{\text{Rb}} = 3/2$ and $I_{\text{Cs}} = 7/2$. At zero magnetic field, the total nuclear spin $\vec{I} = \vec{I_{\text{Rb}}} + \vec{I_{\text{Cs}}}$ is conserved, and in the rotational ground state this leads to 4 hyperfine states with $I = 2, 3, 4$, and 5. The application of an external magnetic field however splits each rotational manifold into $(2N+1)(2I_{\text{Rb}}+1)(2I_{\text{Cs}})$ Zeeman-hyperfine sublevels, so there are 32 levels for in the rotational ground state and 96 levels for in the first rotationally excited state. The rotational and hyperfine Zeeman structure of ^{87}Rb^{133}Cs is shown in Fig. 2.8. Full control of the molecular state down to these hyperfine levels is crucial for the majority of the proposed applications for ultracold polar molecules.

In this work we calculate the rotational and hyperfine energy level structure of ^{87}Rb^{133}Cs in the electronic and vibrational ground state by diagonalizing the Hamiltonian [36, 143–145]

$$\hat{H} = \hat{H}_{\text{r}} + \hat{H}_{\text{hf}} + \hat{H}_{\text{Z}}, \tag{2.27}$$

where

$$\hat{H}_{\text{r}} = B_v\vec{N}^2 - D_v\vec{N}^2\vec{N}^2, \tag{2.28a}$$

$$\hat{H}_{\text{hf}} = \sum_{i=\text{Rb,Cs}} \vec{V_i}\cdot\vec{Q_i} + \sum_{i=\text{Rb,Cs}} c_i\vec{N}\cdot\vec{I_i} + c_3\vec{I}_{\text{Rb}}\cdot\vec{T}\cdot\vec{I}_{\text{Cs}} + c_4\vec{I}_{\text{Rb}}\cdot\vec{I}_{\text{Cs}}, \tag{2.28b}$$

$$\hat{H}_{\text{Z}} = -g_r\mu_{\text{N}}\vec{N}\cdot\vec{B} - \sum_{i=\text{Rb,Cs}} g_i(1-\sigma_i)\mu_{\text{N}}\vec{I_i}\cdot\vec{B}. \tag{2.28c}$$

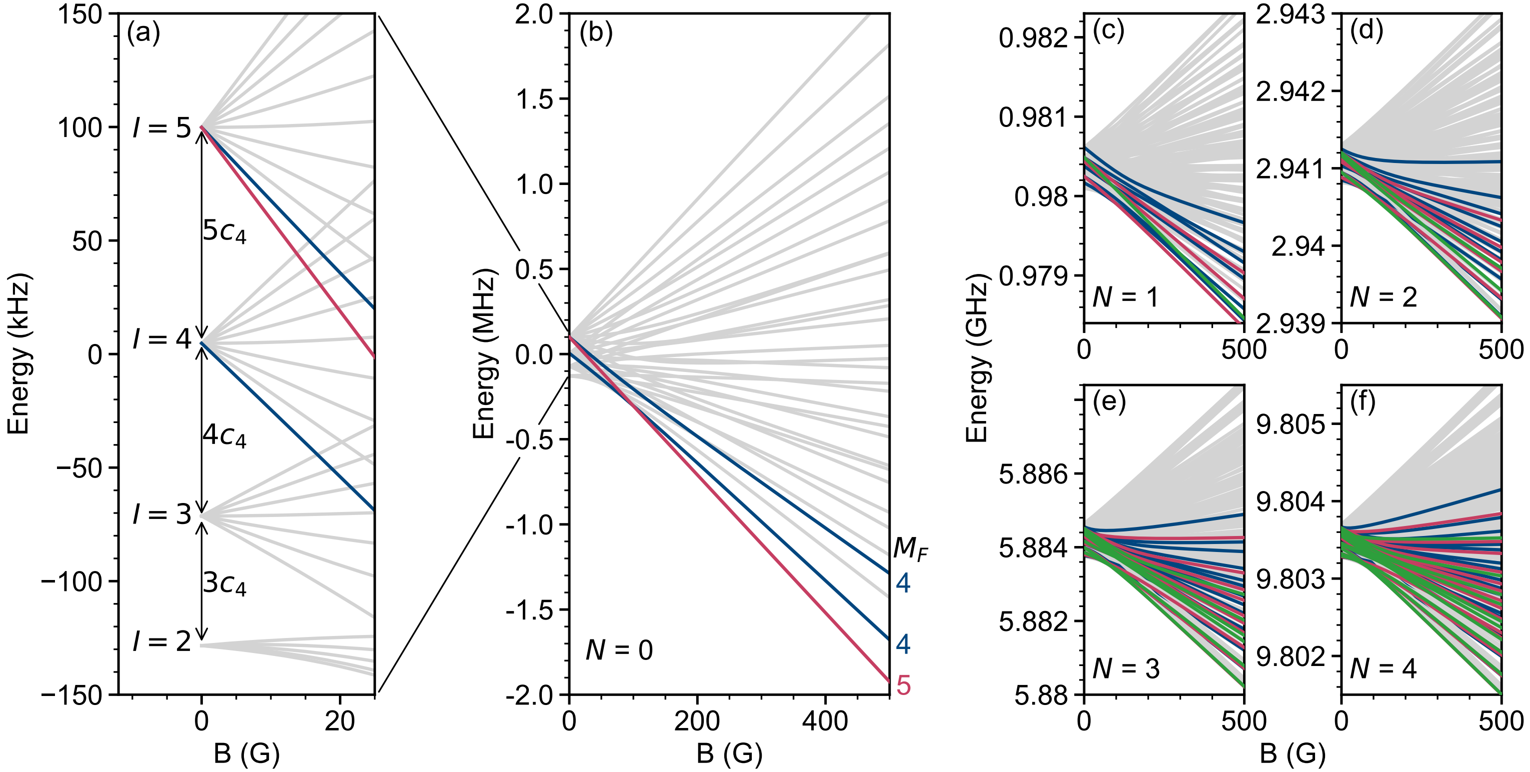

Figure 2.8: Hyperfine and Rotational Zeeman Structure of ^{87}Rb^{133}Cs. The rotational ground state $N = 0$ has $(2M_N + 1)(2m_I^{\mathrm{Rb}} + 1)(2m_I^{\mathrm{Cs}} + 1) = 32$ hyperfine components. (a) At zero magnetic field, many of these states are degenerate leaving only 4 hyperfine states which are separated by multiples of $c_4 = 19$ kHz as shown. These states correspond to different values of the total nuclear spin I. (b) The application of a magnetic field splits these states, such that at high magnetic field good quantum numbers are given by M_N, m_I^{Rb}, m_I^{Cs}. The quantum number $M_F = M_N + m_I^{\mathrm{Rb}} + m_I^{\mathrm{Cs}}$ is conserved in all magnetic field regimes, and is the only good quantum number at the main magnetic field regime investigated in this work $B \sim 181.5$ G. States with $M_F = 4, 5, 6$ have been highlighted in blue, red and green respectively. The hyperfine structure for (c) $N = 1$, (d) $N = 2$, (e) $N = 3$, (f) $N = 4$ is also shown.

The rotational contribution H_{r} (Eq. 2.28a) is defined by the rotational angular momentum of the molecule $\vec{N}$, and the rotational and centrifugal distortion constants B_v and D_v. The hyperfine contribution H_{hf} (Eq. 2.28b) consists of four terms. The first describes the electric quadrupole interaction with coupling constants $(eqQ)_{\mathrm{Rb}}$ and $(eqQ)_{\mathrm{Cs}}$, while the second is the interaction between the nuclear magnetic moments and the magnetic field generated by the rotation of the molecule, with spin-rotation coupling constants c_{Rb} and c_{Cs}. The final two terms represent the tensor and scalar interactions between the nuclear magnetic moments, with tensor and scalar spin-spin coupling constants c_3 and c_4 respectively. Finally, the Zeeman contribution H_{Z} (Eq. 2.28c) consists of two terms which represent the rotational and nuclear interaction with an externally applied magnetic field. The rotation of the molecule produces a magnetic moment which is characterized by the rotational g-factor of the molecule (g_r). The nuclear interaction similarly depends on the nuclear g-factors (g_{Rb}, g_{Cs}) and nuclear shielding (σ_{Rb}, σ_{Cs}) for each species. Note, this Hamiltonian does not consider the application of external electric fields, this would require the addition of a further Stark contribution to the Hamiltonian and significantly complicate the spectra [146]. The effect of DC and AC electric fields on molecules in states with well defined M_N is considered in the following section.

2.6 Polar Molecules

Access to relatively long-range dipole-dipole interactions is a key motivator for the creation of ultracold systems of molecules. Heteronuclear alkali metals in their absolute ground state possess a large electric dipole moment but a practically negligible magnetic dipole moment. The theoretical discussion in this section will therefore be limited to a discussion of the behaviour of electric dipoles only. It is important to note throughout that no state with well-defined parity can possess a space-fixed dipole moment. A superposition of opposite-parity states must be created to induce a dipole moment, either by applying an external electric field or by driving microwave transitions between neighbouring rotational states.

		M_N			
		0	±1	±2	±3
N	3		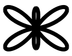		
	2				
	1				
	0				

Table 2.3: Probability distribution (P, θ) for a rigid rotator in various states specified by the rotational quantum number (N) with projection along the z-axis (m_N). Coupling between states by electric field can only occur when $\Delta N = \pm 1$, $\Delta M_N = 0$. Each plot is a 2D slice through the probability distribution, with the symmetry axis running vertically through the centre of each plot.

2.6.1 Polar Molecules in DC Electric Fields

The application of an external DC electric field couples rotational states of opposite parity to induce a dipole moment in the laboratory frame of reference. We can demonstrate this by considering the diatomic molecule to be similar in behaviour to that of a rigid rotor, where the atoms are treated as point masses separated by a distance (r) as is generally applicable to all diatomic molecules in low-lying rotational energy levels (see 2.5.3). It can be shown that such a system has eigenfunctions (Ψ_r) in polar coordinates $(\theta,\ \phi)$ given by [147],

$$\Psi_r = A_0\ P_N^{|m_N|}(\cos\theta)\ \mathrm{e}^{i m_N \phi}, \tag{2.29}$$

where A_0 is a normalisation constant, N is the rotational quantum number with its projection onto the z-axis M_N, and $P_N^{|M_N|}(\cos\theta)$ is the associated Legendre polynomial. This equation has an associated quantum mechanical probability distribution $(P = \Psi^{*}\Psi)$ which is different for each value of the rotational quantum number. The probability distributions for rotational quantum numbers up to $N = 3$ has been plotted in Table 2.3.

The rigid rod model can be adapted for polar molecules by considering the masses on the ends of the rod carrying a different charge. The centre of the charge distribution is then no longer located at the centre of the rod.

The hamiltonian in the basis of $|N, M_N\rangle$ for such an unevenly charged rigid rod in an electric field is made up of two terms. The first term describes the rotational energy of the rigid rod structure without the presence of an electric field, the second describes the Stark effect[9] [68].

$$\begin{aligned}\langle N, M_N| \hat{H} |N', M'_N\rangle &= B \cdot N(N+1) \cdot \delta_{NN'M_NM'_N} \\ -d_0E\sqrt{(2N+1)(2N'+1)} \cdot (-1)^{M_N} \cdot &\begin{pmatrix} N & 1 & N' \\ -M_N & 0 & M'_N \end{pmatrix} \begin{pmatrix} N & 1 & N' \\ 0 & 0 & 0 \end{pmatrix},\end{aligned} \tag{2.30}$$

Here, d_0 is the molecule-frame electric dipole moment, B is the rotational constant of the molecule, and E is the magnitude of the applied electric field. The matrices in the equation are Wigner 3-j coefficients. They ensure that the electric field only 'mixes' states with the same M_N, and that the $|N, M_N\rangle$, $|N, -M_N\rangle$ are degenerate. Hence, the electronic ground state $|1, 0\rangle$ will mix with all of the $|N, 0\rangle$ levels. Increasing the magnitude of the electric field leads to a greater contribution from the coupling term.

Diagonalising the Hamiltonian given in 2.30 yields the Stark map for the rotational energy structure shown in Fig. 2.9. using the predicted parameters for ^{87}Rb^{133}Cs ($d_0 = 1.28$ D [80], $B = 0.51$ GHz [141]). For each energy level, the space-fixed dipole moment is given by the gradient of the curve presented in the plot (i.e. the rate of change in energy of the state with respect to the applied electric field). The space fixed dipole moment for the lowest two rotational states can be seen in Fig. 2.10(a). Experimental measurement of the Stark shift of one of these states can therefore be used to measure the electric dipole moment in the molecular frame (see 4.6). In order for such a measurement to be accurate, we must consider the number of rotational levels which must be included in the calculation for adequate convergence to the correct solution within the uncertainty required. In Fig. 2.10, we demonstrate how the number of rotational levels included in the calculation changes the calculated dipole moment for the rovibrational ground state at large electric fields. Fortunately, it is clear that the coupling is dominated

---

[9] Here we are neglecting the centrifugal distortion term D amongst all other higher order terms in equation 2.26 as part of our approximation of treating the molecule as a 'rigid' rotor. This is valid as we are only considering low-lying rotational levels.

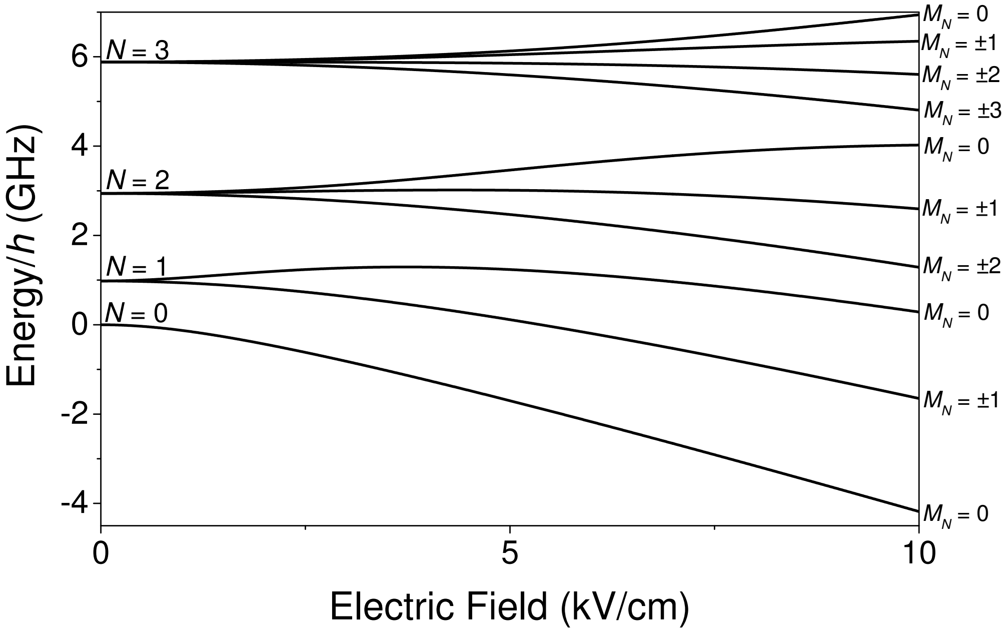

Figure 2.9: Stark shift of the lowest four rotational states $N = 0, 1, 2, 3$ of a rigid rotor-like polar molecule. The application of an external electric field 'mixes' states of opposite parity and splits each rotational state into $N + 1$ hyperfine levels each corresponding to a different value of the projection $|M_N|$.

by the low-lying rotational states and convergence quickly occurs with only $N < 6$ required for reasonable accuracy.

2.6.2 Polar Molecules in Microwave Fields

The dipole induced by applying an electric field is a result of a superposition of states of opposite parity. Unfortunately however, the magnitude of the field required is of the order of 10 kV cm^{-1} which can often be experimentally difficult. Since neighbouring rotational levels have opposite parity, an alternative approach is to engineer a superposition of opposite parity states by coupling two of these neighbouring rotational states with a resonant microwave field. With the molecules starting in the rotational ground state, the easiest superposition to prepare is between $N = 0$ and $N = 1$ rotational levels. The dipole moment operator is

$$\hat{d} = d_0\sqrt{(2N+1)(2N'+1)} \cdot (-1)^{M_N} \cdot \begin{pmatrix} N & 1 & N' \\ -M_N & M & M'_N \end{pmatrix} \begin{pmatrix} N & 1 & N' \\ 0 & 0 & 0 \end{pmatrix}, \tag{2.31}$$

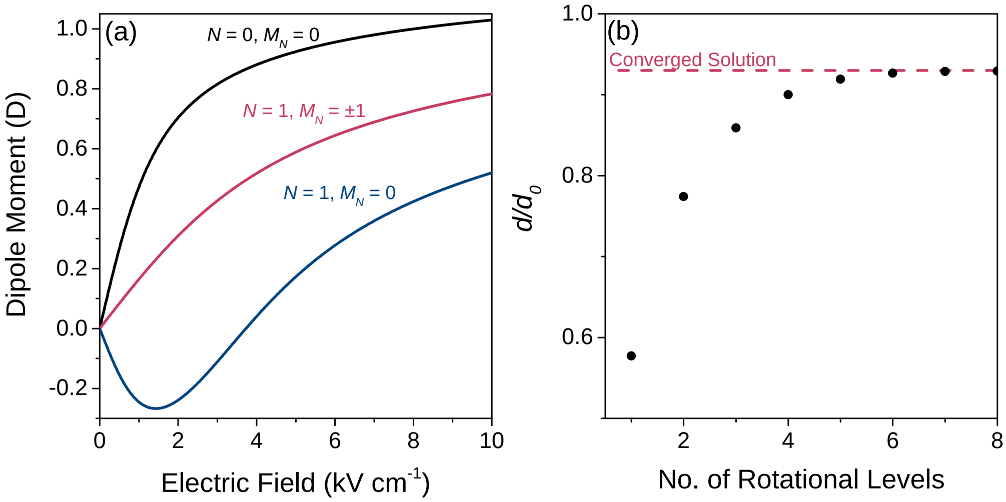

Figure 2.10: Space-fixed dipole moment calculations in the rigid rotor model. (a) Variation of space-fixed dipole moment with applied electric field for the lowest two rotational states $N = 0, 1$. (b) Calculated induced dipole moment at large electric field as a function of the number of rotational levels included in the calculation. Typically only $N < 6$ is required for reasonable accuracy.

where $M = M_N - M'_N$ to account for the allowed superpositions between states with different M_N. A 50:50 superposition of the $N = 0$ and $N = 1$ states will therefore have a dipole moment of $d_0/\sqrt{3}$, and this dipole moment persists even after the resonant field has been removed. For ^{87}Rb^{133}Cs, this is equal to $d_0/\sqrt{3} \approx 0.7$ D. To achieve this using DC electric fields in the rotational ground state would require an electric field of 2 kV cm^{-1}.

2.6.3 Interacting Dipoles

We consider the general case of two interacting particles each with relative position $\vec{r} = r\hat{r}$, and with common dipole moments d pointed along the unit vectors $\hat{e_1}$ and $\hat{e_2}$ respectively as shown in Fig. 2.11(a). The potential energy V_{dd} between these two particles due to their dipole-dipole interactions is

$$V_{\text{dd}}(\vec{r}) = \frac{d^2}{4\pi\epsilon_0}\frac{\hat{e_1}\cdot\hat{e_2} - 3(\hat{e_1}\cdot\hat{r})(\hat{e_2}\cdot\hat{r})}{r^3}, \tag{2.32}$$

where ϵ_0 is the permittivity of free space. If these dipoles are fixed parallel to each other as in Fig. 2.11(b) then this expression simplifies to

$$V_{\text{dd}}(\vec{r}) = \frac{d^2}{4\pi\epsilon_0}\frac{1 - 3\cos^2\theta}{r^3}, \tag{2.33}$$

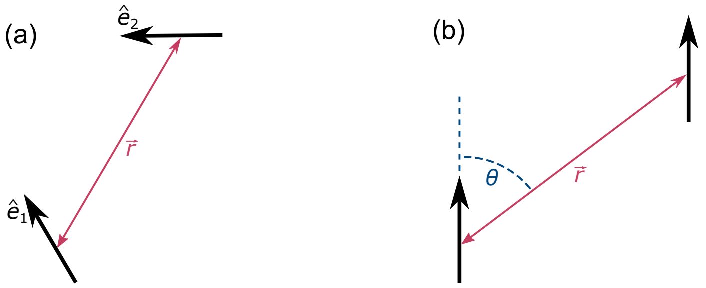

Figure 2.11: General case of two interacting dipoles. (a) Unaligned dipoles where each particle has its respective dipole moment pointed along a unit vector $\hat{e}$. The particles are separated by a vector $\vec{r} = r\hat{r}$. (b) Aligned dipoles where the two dipole moments are parallel to each other, and θ is the angle between the dipole moments and the particles' relative position vector $\vec{r}$.

where θ is the angle between the dipole moments and the particles' relative position vector. This form highlights the two key features of dipole-dipole interactions; the interaction is anisotopic (i.e. depends on θ) and is relatively long ranged (scales as $1/r^3$).

In the context of ^{87}Rb^{133}Cs molecules confined to an optical lattice, given a lattice spacing of 532 nm and molecule frame dipole moment of $d_0/\sqrt{3} = 0.7$ D, we can use Eq. 2.33 to calculate the interaction strength between spin-polarised molecules on neighbouring lattice sites. Head-to-tail interactions are attractive with $V_{\mathrm{dd}}/h = -960$ Hz ($V_{\mathrm{dd}}/k_{\mathrm{B}} = -46$ nK), and side-to-side interactions are repulsive with $V_{\mathrm{dd}}/h = +480$ Hz ($V_{\mathrm{dd}}/k_{\mathrm{B}} = +23$ nK). These interactions are relatively large compared to existing magnetic dipolar systems, and are an order of magnitude larger than those accessible in the equivalent ^{40}K^{87}Rb system where dipolar spin-echange interactions between lattice confined molecules have already been observed using Ramsay interferometry [74]. In addition, energy shifts of this magnitude are significantly larger than the natural linewidth of the rotational and hyperfine states of the molecule, and given sufficient spectroscopic resolution could lead to effects equivalent to Rydberg blockade [15].

In the work presented in this thesis, molecules are trapped in a 3D optical potential with a peak density of $\sim 10^{11}$ cm^{-3}. Given the average separation of molecules at this density, we would expect interaction strengths of around $V_{\mathrm{dd}}/h \sim \pm 10$ Hz for molecules with a dipole moment of $d_0/\sqrt{3} \approx 0.7$ D.

To see how dipole-dipole interactions affect the system in the 3D case, it is perhaps more instructive to compare the energy scale of the dipole-dipole interaction to that of short-ranged contact interactions which depend upon the s-wave scattering length a. We can define an effective dipole length scale (a_{dd}), by equating a typical centrifugal energy $\hbar^2/(ma_{\mathrm{dd}}^2)$ to the dipole interaction energy in equation 2.33 such that

$$a_{\mathrm{dd}} = \frac{d^2 m}{4\pi\epsilon_0\hbar^2}, \tag{2.34}$$

which may be compared to the s-wave scattering length. For ^{87}Rb^{133}Cs, the full molecule-frame dipole moment leads to $a_{\mathrm{dd}} = 3.4 \times 10^4\ a_0$. Although the s-wave scattering length between the molecules has yet to be measured, the dipolar length is significantly larger than the contact interactions in either atomic species and this indicates that the dominant interactions between molecules will likely be dipolar. During a collision, the relative orientation between the two molecules will have strong effects as the dipole-dipole interaction serves to raise or lower the barrier for collisions depending on whether the interaction is attractive or repulsive. This has been investigated as a means of either encouraging or suppressing reactive collisions in ^{40}K^{87}Rb. With the molecules trapped in pancake-shaped optical dipole trap, the molecules were polarised along the tight axis of the trap by a DC electric field. The ratio of trap frequencies in the optical trap is not sufficiently high to restrict collisions to two dimensions, but rather collisions occur more often along the tighter axis of the trap due to the higher trap frequency. In this case, collisions become predominantly attractive head-to-tail and the collision rate is observed to increase [72]. Suppression of collisions can be similarly achieved but requires a geometry which favours side-to-side repulsive collisions.

Chapter 3

Experimental Apparatus

In this chapter we will discuss the experimental apparatus used throughout this thesis. The majority of the experiment has been built and documented by previous students working on the experiment [96–101], so only a brief overview will be given here paying particular attention to the continued maintenance and running of the experiment. This is one of the key challenges when inheriting an experiment from a previous generation of PhD students and one which should not be taken lightly! I will also highlight some important additions to the experiment, specifically the relatively new STIRAP laser system (3.2.3), the addition of DC electric fields (3.4) to orient the molecule electric dipole moments, and microwave radiation (3.5) to probe the hyperfine and rotational structure of the deeply-bound molecules.

3.1 Vacuum System

Our experiment comprises of a two chamber vacuum system. The first houses a pyramid MOT which is loaded directly from dispensers and acts as a cold dual-species atom source for the second ‘science’ chamber. The pyramid MOT has been shown to be highly robust with little to no maintenance required over several years. The second chamber is a cell constructed from 2 mm thick fused silica with internal dimensions of 20 mm×20 mm×83 mm. Each chamber has its own ion pump (40 $\mathrm{l\ s^{-1}}$ for the pyramid chamber, 55 $\mathrm{l\ s^{-1}}$ for the science chamber), while the science chamber also has a non-

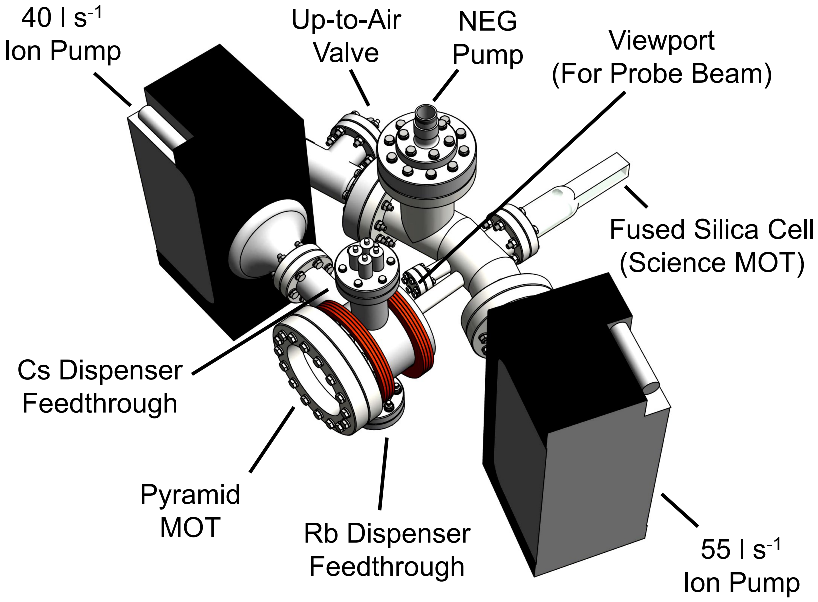

Figure 3.1: Vacuum system used in this work consisting of two chambers each containing their own MOT. The first, a pyramid MOT, acts as a cold dual-species atom source for the second labelled as the science MOT.

evaporable getter (NEG) pump; a factor of $\sim$ 100 pressure differential is maintained between the two [97]. A diagram of the experimental apparatus may be seen in Fig. 3.1.

At present, although the fused silica cell provides excellent optical access, the necessary optics to create a MOT in the science chamber means that access is still at a premium. To remedy this, and to improve the vacuum quality where the molecules are created, a future iteration of the experiment is planned. This will have three chambers with magnetic transport of cold atoms in a quadrupole potential between the second and third chambers similar to that used in [148].

3.2 Laser Systems

Multi-species experiments can have highly complex laser requirements as each species must be addressed independently. In this section we will discuss the laser systems used to laser cool an atomic mixture of ^{87}Rb and ^{133}Cs, optically trap both species together, and to transfer weakly-bound molecules

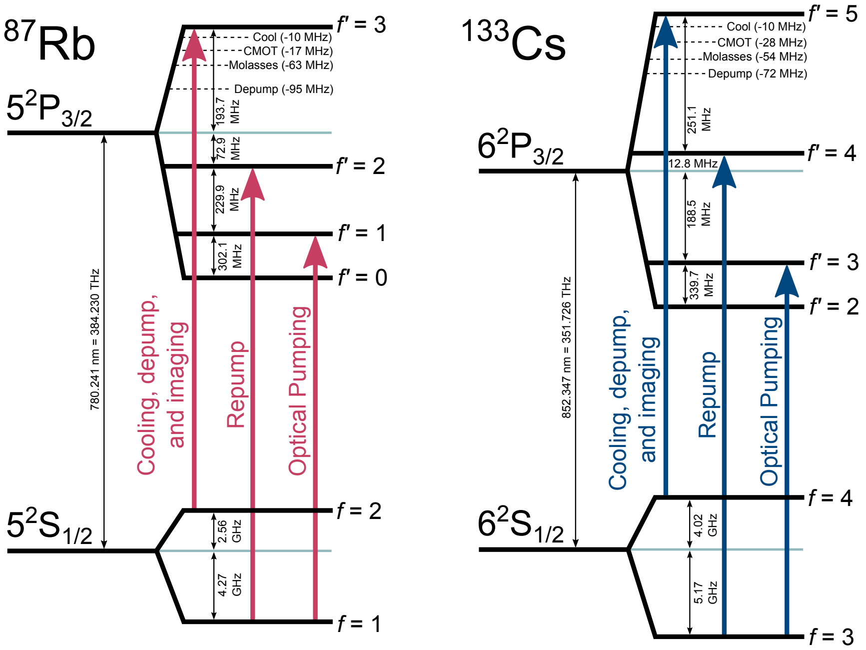

Figure 3.2: Energy level scheme for the D_2 lines in ^{87}Rb and ^{133}Cs atoms. Laser frequencies used in this work are labelled. The cooling light for both species is detuned dynamically during the experimental sequence and is used to depump the atoms during the optical pumping stage.

produced by magnetoassociation to the rovibronic ground state.

3.2.1 Cooling, Optical Pumping, and Imaging

A dual-species experiment requires two complete laser systems to generate light for cooling and repumping in the magneto-optical trap, optical pumping prior to magnetic trapping, and for absorption imaging of both species. The systems developed in our experiment are identical for ^{87}Rb and ^{133}Cs and are built on the same optical breadboard. Light for both species utilises the D_2 transition ($S_{1/2} \rightarrow P_{3/2}$) at 780 nm and 852 nm for ^{87}Rb and ^{133}Cs respectively. Light is passed from the laser system to the main experiment through polarisation maintaining optical fibres. The ^{87}Rb system may also be easily adapted for ^{85}Rb [129, 149]. The frequencies of light required in our experiment are shown in Fig. 3.2.

The cooling and imaging light in the science MOT for each species is generated by a Toptica DL100 extended cavity diode 'master' laser, which is frequency stabilised to $f_{\text{Rb}} = 2 \rightarrow f'_{\text{Rb}} = 3$ ($f_{\text{Cs}} = 4 \rightarrow f'_{\text{Cs}} = 5$) using a signal obtained from modulation transfer spectroscopy in a room temperature vapour cell [150]. The laser frequency is offset from the atomic transition by $\sim$ 200 MHz due to a double-pass acousto-optic modulator (AOM) between the laser and the spectroscopy setup. Light sent to the experiment is then shifted back to near-resonance using a second double-pass AOM before the optical fibre. This allows controllable detuning of the light from the cooling transition by varying the modulation frequency on the second AOM. Extra-cooling light for the pyramid MOT is supplied by seeding an additional slave laser with $\sim$100 µW of light from the master laser. The repump and optical pumping light for each species comes from a home-built external cavity diode laser frequency stabilised to the $f_{\text{Rb}} = 1 \rightarrow X'_{\text{Rb:1,2}}$ ($f_{\text{Cs}} = 3 \rightarrow X'_{\text{Cs:3,4}}$) crossover resonance using an error signal created by frequency modulation spectroscopy [151]. Single-pass AOMs are used to shift the frequency onto resonance with $f_{\text{Rb}} = 1 \rightarrow f'_{\text{Rb}} = 2$ ($f_{\text{Cs}} = 3 \rightarrow f'_{\text{Cs}} = 4$) for repump and $f_{\text{Rb}} = 1 \rightarrow f'_{\text{Rb}} = 1$ ($f_{\text{Cs}} = 3 \rightarrow f'_{\text{Cs}} = 3$) for optical pumping. The power from each homebuilt laser is enough to supply repump light for both the pyramid and science MOTs, as well as light for optical pumping in the science cell.

3.2.2 Optical Trapping

After evaporation in the magnetic quadrupole trap, the atoms (and subsequently produced molecules) are loaded into an optical dipole trap. The light for this trap is provided by a single-frequency IPG Photonics ELR-30LP-SF fibre laser with a maximum output power of 30 W at 1550 nm. The 1550 nm light is split into two beams on a polarising beam splitter. The intensity of each beam is independently controlled using separate AOMs via an active feedback loop. The input signal for this feedback comes from photodiodes which monitor the light leaked through the back of mirrors along each beam path. Each AOM is driven with a fixed modulation frequency of 50 MHz, though the light in one beam is shifted up in frequency while the other is shifted down in frequency in order to avoid standing wave effects in the crossed beam region. $\lambda/2$ waveplates are positioned in each beam path to

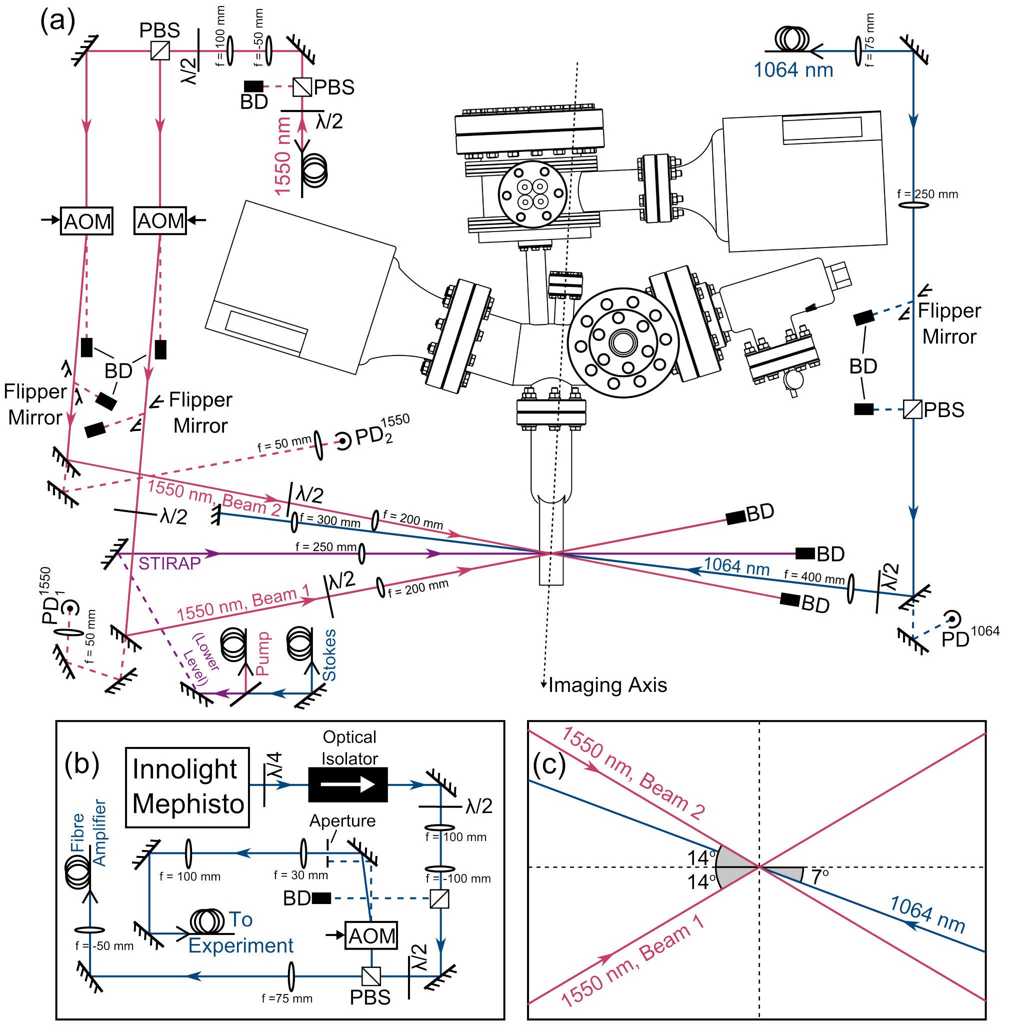

Figure 3.3: Dipole trapping and STIRAP optical layout. (a) Layout of the dipole trapping and STIRAP beams around the vacuum apparatus. Both 1550 nm beams are derived from a single erbium fibre laser. The power in each beam is independently controlled using separate AOMs. (b) A single retro-reflected beam of 1064 nm light is produced by an Nd:YAG non-planar ring oscillator (Innolight Mephisto). The output of this laser is split along two paths. The first passes through an AOM for control of the power before it is fibre coupled and sent to the experiment. The second path leads to a fibre amplifier which will be used to enable higher laser powers in the future. (c) Crossing angles of the trapping beams close to the centre of the glass science cell.

enable control of the polarisation as shown in Fig. 3.3. Up to ∼ 6 W of power is available in each beam.

When the dipole trap was first constructed, the crossing angle of the beams was measured to be ∼ 22° using knife edge measurements to track the po-

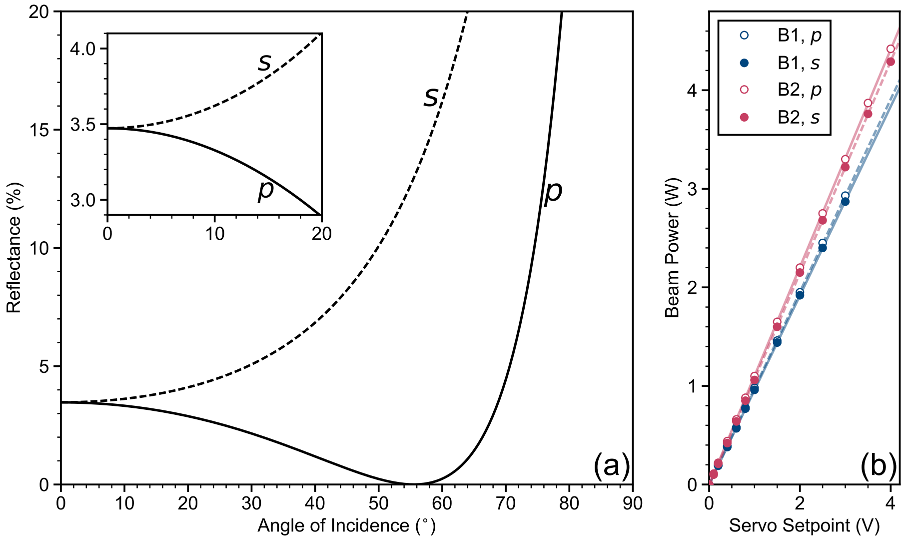

Figure 3.4: Measurement of the dipole trap beam crossing angle using reflectance of light from the uncoated walls of the fused silica cell. The refractive index of the glass is 1.455 for 1550 nm wavelength light. (a) Dependence of reflectance on the angle of incidence and light polarisation. (b) Measurement of beam power with varying the setpoint of the servo. The difference in gradient gives the difference in power after the cell for each polarisation.

sition of one beam relative to the other [98]. However, as the design of the experiment has evolved, the trap has been realigned on many occasions and the crossing angle has been changed to accommodate new optics such as those used to focus STIRAP light onto the molecules [101]. Accurate measurement of this crossing angle using knife edge measurements is non-trivial on a crowded optical table, so we therefore estimate the beam crossing angle by measuring the reflectance R of the light from the walls of the glass cell. Fig. 3.4(a) shows the dependence of the reflectance of fused silica on the angle of incidence and light polarisation. To measure the angle at which the beam meets the wall of the cell, we measure the power transmitted through the cell for both s and p laser polarisations as shown in Fig. 3.4(b). The total transmission $T \propto (1-R)^4$, as the light must pass through both walls of the cell and hence encounters 4 optical surfaces. In our experiment we find a transmitted power ratio $P_s/P_p = 1.019(1)$ and $1.028(1)$, which correspond to angles of incidence of $\sim 12.5°$ and $\sim 15°$ for beams 1 and 2 respectively (see Fig. 3.3 for beam labelling convention). The angle at which the beams intersect each other is simply equal to the sum of the angles of incidence at which they meet the cell. This crossing angle is $\sim 27.5°$, considerably larger

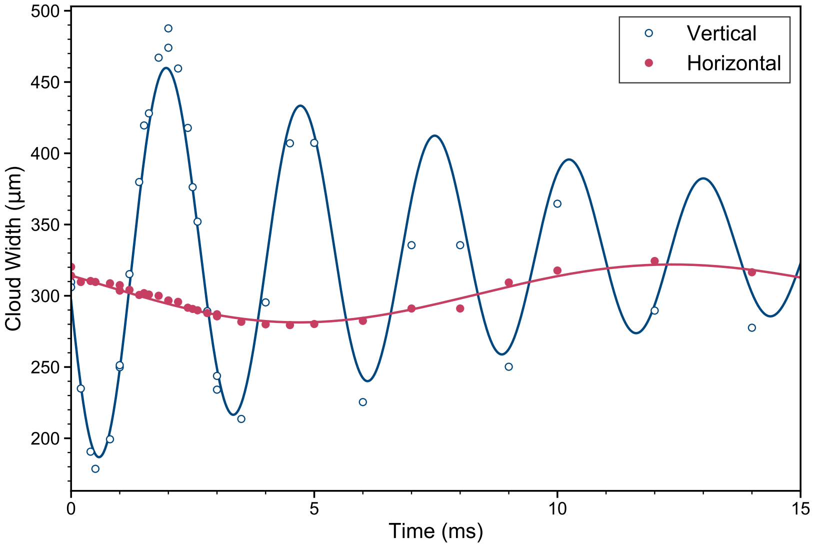

Figure 3.5: Measurement of trap frequency experienced by ^{87}Rb atoms in the crossed optical dipole trap. The $\lambda = 1550$ nm trapping light has a total power of ~ 5.4 W. Open and filled circles show measurements of the vertical and horizontal widths of the atomic cloud, while the lines show damped sine curves fitted to the results. In this case the radial and axial trap frequencies are $\omega_{\mathrm{r}}/(2\pi) = 181(2)$ Hz and $\omega_{\mathrm{a}}/(2\pi) = 33(1)$ Hz respectively.

than was measured for the original trap geometry.

The waists where the two beams intersect are estimated from the trap frequency experienced by atoms in the trap. To measure the trap frequency, the trapping beams are switched off with the atoms magnetically levitated for ~ 1 ms, during which the cloud expands. The atoms are then recaptured in the optical trap for a variable hold time before once again releasing the atoms for a 20 ms time of flight and absorption imaging. During the variable hold time, the cloud width oscillates at twice the frequency of the trap as shown in Fig. 3.5. We repeat this measurement in both single beam traps to determine waists of 105(2) µm and 95(2) µm for each beam. The measurement is then repeated in the crossed beam trap to ensure that the beams are well overlapped at the position of the atoms/molecules. These measurements are in agreement with direct knife edge measurements of the beams close to the centre of the trap.

In future iterations of our experiment, we plan to trap molecules using light at 1064 nm as this is a convenient wavelength for high power narrow linewidth lasers, and because at this wavelength the Feshbach and ground molecule states have the same polarisability. Preliminary tests using light at this wavelength have been performed in our experiment using a Nd:YAG non-planar ring oscillator (Innolight Mephisto). This laser can produce up to 2 W of 1064 nm light in continuous operation and has a very narrow free-running linewidth of ∼ 1 kHz. We servo the intensity of the light using an AOM before coupling the light into a standard single-mode ThorLabs optical fibre. The output of this fibre is then monitored through the leaked light of a mirror and actively stabilised by varying the RF power to the AOM via a feedback loop. The light then passes through the glass cell as shown in Fig. 3.3. The waist at the centre of the glass cell is ∼ 60 µm. This arrangement has also been used to form a bow-tie 3-D trap and 1-D lattice in which Feshbach molecules have been trapped [101]. Some light from the laser is sent to a Nufern fibre amplifier, which can be used to produce higher trapping powers at 1064 nm, however we intend to replace this in the near future with a Mephisto MOPA system.

3.2.3 STIRAP

A laser system for STIRAP must consist of two narrow-linewidth laser light sources which are labelled as the pump and Stokes as shown in Fig. 3.6. The frequency difference between these two sources is required to be relatively large (∼ 100 THz) and equal to the binding energy of the molecule. To ensure smooth running of the experiment, the frequency of both lasers must have excellent short and long term stability. In addition, the frequency of each laser must be continuously tunable over a wide frequency range in order to find and perform spectroscopy on the multitude of available molecular states.

The narrow-linewidths necessary for STIRAP can be achieved by stabilising the laser frequencies to an optical frequency comb [26], multiple independent cavities [152], or a single multi-wavelength cavity [153]. In the case of frequency stabilisation to an optical cavity, there are two approaches. The length of the cavity may be actively stabilised by referencing back to a frequency comb [152], or an atomic reference [154, 155]. Alternatively, the necessity of having an optical reference can be removed by relying on the

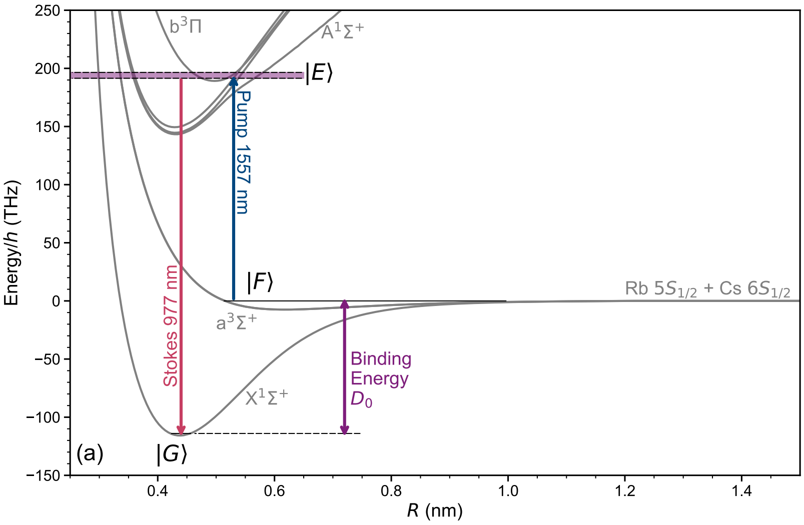

Figure 3.6: Molecular transitions for STIRAP. The coupling between states introduced by the STIRAP lasers is shown. The shaded purple area shows the region in which excited states may lie and still be accessible to our laser system for coupling to both states near dissociation and the rovibronic ground state.

passive stability of an ultra-low-expansion (ULE) glass cavity maintained at the zero expansion temperature of the glass [153]. Typically, a tunable frequency source is then generated by using the output of another laser which is offset-locked to the frequency stabilised laser via an optical phase-locked loop [153]. The laser system developed in our experiment is fundamentally different to those typically used in similar experiments as we only require two lasers.

Our system utilises a pair of Toptica DL Pro external cavity diode lasers to provide light at 1557 nm and 977 nm for the pump and Stokes transitions respectively. Light from each laser is passed through an optical isolator (∼ 40 dB) before being split on polarising beam splitters and coupled into four separate fibres leading to the main experiment, an optical frequency comb, a wavemeter and an optical cavity as shown in Fig. 3.7(a).

Both lasers are referenced to the same 10 cm plane-concave optical cavity to narrow the linewidth. The cavity (ATFilms) is constructed from ULE glass, and is mounted in a temperature stabilised vacuum housing from Stable Laser Systems. The temperature of the cavity is maintained at 35°C, the zero-expansion temperature of the ULE glass. Each beam sent to the cavity

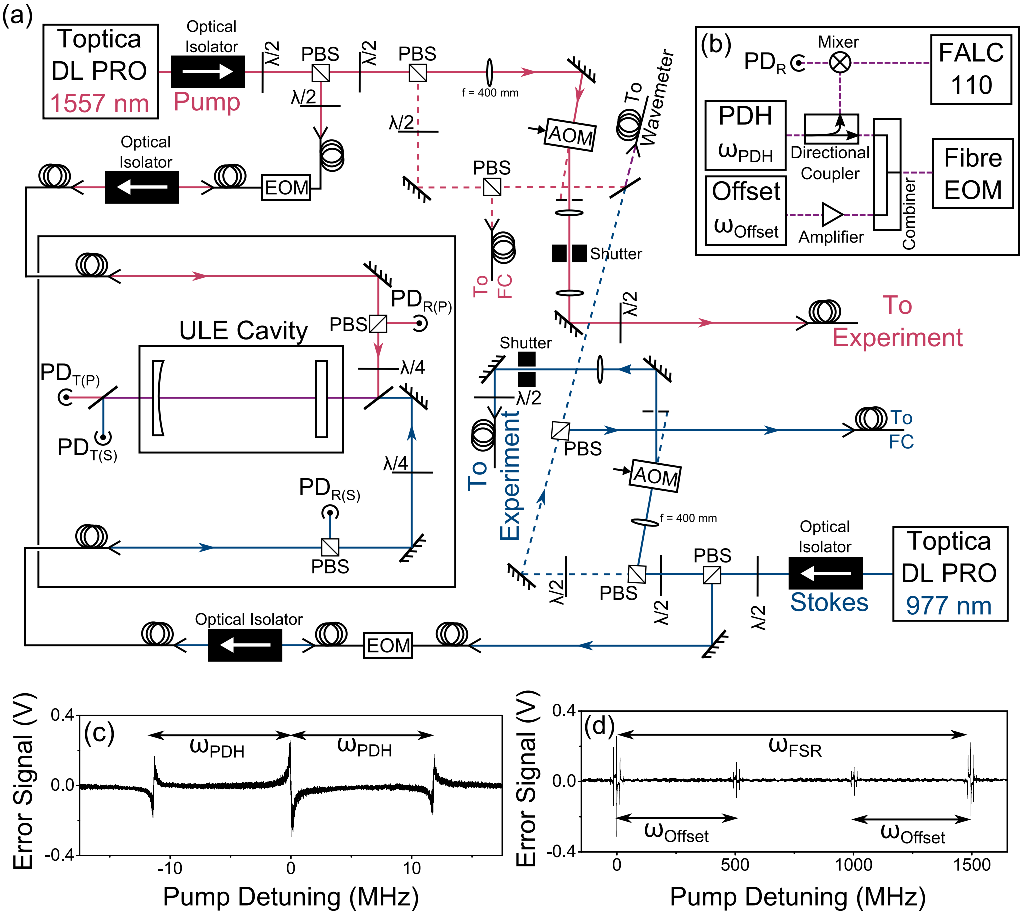

Figure 3.7: STIRAP laser system. (a) Optical setup for the laser locking and distribution of laser light to the experiment. Laser light is supplied by two Toptica DL Pros at 1557 nm for the pump (top left) and 977 nm for the Stokes (bottom right). The light is then split between the main experiment, an optical frequency comb (FC), a wavemeter, and the ULE optical cavity for frequency stabilisation. Fibre coupled EOMs between each laser and the optical reference cavity provide the Pound-Drever-Hall (PDH) and offset modulation signals required for frequency stabilisation as described in the main text. (b) The Pound-Drever-Hall and offset electronics. The directional coupler which is used to split the PDH modulation signal is a Minicircuits ZDC-20-3, and the mixer is a Minicircuits ZFM-150+. The resultant error signal is sent to a Toptica FALC 110 fast analogue servo module. (c) Example PDH error signal while scanning the pump laser over a small frequency range. (d) Example PDH error signal while scanning the pump laser over a large frequency range. The free spectral range of the cavity is $\omega_{\text{FSR}} = 1496.873(1)$ MHz at 1557 nm and $\omega_{\text{FSR}} = 1496.662(1)$ MHz at 977 nm.

passes through an optical fibre-coupled electro-optic modulator (EOM). The output of each EOM (Thorlabs LN65S-FC for 1557 nm, EOSpace PM-0K5-10-PFA-PFA-980 for 977 nm) is then coupled via a fibre and mode-matching optics to the optical cavity. Dichroic mirrors at either end of the cavity are used to combine the two different wavelengths of light entering the cavity, and to separate the two wavelengths following transmission or reflection. Both the transmitted and reflected beams are monitored on photodiodes, and the signal generated by the reflected light is sent to the locking electronics (Fig. 3.7(b)). The frequency stabilisation electronics are a standard Pound-Drever-Hall (PDH) setup as has been explained in [156], where the EOM is driven at a frequency $\omega_{\mathrm{PDH}} \sim 10$ MHz to generate the PDH readout signal (Fig. 3.7(c)). Each laser control unit is fitted with a fast analogue servo module (Toptica FALC 110) to which the error signal is sent.

The fibre-coupled EOMs are crucial to the simplicity and flexibility of our setup. These modulators are non-resonant and hence work over a wide bandwidth of 10 GHz. Additionally, these devices can be driven simultaneously at multiple frequencies and require relatively small driving voltages (~ 4.5 V). In addition to providing the modulation for the PDH lock, we use these EOMs to provide continuous tunability of the laser frequency sent to the main experiment. By applying a second modulation frequency ω_{Offset} to each EOM, we add high-frequency sidebands to the original carrier light (Fig. 3.7). By stabilizing the frequency of a sideband to a cavity mode, we are then able to precisely tune the frequency of the carrier light by simply changing the modulation frequency, ω_{Offset} [157]. Due to the high bandwidth of the EOMs, ω_{Offset} may be larger than the free spectral range of the optical cavity ω_{FSR}. Hence, the frequency of the carrier light can be tuned continuously to any point between the modes of the cavity.

Isolating the optical reference cavity from vibrations is typically critical for achieving high efficiency STIRAP. Our cavity is placed on a breadboard on top of a sorbathane mat, which is inside a wooden box lined with sound-proofing foam (30 mm thick). The whole assembly is placed on an optical table (without a vibration isolation platform) in the same room as the main experiment itself. We neglect further isolation in part because we find that the part of the apparatus most sensitive to vibrations is not the cavity itself

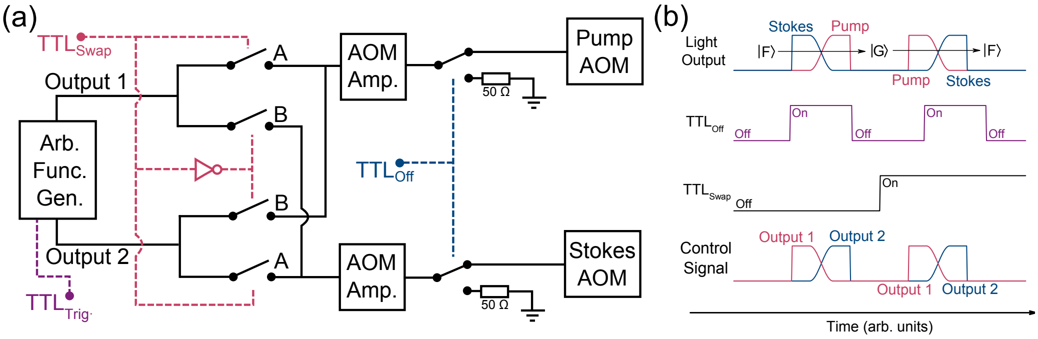

Figure 3.8: STIRAP pulse sequence control scheme. (a) STIRAP and spectroscopy pulses are controlled by two signals produced by a single arbitrary function generator (Agilent 33522B) which is triggered by a TTL pulse $\mathrm{TTL}_{\mathrm{Trig.}}$ from the FPGA. The outputs of the function generator are connected to the modulation input of two independent fixed frequency 80 MHz amplifiers via an array of TTL-controlled analogue switches (DG412). The switch array allows either output of the function generator to be connected to either amplifier. In the schematic shown, when $\mathrm{TTL}_{\mathrm{Swap}}$ is on, switches labelled A are closed and B are open. Output 1 of the function generator is therefore connected to the amplifier which controls the pump acousto-optic modulator (AOM) and output 2 controls the Stokes. Similarly, when $\mathrm{TTL}_{\mathrm{Swap}}$ is off, output 1 controls the Stokes and output 2 controls the pump. This allows a single pulse sequence to transfer molecules to and from the ground state as shown in (b). A third TTL control $\mathrm{TTL}_{\mathrm{Off}}$ disconnects the amplifiers from their respective AOMs to ensure no resonant light can reach the experiment when the STIRAP light is not in use.

but instead the EOM and the accompanying fibres.

Light destined for the main experiment is passed through an acousto-optic modulator (AOM) prior to fibre coupling (ISOMET 1205C-1023 for 1557 nm, ISOMET 1205C-1 for 977 nm); this shifts the frequency of the light by 80 MHz and allows control of the amplitude of the light to create the STIRAP pulses. The pulse sequence for STIRAP is generated by an arbitrary function generator (Agilent 33522B). The output from this is sent to a fast (∼ns) TTL-controlled analogue switch (DG412) which allows the pump and Stokes control signals to be swapped. This enables the same pulse sequence from the signal generator to be used to transfer the molecules to and from the ground state. The output of the switch then controls the amplitude output of the fixed frequency amplifier (ISOMET 532B-2) driving the AOM, and hence the intensity of the light at the experiment. Between the amplifier and the AOM there is another switch (Minicircuits ZX80-DR230-S+) which disconnects the output of the amplifier from the AOM. This is used to ensure that there is no leaked resonant light reaching the molecules when not required. The control scheme used is shown in Fig. 3.8.

At the main experiment, the light from each fibre is coupled in free space on a dichroic mirror and focussed (f = 300 mm) to a waist of 37.7(1) µm (pump) and 35.6(6) µm (Stokes) at the position of the trapped molecules (Fig. 3.3). The system can provide up to 16 mW of each wavelength of light at the position of the molecular sample.

3.3 Magnetic Fields

Homogeneous magnetic bias fields and magnetic field gradients are generated using various pairs of copper coils outside the glass cell. These copper coils are wound from square cross-section copper tubing and are water cooled using a barrier cooler filled with distilled water. Two sets of coils in anti-Helmholtz configurations produce magnetic field gradients for the magnetic trap (quad 1) and science MOT (quad 2). The magnetic trap gradient is roughly an order of magnitude greater than the MOT gradient for a given current. There are three sets of bias field coils each in a Helmholtz configuration. Bias 1 and 2 are capable of producing the largest magnetic fields. At present, only bias 1 is used to reach the $\sim$ 200 G magnetic field required in our molecule production sequence. However, both of these coils may be connected in series to produce a magnetic field of up to 1157(1) G using a current of 425 A [98]. Bias 3 is used to make small fast ($\sim$ 1 ms) changes to the bias field as each coil consists of just two turns of wire. In the current experimental sequence, bias 1 is switched on to produce a fixed magnetic field just below the Feshbach resonance while bias 3 is used to precisely tune the magnetic field over the resonance to associate atoms into molecules.

3.3.1 Magnetic Field Calibration

To calibrate the magnetic field we measure the microwave transition frequency between the spin-stretched states of atomic Cs ($|f = 3, m_f = +3\rangle \rightarrow |4, +4\rangle$) or Rb ($|1, +1\rangle \rightarrow |2, +2\rangle$). The energy difference ΔE between these

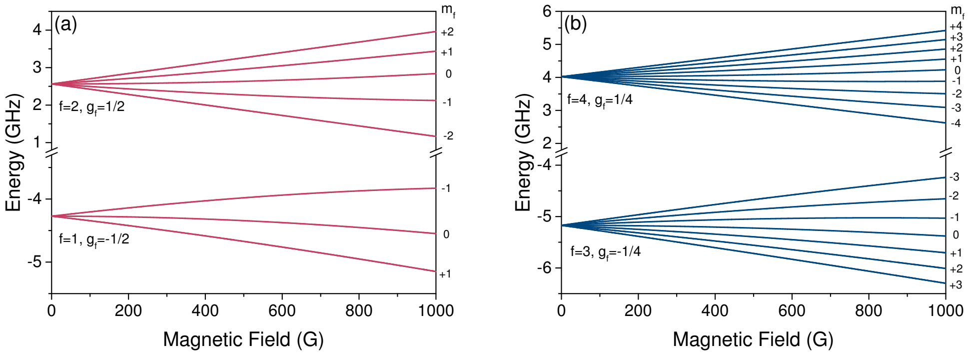

Figure 3.9: Breit-Rabi diagrams showing the magnetic field dependent energy shifts of the hyperfine ground states in (a) ^{87}Rb and (b) ^{133}Cs.

states at a given magnetic field B can be calculated using the Breit-Rabi equation

$$\Delta E = \frac{hV_{\mathrm{hfs}}}{2(2I+1)} - g_I \mu_{\mathrm{B}} B m_f \pm \frac{1}{2} hV_{\mathrm{hfs}} (1 + \frac{4m_f}{2I+1} x + x^2)^{1/2}, \tag{3.1a}$$

$$\text{where } x = \frac{(g_I + g_J)\mu_{\mathrm{B}} B}{hV_{\mathrm{hfs}}}. \tag{3.1b}$$

Here, I is the nuclear spin, V_{hfs} is the hyperfine splittings of the ground states at zero magnetic field, $g_{(f,I,J)}$ is the Landé g-factor, h is the Planck constant, and μ_{B} is the Bohr magneton [158]. The relevant Breit-Rabi diagrams for Rb and Cs can be seen in Fig.3.9. By measuring the transition frequency between these states experimentally, we can therefore calculate the magnetic field experienced by the atoms.

Considering specifically Cs, the atoms are initially trapped in the $|3, +3\rangle$ state and the transition frequency between the spin-stretched states is in the microwave regime ($\sim$ 9.6 GHz for Cs). The atoms are exposed to microwave radiation (see Sec. 3.5) for $\sim$ 100 ms and some of the population is transferred into the $|4, +4\rangle$ state only when the microwave frequency is resonant with the transition. To perform a measurement we need to separate the atomic populations in each of the two states from each other. The $|3, +3\rangle$ state has a negative magnetic dipole moment while the $|4, +4\rangle$ state has a positive magnetic dipole moment, the two states can therefore be separated via the Stern-Gerlach effect (2.2.1). By applying a magnetic field gradient to levitate the $|3, +3\rangle$ atoms, these atoms will be separated vertically from those transferred into the $|4, +4\rangle$ state which experience a downward force in

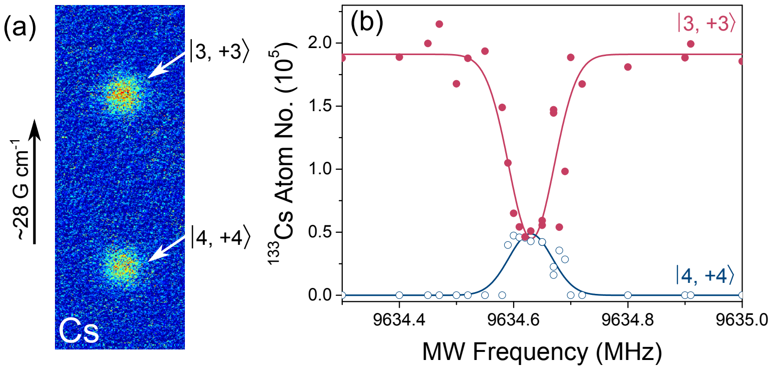

Figure 3.10: Magnetic field calibration using the spin-stretched hyperfine states in atomic ^{133}Cs. (a) Absorption images of Cs after Stern-Gerlach separation of the $|f = 3, m_f = +3\rangle$ and $|f = 4, m_f = +4\rangle$ hyperfine states as discussed in the main text. (b) Experimental results showing the microwave (MW) frequency dependence on the ^{133}Cs atom population in each hyperfine state. The centre frequency of the transition here is 9634.630(3) MHz which corresponds to a magnetic field of 179.124(1) G.

the same magnetic field gradient. The microwave frequency is resonant with the transition when the largest proportion of the atomic population has been transferred into the $|4, +4\rangle$ state. An example experimental measurement is shown in Fig. 3.10.

3.4 Electric Fields

The application of an external electric field serves to mix states with opposite parity which allows the observation of the molecular dipole moment in the laboratory frame of reference. Until recently, our apparatus had been used only for preparing the high phase-space density atomic mixtures and therefore no electric fields had been required. The initial design criteria was to be able to produce electric fields up to $\sim$ 1.5 kV cm^{-1} using a set of electrodes outside of the fused silica vacuum cell with minimal modifications to the existing apparatus. This electric field would give access to a lab-frame dipole moment of $\sim$ 0.6 D. In addition, the electric field must be quite uniform at the position of the molecules in order to minimise the variation in dipole moment across the molecular sample.

The final design utilises a set of four wire electrodes positioned parallel to the

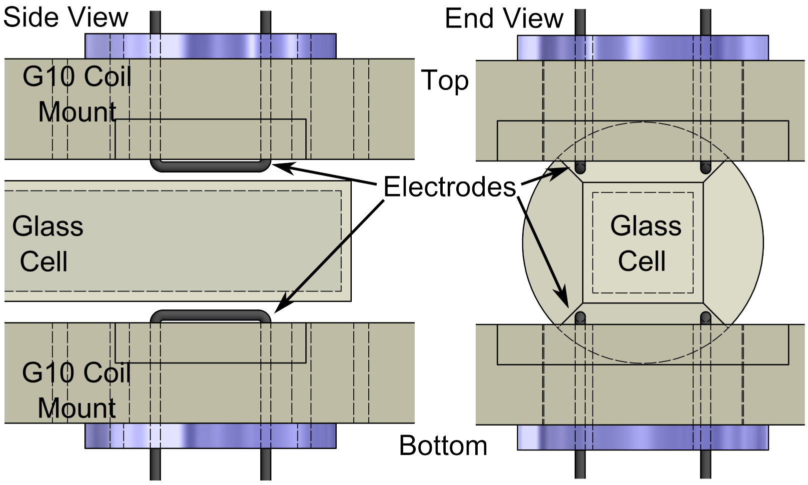

Figure 3.11: Electrode array for producing DC electric fields. A set of four electrodes are mounted in Tufnol G10 around the centre of the magnetic field coil array. Each electrode can be connected to one of two power supplies capable of producing potentials of up to ±5 kV. In its current configuration, the top electrodes are connected to a negative potential and the bottom electrodes are connected to a positive potential. This gives a DC electric field anti-parallel to the applied magnetic field.

four corner edges of the fused silica cell. This is a relatively straightforward way of generating an electric field inside the cell without impeding any optical access. In addition, by wiring different pairs of electrodes, the electric field direction can be chosen to either be parallel or perpendicular to the magnetic bias field. The disadvantage of this setup is that the electric field produced is only uniform close to the centre of the electrode array. To ensure the molecules are close to this position, the electrodes are mounted on the coil mounts used to produce the magnetic fields rather than with respect to the glass cell. The electrodes are made from 1.5 mm stainless steel wire and run through a pair of mounts made from Tufnol G10 as shown in Fig. 3.11. Each mount sits in a hole at the centre of the coil mount. These holes are also used for the vertical MOT and optical pumping beams which are unimpeded by the addition of the electrodes.

To calculate the electric field at the centre of our glass cell we cannot only consider the simple geometry of the four electrodes; we must also include the dielectric constant of the glass cell and the surrounding magnetic field coils. To achieve this, we begin by constructing a model of the experimental apparatus in Autodesk Inventor, a common computer-aided design (CAD)

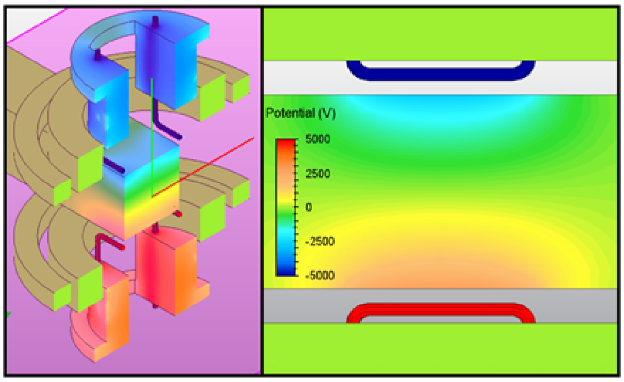

Figure 3.12: Simulating the electric potential across the cell. Calculation is performed using finite element methods in Autodesk Multiphysics. Here ±5 kV is applied to the electrodes positioned close to the corners of the fused silica cell to give an electric field at the centre of the cell of 1.5 kV cm^{-1}.

program. We then use a second program, Autodesk Multiphysics [1] to create a 3D mesh which follows the geometry of the experimental apparatus. We use finite element methods [159] to calculate the potential at all nodes on this mesh taking into account the potential applied to the electrodes and coils and dielectric properties of the glass cell (see Fig. 3.12). Applying an electric potential of ±1 kV between the upper and lower electrode pairs yields an electric field at the position of the molecules of 153(1) V cm^{-1}. A total potential difference between the electrodes of $\sim$ 10 kV is therefore required to achieve the desired maximum electric field of 1.5 kV cm^{-1}.

The uncertainty on the electric field has three contributions. The largest contribution is due to the uncertainty in the measurement of the electrode separations, including any uncertainties in the electrode shape (i.e. the bend radius at either end of the electrode). This is currently the largest source of uncertainty in our calculation. The next source of error is caused by the uncertainty in the position of the molecules with respect to the centre of the electrode array. This uncertainty is estimated to be ±1 mm in any direction, and the uncertainty in the field therefore also gives an indication of the uniformity of the field. Note that the position of the glass cell with respect to the electrode array has an error of similar magnitude. However, calculations of the electric field where we move the glass cell by ±1 mm show

---

[1] The Autodesk Multiphysics package has subsequently been merged into Autodesk Simulation Mechanical

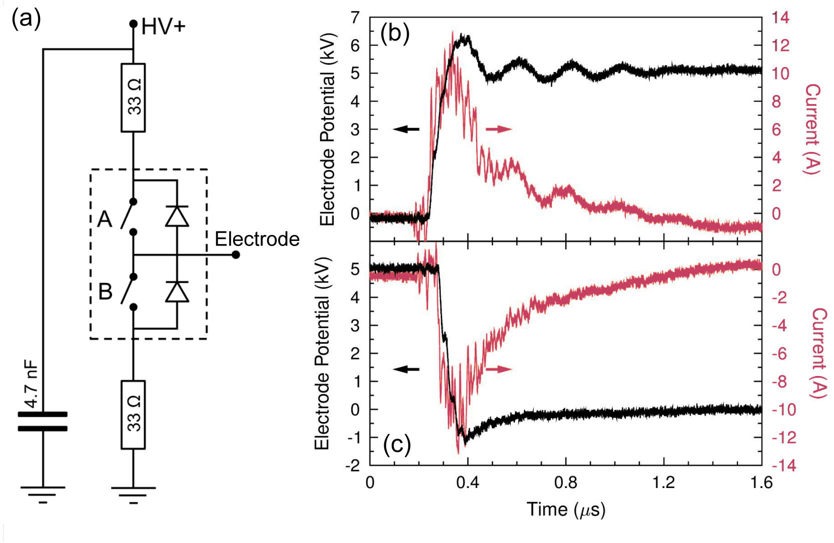

Figure 3.13: Switching of high voltages. (a) Circuit diagram for the switches used. Everything contained within the dotted box is contained within the moulded plastic housing of the switch itself, while the rest is mounted on an external PCB. When charging the electrodes, switch A is closed and B is open, when discharging switch B is closed and A is open. Example (b) rise and (c) fall times for the high voltage switches are also shown. Both switches were activated/deactivated simultaneously, though only the positive potential pulses are shown here. The potential on the electrodes and current in/out of the electrodes are shown in black and red respectively. The time $t = 0$ is defined as the time where the TTL control signal reached 2.5 V.

negligible deviation from the central value. The final source of error is from the electric field calculation itself. Finite element analysis is an approximate method which relies upon a converging solution. The convergence has some noise, which is estimated by repeating the calculation with a range of mesh densities.

In our experiment we need to be able to switch on the electric field for time scales similar to that used for the STIRAP pulse sequence (microseconds) and to the expected lifetime of the molecules in the trap (seconds). We therefore require fast switching times to enable the fast pulsing on of the electric field and for the potential to be relatively stable over many seconds while active.

The high potentials required are generated using two Stanford Research Systems PS350 5kV power supplies. This allows us to apply potentials of ±5 kV to the electrodes; in theory allowing access to the 10 kV potential difference required to reach our maximum field goal. The power supplies have a very large capacitance, and are hence very slow to switch on and off (the discharge time can be measured in seconds). In order to speed up the switching times we employ two Behlke HTS-61-03-GSM switches in conjunction with a parallel capacitor. See Fig. 3.13(a). These switches allow the slow power supplies to store charge in the capacitor; the switches then allow the transfer of that stored charge to the electrodes, and away from the electrodes much more quickly than using the power supplies alone. The switches are controlled via TTL, and the connection for this is made via an external optical link to minimise the risk of damage to the FPGA used to control the experiment. The size of the charging capacitor required, and the final switching time depend enormously on the capacitance of the electrode configuration. Consequently, it is important to keep the high voltage wires separate and as short as possible to minimise extra resistance and capacitance being introduced by these components. The switching times in our experiment have been measured using a Testec HVP-15HF 50 MHz high voltage probe with a 4.7 nF capacitor used in the switching circuit. Example input/output signals can be seen in Fig. 3.13. Some ringing can be seen on the activation pulse which limits the switching time to around 1 µs. This is due to the inductive nature of the system we have. Moreover, it is very difficult to damp without further increasing the switching time. The deactivation switch time is much faster and takes 300 ns. The peak current measured in each direction is 13 A. Note that it is very difficult to get an accurate measurement of the minimum switching time. This is because the addition of a probe necessarily increases the capacitance of the electrode array which therefore increases the switching time!

The maximum electric field attainable in our experiment is not limited by the maximum potential we can apply to the electrodes. It is instead limited by the electric field at which the fused silica cell becomes measurably polarised (~ 1 kV cm^{-1}). Above this electric field, charge build up on the surface of the cell leads to a significant electric field even when there is no potential applied to the electrodes. This electric field causes a DC Stark shift of the ground state which shifts the state off-resonance with our STIRAP lasers, making return of the molecules to the free-atomic state for imaging difficult.

We have found that with UV light we can remove this stray charge between experimental runs, but we have not tried to apply the UV light during the experimental sequence. Future iterations of the experiment will seek to minimise this effect by placing electrodes in vacuum so as to minimise the electric field at the walls of the glass cell. Another option may be to use ITO coatings on the walls of the glass cell. It has been shown that an array of 8 electrodes may be used to generate extremely uniform fields with a fractional deviation in electric field across the sample of trapped molecules of $\sim 10^{-6}$ [160].

3.5 Microwave Sources

As discussed in section 3.3.1, microwaves at $\sim$ 6.8 GHz and $\sim$ 9.6 GHz are used in the experiment to transfer atoms between hyperfine levels in the atomic ground states as a means of calibrating the magnetic fields. At these frequencies, we use two microwave horns (Atlantec RF AS6366 and AS6186) positioned just outside the coil array which serve as a directional source of unpolarised microwaves. However, the transitions between the lowest-energy rotational states of the molecule require lower frequency microwaves than can be provided by these two antennas.

The rotational constant of ^{87}Rb^{133}Cs is around $B_v \approx 490$ MHz. Therefore, the splitting between the ground and first rotationally excited state is therefore $B_v N(N+1) = 2B_v \approx 980$ MHz. This is a microwave frequency (MW) in the ultra-high frequency (UHF) part of the radio spectrum which is used for military and aeronautical communication and radio-navigation, and is close in frequency to those used in cellular communication [161]. Directional antennas (e.g. horns) must typically have dimensions on the order of one wavelength λ. As the wavelength in this part of the spectrum is relatively large ($\lambda \approx 30$ cm), directional sources placed close to the molecules would be impractical and we must therefore consider omnidirectional antennas which can be constructed with a less-intrusive form factor.

Our solution was to install a pair of homebuilt base-fed $\lambda/4$ monopole antennas in the apparatus to work around 980 MHz. A schematic diagram of one of our antennas is shown in Fig. 3.14. The antenna consists of a square of

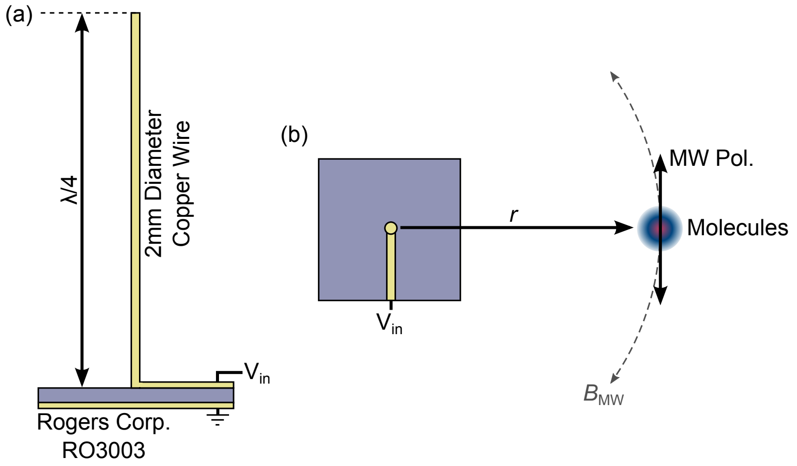

Figure 3.14: 980 MHz $\lambda/4$ monopole antenna design. (a) Side view showing both sides of the high frequency circuit board and length of copper wire used to match the resonant frequency. (b) End view looking down the length of copper wire. The oscillating magnetic field produced around the wire is cylindrically symmetric around the length of wire and the molecules are positioned some distance from the antenna r. The microwave polarisation is therefore linear and perpendicular to both the vector r and the axis of the copper wire.

high frequency circuit material with a layer of rolled copper on each surface (Rogers Corp. RO3003). One of the copper faces is milled to leave a narrow copper track leading from the edge to the centre of the board. The centre end is soldered to a straight piece of copper wire angled perpendicular to the plane of the circuit board. The copper wire has length equal to a quarter wavelength ($\lambda/4 = 77$ mm). A female SMA connector is attached to the edge of the circuit board. The pin of the SMA is connected to the milled narrow wire, while the ground is connected to the opposing square copper surface which acts as a ground plate[2]. The idealised monopole antenna can be considered as a dipole whose lower half has been cut off and replaced by its image in the ground plane. However, as the ‘grounded’ monopole antenna only radiates its power in a hemisphere above the ground plane, the intensity output is 3 dB greater than that of a free-space dipole antenna [162, 163]. The polarisation of the microwaves (defined as the plane of the magnetic field component) is reasonably linear and is perpendicular to the axis of the antenna at the position of the molecules as shown in Fig. 3.14. As a re-

---

[2] One of the antennas in our apparatus is mounted such that the ground plate is clamped close to and parallel to the surface of the earthed optical breadboard. In this case, the breadboard also acts as an extended ground plate.

sult, installing two antennas orientated perpendicular to each other and with appropriate orientation with respect to the magnetic field, allows one to preferentially drive π transitions (MW polarisation parallel to B-field) and the other to drive $\sigma^{\pm}$ transitions (MW polarisation perpendicular to B-field).

Microwaves are provided by two analog signal generators (Agilent N5183B and E8257D) which are both frequency referenced to the same external 10 MHz GPS disciplined oscillator (Jackson Labs Fury). Each signal generator is connected to a Minicircuits TVA-R5-13 +38 dB amplifier, which is in turn connected directly to the antenna. The signal may be pulsed on and off using an external TTL-controlled switch (Minicircuits ZYSW-2-50DR) placed between the source and the amplifier. These switches have a typical rise/fall time of 6 ns, though our minimum pulse time is limited to 730 ns by the minimum allowed step duration in the field programmable gate array (FPGA) which controls the timing of the experiment. Alternatively, the Agilent N5183B has built-in pulse modulation enabling pulse times down to as low as 20 ns.

Transitions to higher rotational levels require higher frequency microwaves. Our existing array of horns covers a frequency range of ∼2-13 GHz. Therefore, with the addition of the 980 MHz antennas, we can access any rotational states starting from the rotational ground state up to around $N = 13$ ($E_{N=13} - E_{N=12} \approx 12.7$ GHz). However, as the horns offer no control of the polarisation of the microwaves, it may prove useful to develop alternative broadband antenna solutions to enable more selective transfer between certain molecular hyperfine states. Linear antennas, as we are using at 980 MHz, offer linear polarisations of microwaves, but it is also possible to generate circular microwave polarisations to enable selectivity between σ^{+} and σ^{-} states. One such antenna design is the spiral antenna [164, 165], which is frequency independent [166] and widely used commercially in GPS applications.

Chapter 4

Creation and Characterisation of Ultracold ^{87}Rb^{133}Cs

The production of molecules at ultracold temperatures is a difficult goal to accomplish. Although direct cooling techniques are making great progress [39, 42, 45], to date the most successful approach is to employ magnetoassociation on a Feshbach resonance to produce weakly-bound molecules from a pre-cooled atomic gas. These molecules can then be transferred to their rovibronic and hyperfine ground state by stimulated Raman adiabatic passage (STIRAP). This process has been used to produce homonuclear molecules such as $\mathrm{Cs_2}$ [152] and $\mathrm{Rb_2}$ [67] and, most relevant to this work, a small but growing number of heteronuclear molecules possessing permanent electric dipole moments [26, 28–30, 32].

In this chapter, we will demonstrate the production of ^{87}Rb^{133}Cs molecules in the lowest hyperfine level of the rovibronic ground state. Production of weakly-bound Feshbach molecules in our apparatus was first reported in [167], with transfer the the rovibronic ground state in [29]. Each of these steps has been the primary subject of previous theses [100, 101], and we will therefore only briefly outline the necessary steps and key results (4.1, 4.2). In this work, we will pay special attention to optimising the efficiency of both processes to maximise the number of molecules produced. This is vital to maximise the initial density of the molecule sample, and to enable measurements of the molecule lifetime with an acceptable signal to noise. In

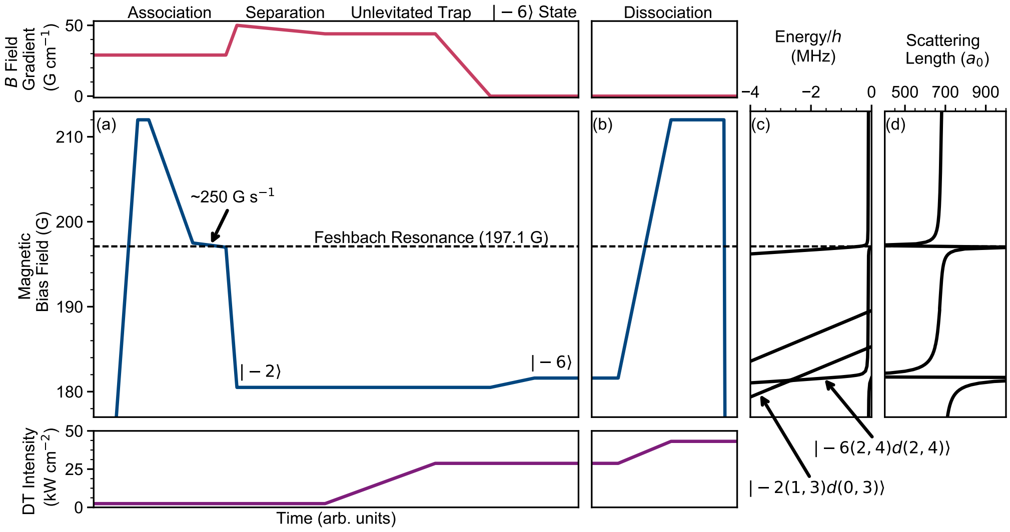

Figure 4.1: Experimental sequence for the (a) association and (b) dissociation of weakly-bound Feshbach molecules. We begin with a mixture of ^{87}Rb and ^{133}Cs atoms at a temperature of $\sim$ 300 nK in a magnetically-levitated optical dipole trap at a magnetic bias field of $\sim$ 22 G. To associate molecules, we sweep the magnetic field from high to low magnetic field across a Feshbach resonance at 197.1 G. We separate the atoms and the molecules via the Stern-Gerlach effect before transferring the molecules to an unlevitated optical trap. The molecules are then prepared in the $|{-6}(2,4)d(2,4)\rangle$ Feshbach state ready for transfer to the rovibronic ground state by STIRAP. To dissociate the molecules, the magnetic bias field is swept back across the Feshbach resonance and held where the energy of the molecular state is higher than the energy of the free atoms. Once all of the molecules have been dissociated back to atoms, the magnetic field must be switched off for absorption imaging. (c) Near-threshold molecular bound states for ^{87}Rb^{133}Cs in the magnetic field regime close to the association Feshbach resonance. (d) Scattering length between ^{87}Rb^{133}Cs showing the Feshbach resonances used in this work.

addition, we will discuss the process of imaging atoms and molecules in our experiment (4.3). Finally, we present a number of characterisation measurements of the molecule's temperature (4.4), binding energy (4.5), and electric dipole moment (4.6).

4.1 Feshbach Association

We begin the association process with a mixture of ^{87}Rb and ^{133}Cs at a temperature of $\sim$ 300 nK and a phase-space density of $\sim$ 0.1. The atomic mixture is held in a magnetically-levitated optical dipole trap following a

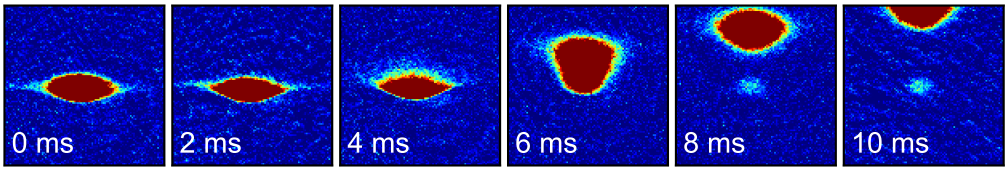

Figure 4.2: Spatial separation of atoms and molecules via the Stern-Gerlach effect. Cs absorption images after various hold times in a magnetic field gradient. The magnetic field gradient is chosen to over-levitate the atoms such that they are thrown out of the top of the dipole trap.

sequence of evaporative cooling, where the intensity of the dipole trapping light is reduced over $\sim$ 800 ms to allow the most energetic atoms to escape from the sample. A magnetic bias field of $\sim$ 22 G is applied which is required for the efficient evaporative cooling of ^{133}Cs. We tune the ratio of ^{87}Rb and ^{133}Cs atoms in the trap to optimise the efficiency of magnetoassociation by varying the number of ^{133}Cs atoms loaded into the MOT at the start of the experimental sequence. We typically find that the largest number of Feshbach molecules are produced with 3.5×10^5 ^{133}Cs atoms and at least 4×10^5 ^{87}Rb atoms.

To associate molecules from the atomic mixture we must increase the magnetic bias field to near the Feshbach resonance at 197.1 G as shown in Fig. 4.1. We begin by increasing the bias field to 212 G, where the field is allowed to stabilise, before reducing the magnetic field to within $\sim$ 0.4 G of the resonance. We perform association by sweeping the magnetic bias field over the Feshbach resonance from high to low field with a ramp speed of $\sim$ 250 G s^{-1} over 1.56 ms. Once across the resonance, molecules occupy a bound state which runs nearly-parallel to the free-atomic energy. We therefore ramp the magnetic field down further to a second Feshbach resonance around $\sim$ 182 G. The speed of this ramp is carefully designed to follow the avoided crossings between the Feshbach states and allows us to transfer the molecules to the $|-2(1,3)d(0,3)\rangle$ Feshbach state. The molecules created have a temperature similar to that of the atomic distribution from which they are associated.

The $|-2(1,3)d(0,3)\rangle$ state has a different ratio of magnetic moment to mass than either of the free atom species[1]. This allows the separation of the

---

[1] The $|-6(2,4)d(2,4\rangle$ Feshbach state which the molecules pass through could also be

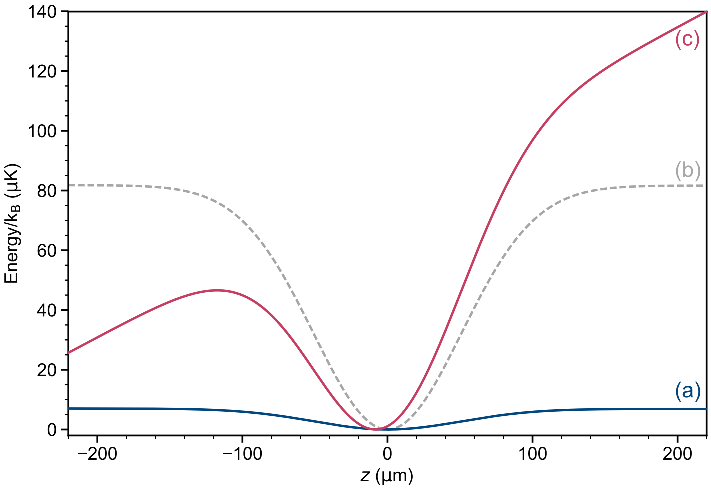

Figure 4.3: Transfer of Feshbach molecules from the shallow magnetically levitated trap to an unlevitated pure optical trap. (a) The molecules begin in a shallow optical trap which is supported against gravity by the interaction between the molecules magnetic dipole moment and an applied 43 G cm^{-1} magnetic field gradient. (b) The trap is made deeper by increasing the intensity of the trapping beams by a factor of $\sim$ 10 over 20 ms. (c) The magnetic field gradient is ramped off over 10 ms leaving the molecules trapped in a purely optical trap. The trap centre shifts over this time by ∼10 µm due to gravitational sag.

atoms from the molecules via the Stern-Gerlach effect. Both atomic species are exactly levitated using a magnetic field gradient of 29 G cm^{-1}, while molecules in the $|-2(1,3)d(0,3)\rangle$ state require a gradient of 43 G cm^{-1}. If we apply a gradient to levitate the molecules, the trap for the atoms will therefore be tilted and they are lost from the trap as shown in Fig. 4.2. We find that the most robust method for removing all of the atoms requires an initial field gradient of 50 G cm^{-1}. In order to minimise loss of molecules during this step, we ramp the magnetic field gradient up to this value initially before relaxing the gradient back to exactly levitate the molecules over 15 ms.

Once only molecules remain in the trap, we must transfer the molecules to an unlevitated optical trap as the ground state has no appreciable magnetic dipole moment. The dipole trap intensity is increased from 3 kW cm^{-2} to

---

used for Stern-Gerlach separation. However, at present we are unable to magnetically levitate states with positive magnetic dipole moments such as this. In addition, we observe a factor $\sim$ 10 shorter lifetime in the $|-6(2,4)d(2,4)\rangle$ state which would likely make the overall molecule production process less efficient. This shorter lifetime is not a problem when used as the starting point for STIRAP transfer, as the molecules only occupy this state for 2 ms before they are transferred to the long-lived rovibronic ground state.

36 kW cm^{-2}, corresponding to an increase in trap depth from 7 µK to 82 µK over 20 ms. During this transfer, the radial (axial) trap frequency increases from 51 Hz (10 Hz) to 174 Hz (34 Hz) which causes heating of the molecules. However, as the heating is roughly adiabatic, the trap depth increases $\propto I$ while the temperature of the molecules increases proportional to the change in trap frequency $\omega_{\text{trap}} \propto \sqrt{I}$. The molecules are therefore heated significantly less than the depth increase of the trap. After the increase in intensity, the magnetic gradient is ramped off over 10 ms. This leaves the molecules in a trap tilted by gravity with a depth of 47 µK as shown in Fig. 4.3. Once in the unlevitated optical trap, the molecules are transferred to the $|-6(2,4)d(2,4)\rangle$ Feshbach state in preparation for STIRAP transfer to the rovibronic ground state. When well optimised, our apparatus can create up to 5000 Feshbach molecules at the end of this sequence. Typically the number is slightly lower due to slow drifts in magnetic fields and light power/polarisation out of the optical fibres. When optimised for stability, we routinely create 3000-4000 Feshbach molecules ($\sim 1\%$ conversion efficiency) for around 300 experimental cycles per day.

4.2 Transfer to the Ground State

The first step to performing STIRAP is to set both lasers on resonance with the necessary molecular transitions. To find the *pump* transition, we perform one-photon spectroscopy of the electronically excited b$^3\Pi$ + A$^1\Sigma^+$ hyperfine manifold. This is initially done in the dipole trap by pulsing 20 µW of pump light, polarised parallel to the magnetic field, on for 750 µs. The molecules, which are initially in the near-dissociation Feshbach state $|F\rangle$, are transferred to an excited state $|E\rangle$ when the pump is resonant with a transition. This is observed as a loss of molecules remaining in state $|F\rangle$. Using this method, we have observed seven excited states with the molecules starting in the $|-2(1,3)d(0,3)\rangle$ Feshbach state as reported in [130]. The $|^3\Pi_1, v = 29, N = 1\rangle$ excited state identified for use as the intermediate state for STIRAP is shown in Fig. 4.4 (b).

To find the Stokes transition, we perform two-photon spectroscopy. This involved pulsing 40 µW of pump and 16 mW of Stokes light simultaneously,

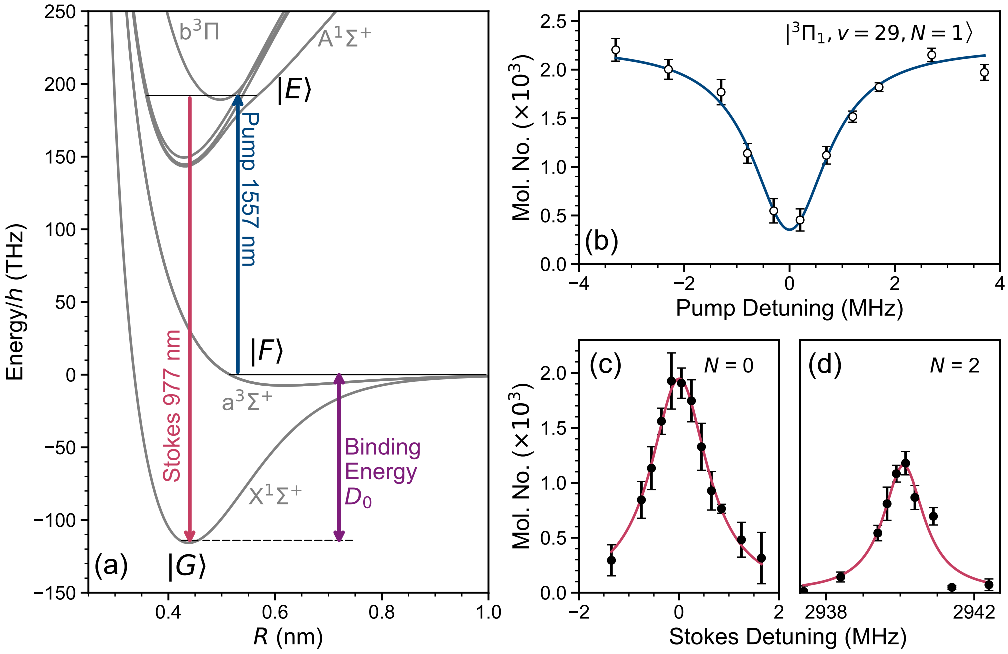

Figure 4.4: One- and two-photon spectroscopy of STIRAP transitions. (a) Molecular potentials for ^{87}Rb^{133}Cs. The pump and Stokes transitions couple the intial Feshbach triplet state $|F\rangle$ and rovibronic singlet ground state $|G\rangle$ to a common electronically excited state $|E\rangle$ with mixed singlet-triplet character. These two transitions differ in energy by the binding energy of the ground state of the molecule with respect to the intial Feshbach state. (b) One-photon spectroscopy of the $|^3\Pi_1, v = 29, N = 1\rangle$ excited state used as state $|E\rangle$ in this work. The pump light only is pulsed on for 750 µs and the transition is observed as loss of molecules from the initial Feshbach state $|F\rangle$. (c/d) Two-photon spectroscopy of (c) $N = 0$ and (d) $N = 2$. Both pump and Stokes light is pulsed on simultaneously. When the Stokes light is on resonance, the loss of molecules due to the pump light is suppressed.

again for 750 µs. The Stokes light is polarised perpendicular to the applied magnetic field, while the pump polarisation remains parallel as it is in the one-photon spectroscopy. When the Stokes is *off*-resonance, we observe no molecules as they are all transferred to the excited state $|E\rangle$. When the Stokes is *on*-resonance, the loss of molecules is suppressed due to the formation of a two-photon dark state. Features for when the Stokes laser is resonant with transitions to the rotational ground state $N = 0$ and the second rotationally excited state $N = 2$ are shown in Fig. 4.4 (c/d). Note that when using this technique we are unable to resolve any of the hyperfine structure in the deeply-bound rotational states.

To efficiently transfer molecules between the initial Feshbach state $|F\rangle$ and the rovibronic ground state $|G\rangle$, we must modulate the intensities of both the pump and Stokes light to form the required STIRAP sequence (see Fig. 4.5). We begin the transfer with the molecules starting in the $|-6(2,4)d(2,4)\rangle$ Feshbach state to maximise the strength of the coupling of the pump transition [29, 130]. Both lasers are set on-resonance with their respective transitions and the intensities varied sinusoidally between 0 and ~ 13 mW in each beam over 20 µs to perform the transfer. Details of imaging in the experiment will be discussed in section 4.3. In brief, imaging requires that the molecules be returned to the initial Feshbach state at the end of each experiment. This requires that we perform a 'double' STIRAP sequence as shown in Fig. 4.5.

Initial attempts to perform STIRAP were carried out in the $\lambda = 1550$ nm dipole trap and showed limited efficiency of 50% in each direction [29]. This low efficiency was caused by the polarisability difference between states $|F\rangle$ and $|G\rangle$ which led to a spatially varying AC Stark shift in the two-photon detuning across the molecules. To remove this effect, the dipole trap is switched off for ~100 µs during the STIRAP transfer after which the molecules are recaptured. During this time, the motion of the molecules is small and we observe no loss of molecules as a result of switching off the trap. The STIRAP transfer efficiency in free space is 92(1)% as shown in Fig. 4.5.

To optimise the efficiency, we perform the STIRAP pulse sequence and vary the detuning of the Stokes laser. The two photon resonance feature we observe by this method is significantly narrower than that from the two-photon spectroscopy, and this allows us to observe hyperfine structure. In Fig. 4.5(c) we show the result of varying the Stokes detuning for two different polarisations of the Stokes laser. The states $|F\rangle$ and $|E\rangle$ both have $M_F = 4$. When the Stokes laser is polarised parallel to the applied magnetic field, we therefore drive a π-transition to a ground hyperfine state with $M_F = 4$. Alternatively, when the Stokes laser is polarised perpendicular to the applied magnetic field, we drive $\sigma^{\pm}$ transitions to hyperfine states with $M_F = 3$ or 5. Sufficiently strong transitions to enable efficient transfer are only observed to two of the available hyperfine states. The energy difference between the two observed hyperfine states, along with the selection rules for the allowed transitions, allows these two states to be uniquely identified as the spin stretched $M_F = 5$ state, and the highest energy $M_F = 4$ state shown in Fig. 2.8. The

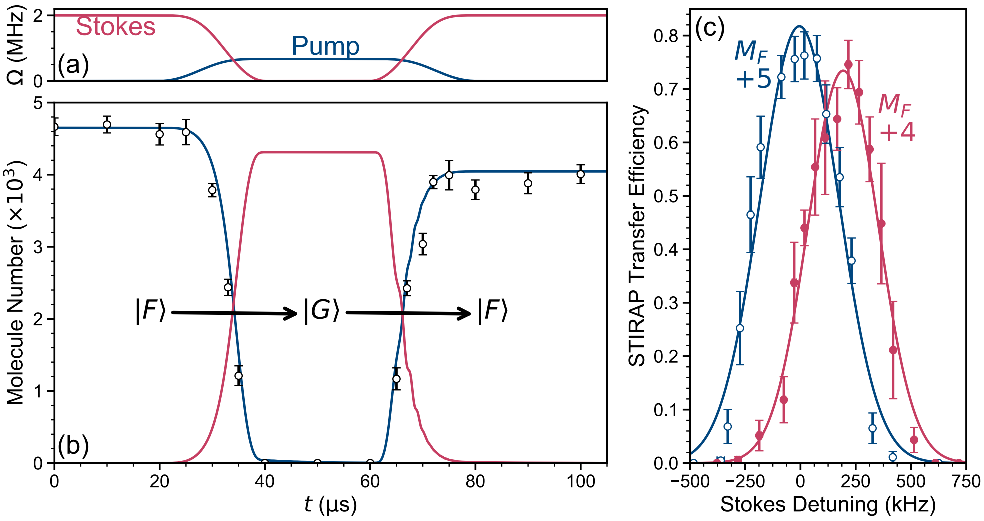

Figure 4.5: STIRAP transfer of ^{87}Rb^{133}Cs molecules to the rovibronic ground state with hyperfine state control. (a) Pulse sequence used for transfer. To transfer the molecules, the intensities of the pump and Stokes light are changed sinusoidally over 20 µs. (b) Feshbach state population at various times during the round-trip STIRAP pulse sequence. Molecules are first transferred to the hyperfine and rovibronic ground state $|G\rangle \equiv |N = 0, M_F = 5\rangle$ where they may no longer be dissociated for imaging. We therefore transfer the molecules back to the initial Feshbach state at the end of the sequence to allow imaging. Transfer efficiency in each direction is 92(1)%. The red and blue lines are the ground and Feshbach state populations calculated with no-free parameters as described in the main text and [140]. (c) STIRAP round-trip efficiency as a function of the detuning for two different linear polarisations of the Stokes light. The pump laser is left on resonance and is polarised parallel to the magnetic bias field. With the Stokes laser polarised parallel to the magnetic field we can access a hyperfine state with $M_F = 4$ (red filled circles). With perpendicular polarisation we can access the spin-stretched $M_F = 5$ hyperfine state which is the lowest energy and therefore absolute ground hyperfine state (blue empty circles).

spin-stretched $M_F = 5$ state is the absolute ground state, i.e. it is the lowest energy hyperfine level of the rovibronic ground state.

Understanding our ground-state transfer requires that the peak Rabi frequencies for each transition are well known. This is measured by direct observation of Rabi oscillations of the molecule population between the states, as shown in Fig. 4.6. For the pump transition, we simply pulse on the resonant pump light for a variable time and measure the population of molecules remaining in the initial Feshbach state. In Fig 4.6(a), data with the dipole trap on and off are shown. With the dipole trap *on*, rapid dephasing due to the variable

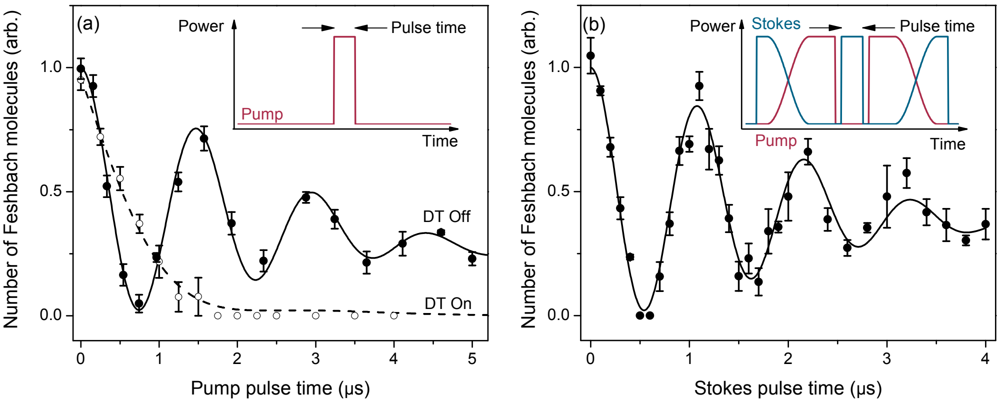

Figure 4.6: Rabi oscillations on (a) the pump and (b) the Stokes transitions. A fit to each is shown, which includes decay of the excited state and dephasing from spatial variation of the Rabi frequency. Inset are sketches of the pulse sequences for each measurement, with the pump laser in red and the Stokes in blue. For the pump, we show the effect of carrying out the same pulse sequence with the dipole trap (DT) on (empty circles) and off (filled circles). We cannot drive Rabi oscillations in the presence of the dipole trap as explained in the main text. For the Stokes, we transfer the molecules to the ground state by STIRAP before driving the oscillations, and then transfer any remaining ground state population back to the Feshbach state for detection.

transition AC Stark shift across the cloud means that we no longer observe Rabi oscillations. Rabi oscillations on the Stokes transition are observed by first transferring the molecules to the ground state. The resonant Stokes light is then pulsed on for a time before we reverse the STIRAP process to measure the number of remaining molecules. The measurement of Rabi frequency on the Stokes transition is therefore measuring the number of molecules remaining in the ground state as a function of the duration of the Stokes light pulse. Rabi oscillations on each transition with the dipole trap off are fit using a damped cosine function to extract Rabi frequencies for the pump and Stokes transitions of $\Omega_{\mathrm{P}}/(2\pi) = 666(6)$ kHz and $\Omega_{\mathrm{S}}/(2\pi) = 915(7)$ kHz, with an intensity of approximately ~ 0.9 kW cm^{-2} in each beam. The visible dephasing of the Rabi oscillations arises as a result of the intensity variation of the tightly focussed STIRAP light across the cloud.

We model the transfer using a numerical simulation based on an open three-level 'lambda' system. Loss is included in the system as the decay of the intermediate state to a fourth 'dump' level at a rate given by the linewidth Γ. We estimate the linewidth of the excited state from the loss of molecules dur-

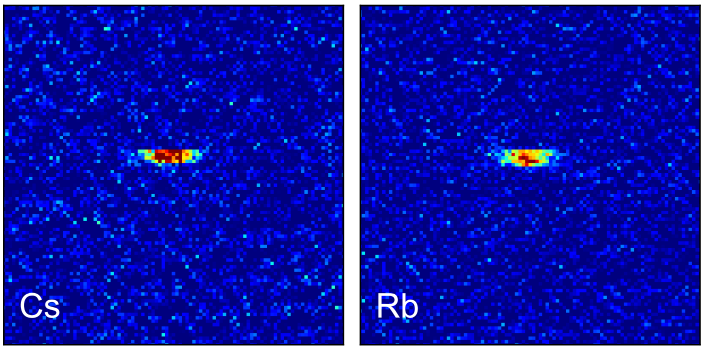

Figure 4.7: Absorption images of ~ 4000 ^{87}Rb and ^{133}Cs atoms resulting from the dissociation of ground state molecules. The dipole trap intensities are increased to compress the atoms prior to imaging, and each species is imaged in the dipole trap with minimal time of flight.

ing the Rabi oscillation measurements. Our best estimate for this linewidth is $\Gamma/(2\pi) = 35(3)$ kHz. By diagonalising the appropriate Hamiltonian for our 'four' level system including uncorrelated noise between the two driving lasers [140], we produce the theory lines for population transfer shown in Fig. 4.5. This calculation is performed using our measured linewidth and Rabi frequencies and hence has no free parameters. Our theoretical model describes the experimentally observed STIRAP efficiency remarkably well. Our transfer efficiency is likely limited by the laser linewidth and available light intensity.

4.3 Imaging

At present, imaging in our experiment is performed by reversing the routine for molecule creation to dissociate the molecules back to their constituent atoms. The resultant atoms are imaged by standard atomic absorption imaging at low magnetic field. Atom numbers are recorded for each species and the recorded number of molecules for each experimental run is the average of these two numbers. As this process requires STIRAP back to the initial weakly-bound Feshbach state, it is very sensitive to changes in magnetic field and we can only probe molecules in the centre of the STIRAP beams. However, this method has its advantages as it is hyperfine-state selective and the atom imaging process is well-known and robust.

To improve signal to noise when imaging the small number of atoms remaining at the end of our experimental sequence, we increase the powers in each dipole trap beam to $\sim$ 3W during the dissociation sequence. This compresses the atoms, maximising the optical depth of our absorption images, and allowing imaging down to a few hundred atoms. Each species is imaged in-situ with minimal time of flight. There is a delay between the imaging pulses for the two atomic species. The dipole trap is switched off for 50 µs during the Cs probe pulse, after which the atoms are recaptured until the Rb probe pulse 5 ms later. A typical set of compressed-atom absorption image can be seen in Fig. 4.7.

Direct imaging the molecules could be less sensitive to magnetic field variation and would give additional information about the spatial distribution and temperature of molecules in the trap. However, to get an image with high optical depth we require a sufficiently *closed* transition such that each molecule can scatter multiple photons. A previous study using ^{40}K^{87}Rb showed that the *open* transition between the rovibronic ground state and the $v = 3$ level of the $a^1\Pi$ state can be used to perform such direct absorption imaging of molecules despite a branching ratio $\eta = 0.14$ [168]. A mostly-closed transition in ^{40}K^{87}Rb has been identified as potentially good for laser cooling between the $|X^1\Sigma^+, v = 0, N = 1\rangle$ and $|b^3\Pi_{0+}, v = 0, N = 0\rangle$ states [169], and may also be used for improved direct imaging. An analogous transition also exists in ^{87}Rb^{133}Cs where the decay of the $b^3\Pi_{0+}$ state to the $a^3\Sigma^+$ state is deeply suppressed due to a small transition dipole moment and small energy of the emitted photon [138, 170]. Based on the known Franck-Condon factors for this transition ($\lambda \approx 1145$ nm) [139], with two vibrational repumping lasers we could expect to scatter $\sim$ 100 photons before only 50% of the molecules remain in the ground state. This may be useful in the future for direct imaging of molecules, though would require transfer of the molecules to the first rotationally excited state prior to imaging.

4.4 Temperature

Accurate measurement of the temperature T of the atomic/molecular sample requires the measurement of the cloud's expansion in free space over time.

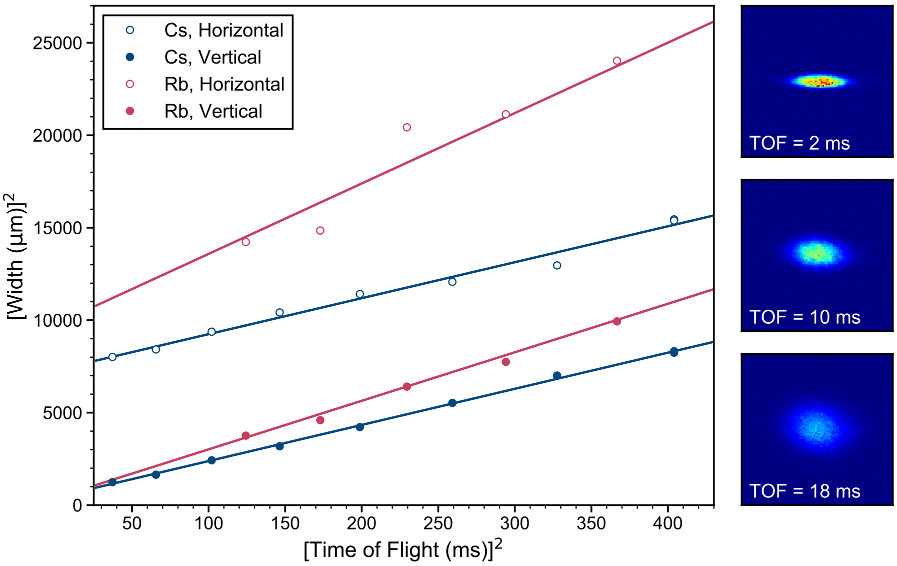

Figure 4.8: Temperature measurement of the atomic mixture in the levitated trap at the end of the dipole trap evaporation ramps just prior to Feshbach association. Each data point is a result of a single run of the experiment. We observe a faster expansion of the Rb atoms due to their lower mass. We find average temperatures of 0.28(1) µK and 0.280(3) µK for the Cs and Rb atoms respectively.

In the experiment, we turn off the optical and magnetic traps and allow the cloud to fall in free space. By varying the time between the traps switching off and the imaging sequence, we vary the time of flight experienced by the atoms or molecules. We get the width of the cloud by fitting the absorption images assuming a Gaussian density distribution. The $1/e^2$ width of the cloud σ increases with time of flight t such that

$$\sigma^2 = \sigma_0^2 + \frac{k_\mathrm{B}T}{m}t^2, \tag{4.1}$$

where σ_0 is the trapped cloud width, m is the mass, and k_B is the Boltzmann constant. Hence, by plotting the cloud width squared (σ^2) against the time of flight squared (t^2) we expect a linear correlation with gradient $\frac{k_\mathrm{B}T}{m}$.

A temperature measurement for the atomic mixture at the end of the dipole trap evaporation is shown in Fig. 4.8. Here, due to the large number of atoms available, images with high optical depth may be taken for flights of up to 25 ms before the atoms fall out of the imaging field of view[2]. When performing similar measurements using the molecules as shown in Fig. 4.9,

---

[2] Longer times of flight may be observable by magnetically levitating the atoms.

much shorter times of flight (< 9 ms) must be used as the initial numbers and hence optical depth of the images is much lower. In addition, the process of dissociation and switching off of the large magnetic fields limits the minimum time of flight to 3.3 ms. The total range of expansion times we are able to image across is therefore around 5 ms over which the cloud expands by less than a factor of two; this limits the certainty in the measured temperature of the molecules. We find an average translational temperature for the molecules in the pure optical trap of 0.9(1) µK. This temperature indicates that the transfer between the magnetically levitated trap of the atoms and the pure optical trap of the molecules is adiabatic. Adiabatic transfer preserves the phase-space density of the trapped sample, i.e.

$$N\left(\frac{\hbar\omega}{k_{\mathrm{B}}T}\right)^{3} = \mathrm{Constant} \tag{4.2}$$

where N is the number of molecules, ω is the trap frequency, k_{B} is Boltzmann's constant, and T is the temperature. During the transfer between the magnetically levitated trap of the atoms and the pure optical trap of the molecules, the trap frequency is increased by a factor of ~ 3. As both the phase-space density and the number of molecules in the sample remains constant, the temperature must also increase by the same factor as the trap frequency.

4.5 Binding Energy

Accurate characterisation of the internal structure of even simple diatomic molecules is difficult both theoretically and experimentally. Here we will discuss the measurement of a fundamental property of the molecule - its binding energy. Our chosen method of creating ultracold molecules is well-suited to measuring this quantity as we start off with free ground-state atoms (i.e. atoms which are at the minimum dissociation energy of the molecules) and must 'remove' the $\sim h \times 114$ THz of energy from the atom-pair in a controlled way to form a tightly-bound molecule.

We begin our measurement of the binding energy by precisely measuring the frequencies of our STIRAP lasers. The transfer efficiency of STIRAP is

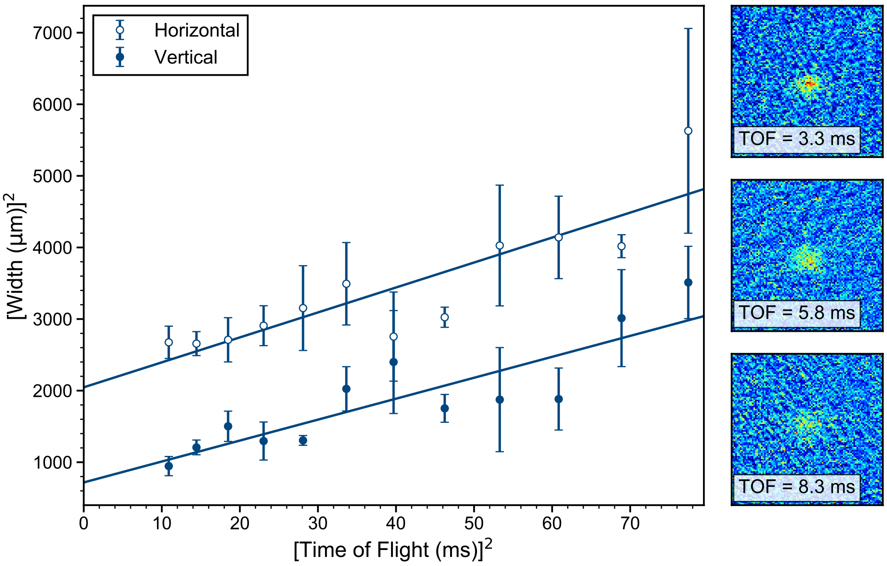

Figure 4.9: Temperature measurement of Feshbach molecules in the pure optical trap by observing the rate of expansion in free-space. Each data point is an average of 3-4 experimental runs. Due to the 5 ms delay between imaging of the two atomic species, only the Cs atom absorption images have sufficient optical depth to collect useful results. We fit the data for the cloud width in the vertical and horizontal directions and find temperatures of 0.8(1) µK and 0.9(2) µK respectively, giving an average translational temperature for the molecules of 0.9(1) µK.

maximised when the laser frequencies meet the two-photon resonance condition, while being relatively insensitive to any common detuning of both lasers from the intermediate state [131]. Therefore, the frequency difference between the two lasers when the efficiency of STIRAP is maximised yields a direct measurement of the energy difference between the rovibronic and hyperfine ground state of the molecule and the initial Feshbach state.

Our precision measurements of laser frequency are performed with reference to a GPS-referenced optical frequency comb. The frequency comb we have installed at the Durham University Department of Physics is the first of its kind, based on difference frequency generation technology developed by TOPTICA Photonics AG [171]. In a typical frequency comb, the frequency of each comb tooth N has a frequency $f = N f_{\text{rep}} + f_{\text{CEO}}$, where f_{rep} is the repetition rate of the comb and f_{CEO} is the carrier-envelope offset frequency. The key feature of the difference method implemented in the TOPTICA optical frequency comb is that the carrier-envelope offset frequency is cancelled,

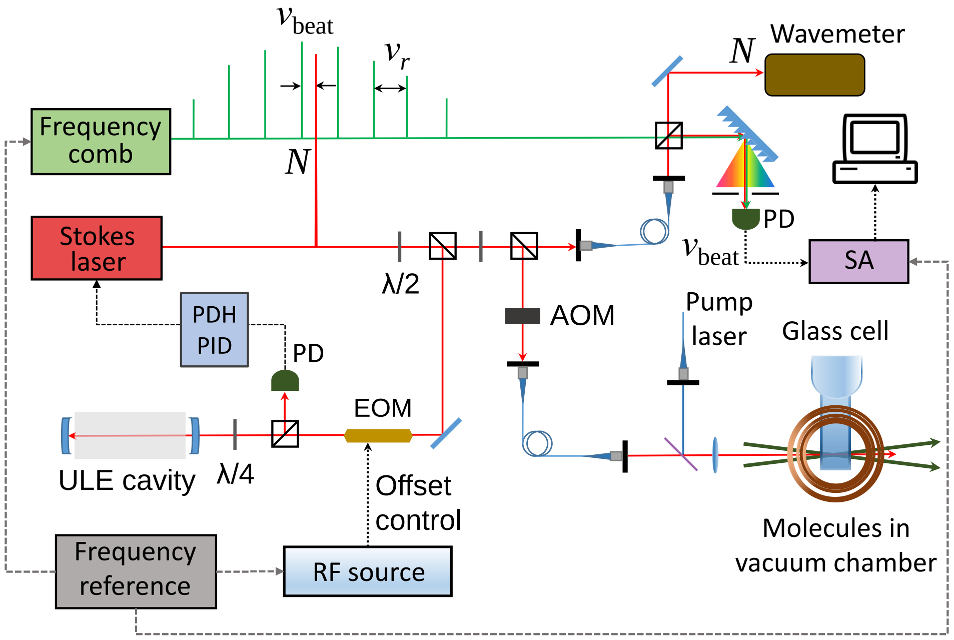

Figure 4.10: Schematic of the experiment used to perform spectroscopy while recording the beat note ν_{beat} of the STIRAP lasers with the optical frequency comb. The beat signal between each STIRAP laser and the nearest comb line N is detected on a photodiode which is connected to a spectrum analyzer (SA). The light reaching the molecules is offset by 80 MHz from that sent to the frequency comb by an acousto-optic modulator (AOM). The frequency comb, spectrum analyzers, and EOM driver are all referenced to the same 10 MHz GPS disciplined oscillator. This figure shows the setup for the Stokes laser; the setup for the pump laser is identical.

meaning that each comb tooth has a frequency $f = Nf_{\text{rep}}$ with zero frequency offset. The frequency comb is seeded by a mode-locked Er:fibre laser with an 80 MHz repetition rate, whose 10^{th} harmonic is locked to an 800 MHz ultra-low-noise oven-controlled RF oscillator, which in turn is locked to the 10 MHz output of a GPS disciplined quartz oscillator (GPSDO).

Absolute frequencies of the STIRAP lasers are measured by beating light from each laser with the nearest tooth of the frequency comb as shown in Fig. 4.10. The beat note is recorded on a spectrum analyzer (Agilent N1996 and N9320B for pump and Stokes respectively) which is referenced to the same 10 MHz GPSDO as the comb. The nearest comb tooth is identified using a wavemeter with absolute accuracy of 30 MHz (High Finesse WS-U), which is calibrated using lasers locked to well-known spectral lines in Rb, Cs, and Sr. Light sent to the frequency comb is offset from that sent to the

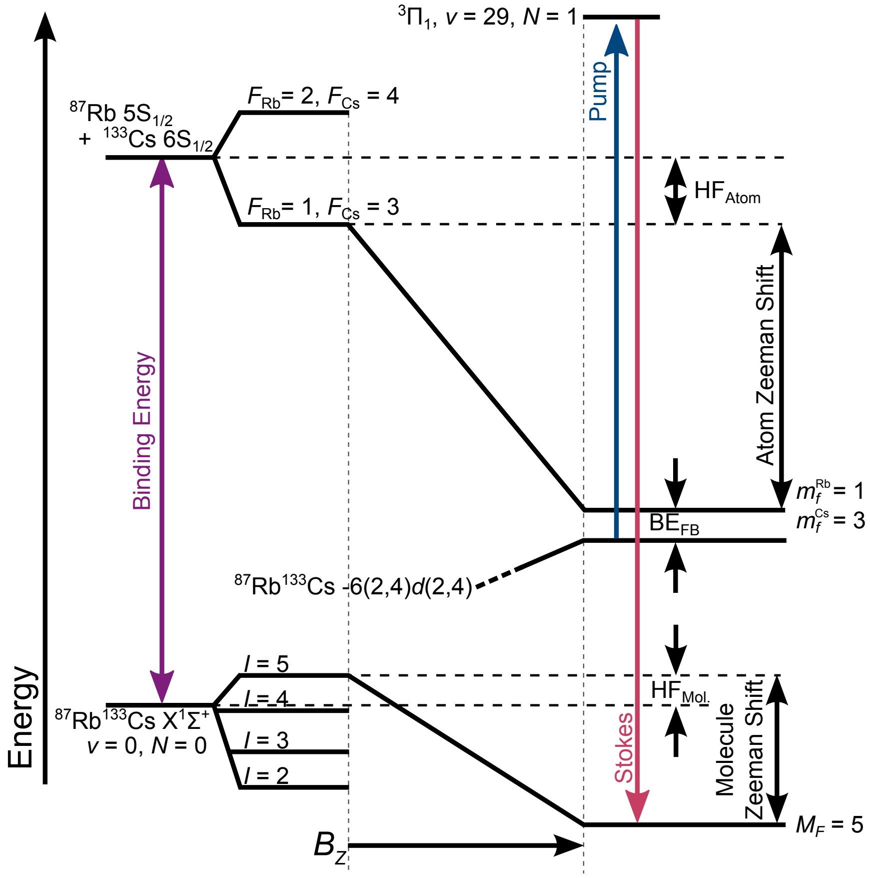

Figure 4.11: Schematic view of the energy levels involved in measuring the binding energy of ^{87}Rb^{133}Cs. The frequency difference between the STIRAP lasers gives the energy difference between the rovibronic and hyperfine ground state of the molecule with respect to the initial $|{-6(2,4)d(2,4)}\rangle$ Feshbach state. To convert this energy into a binding energy for the molecules at zero magnetic field we must consider the binding energy of the Feshbach state (BE$_{\mathrm{FB}}$), Zeeman shifts of the free-atomic and bound-molecular states, and the zero-field hyperfine splitting (HF$_{\mathrm{Atoms}}$ and HF$_{\mathrm{Mol.}}$).

molecules by the frequency of an 80 MHz acousto-optic modulator (AOM). We have measured the offset from the nominal 80 MHz of these AOMs to be -705(3) Hz with a negligible statistical uncertainty.

To measure the energy difference between the pump and Stokes transitions, we fix the frequency of the pump laser on resonance with the Feshbach and intermediate states. We then vary the frequency of the Stokes laser and measure the efficiency of the STIRAP transfer. The beat notes of both lasers with the optical frequency comb are measured throughout, and for each data point we subtract the pump and Stokes absolute frequencies measured with

Source	**Correction (MHz)**	**Error (MHz)**
$f_{\text{Stokes}} - f_{\text{pump}}$	114 258 363.067	0.006
Feshbach binding energy	1.84	0.04
Rb Zeeman	194.084	
Cs Zeeman	134.353	
RbCs Zeeman	−0.734	
Total Zeeman		0.013
Cs hyperfine	$\frac{9}{16} \times 9\,192.631\,770$	$\equiv 0$
Rb hyperfine	$\frac{5}{8} \times 6\,834.682\,611$	$< 10^{-10}$
RbCs hyperfine (I=5)	0.100	
Binding energy	114 268 135.24	0.04

Table 4.1: All the corrections, and their respective experimental errors, which must be added to each measurement of the energy difference $f_{\text{Stokes}} - f_{\text{pump}}$ to give the energy difference between the degeneracy-weighted hyperfine centroids of the free atoms and the RbCs rovibronic ground state, *i.e.* the binding energy. The uncertainty in the Zeeman shift is from the uncertainty in the measured magnetic field. The values shown are for a measurement at a magnetic field 181.538(6) G driving a transition to the $M_F = 5$ hyperfine ground state.

the comb. The result of this experiment is to find a peak as a function of Stokes frequency (see Fig. 4.5(c)), which we fit with a Gaussian lineshape to determine the energy difference between the initial and final states. We have repeated this measurement five times, each on different days. One of these measurements was performed using a different intermediate excited state $|^3\Pi_1, v = 35, N = 1\rangle$; for this measurement STIRAP was not performed and we instead used the two-photon spectroscopy routine used at the beginning of section 4.2.

To convert our measured STIRAP energy difference into a binding energy at zero magnetic field, we must correct for the Zeeman shifts in both the free-atom and bound-molecule states. The Zeeman shift of the ground-state molecular hyperfine state depends upon molecular constants which at the time had reasonable theoretical predictions, but we have since experimentally measured in chapter 5. In addition, as the energy difference we measure between the STIRAP transitions is between the ground state and the initial Feshbach state, we must also consider the binding energy of that Feshbach state. Fig. 4.11 illustrates all of the corrections which must be made, all of which depend upon magnetic field (measured using the procedure outlined in section 3.3.1). An example calculation of the binding energy from one of our measurements is shown in Table 4.1. Taking a weighted mean of our five independent measurements of the binding energy of ^{87}Rb^{133}Cs, we find

$$\begin{aligned} D_0 &= h \times 114\ 268\ 135.25(3)\ \text{MHz} \\ &= hc \times 3\ 811.574\ 714(1)\ \text{cm}^{-1}. \end{aligned}$$

Further details regarding this measurement may be found in [172].

4.6 Electric Dipole Moment

The reason we choose to work with heteronuclear diatomic molecules such as ^{87}Rb^{133}Cs is to access the large molecule-frame electric dipole moment. In order to observe an electric dipole moment in the laboratory-frame, we must apply a DC electric field which mixes states with opposite parity and gives an external axis along which the dipoles can orient themselves.

In the experiment, we observe the response of the molecules to the applied electric field as a DC Stark shift of the energy levels of the molecule (see 2.6.1 for theory). We are primarily interested in the energy shift of the rovibronic ground state of the molecules. In particular, it is important that we perform this measurement on molecules in the rotational ground state as the DC Stark shift of the molecules depends on the rotational angular momentum projection M_N which is the same for all hyperfine states with $N = 0$. The picture becomes far more complicated in higher rotational levels due to nuclear quadrupole coupling as will be seen in the remaining chapters of this thesis.

We begin by measuring the DC Stark shift of the pump transition by performing one-photon spectroscopy as described in section 4.2. The electric field is switched on for the duration of the spectroscopy light pulse. As the initial Feshbach state has a negligible electric dipole moment, this shift is equal to the Stark shift of the electronically excited state. We observe a near-linear shift of the excited state of ~ 500 kHz V^{-1} cm before an avoided crossing with a collection of higher-lying hyperfine states at ~ 500 V cm^{-1}.

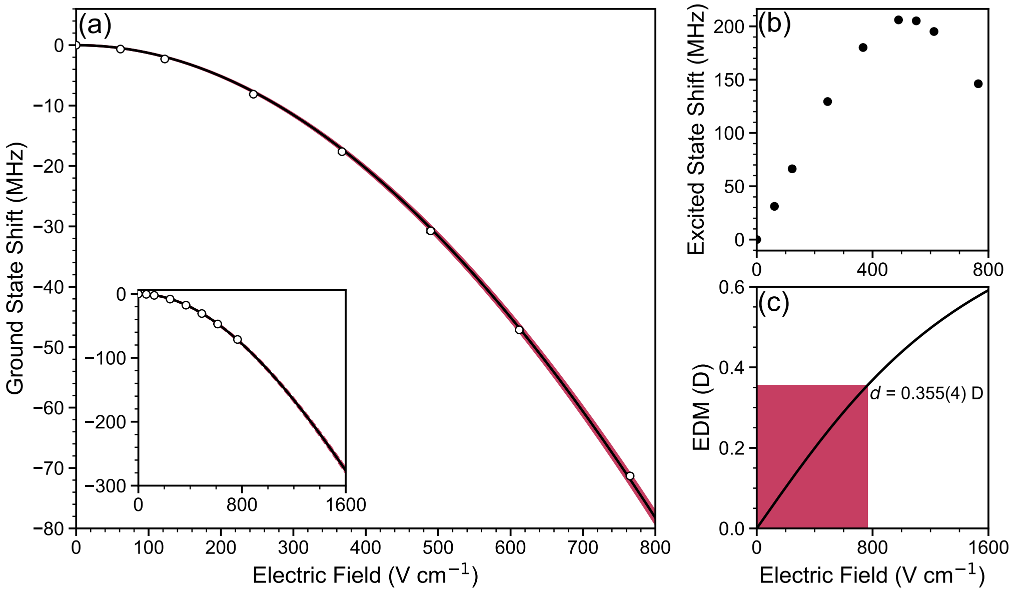

Figure 4.12: Measurement of the electric dipole moment (EDM) of ^{87}Rb^{133}Cs molecules. (a) DC Stark shift of the rovibrational ground state. The ground-state shift is equal to the DC Stark shift of the two-photon dark-state resonance used for STIRAP. White circles show experimental measurements of the ground-state shift. The black line shows the fitted AC Stark shift found by diagonalising the matrix given in Eq. 2.30. The red shaded region illustrates the systematic uncertainty in this measurement due to the uncertainty in the electric field at the molecules. **Inset:** AC Stark shift of the ground state in the full-region accessible to the experiment in the absence of charge build-up on the cell walls. (b) AC Stark shift of the intermediate excited state. An avoided crossing is observed with a group of higher lying hyperfine states around $E = 500$ V cm^{-1}. (c) Laboratory-frame dipole moment in the electric field region currently accessible. The red-shaded region shows the electric fields at which we have been able to perform measurements with negligible charge build-up on the cell. The highest space-fixed electric dipole moment generated so far is 0.355(4) D.

The DC Stark shift of the ground state is given by the energy shift of the two-photon dark-state resonance used for STIRAP. We measure this by performing two-photon spectroscopy (see 4.2) in an electric field with the pump laser set on resonance with the Stark shifted excited state transition. The experimental results and fitting are shown in Fig. 4.12. By diagonalising the matrix given in Eq. 2.30 we can fit the experimental data with the molecule-frame dipole moment as the only free parameter. We find a permanent electric dipole moment of

$$d_0 = 1.225(3)(8)\text{ D}. \tag{4.3}$$

The first uncertainty is the statistical and the second is systematic, arising from the uncertainty in the electric field. The systematic uncertainty is illustrated in Fig. 4.12(a) by the red shaded region.

Although in theory our electrode and power supply configurations could allow us to investigate electric fields up to $\sim$ 1500 V cm^{-1}, we are only able to access fields of $\sim$ 800 V cm^{-1} before we find a measurable charge on the surface of the fused silica cell. This accessible electric field translates to a laboratory-frame electric dipole moment of $d = 0.355(4)$ D as shown in Fig. 4.12(c).

4.7 Summary

We are able to produce a sample of over 4000 ^{87}Rb^{133}Cs molecules in their rovibronic and hyperfine ground state. The molecules are spatially separated from the atomic mixture from which they are associated via the Stern-Gerlach effect and are trapped in a purely optical potential where they have a temperature of 0.9(1) µK measured by time-of-flight expansion of the molecular cloud in free space. We have measured the binding energy of the molecular ground state by precisely measuring the frequency difference between our two narrow-linewidth STIRAP lasers with reference to an optical frequency comb. We find a binding energy of $D_0 = hc \times 3\ 811.574\ 714(1)$ cm^{-1}. Finally, by measuring the DC Stark shift of the rovibronic ground state of the molecules in a static electric field, we have measured the molecule-frame electric dipole moment of the molecule to be $d_0 = 1.225(3)(8)$ D. This translates to a maximum laboratory-frame electric dipole moment of $d = 0.355(4)$ D given the largest electric fields we currently have access to.

Chapter 5

Coherent Control of the Rotational and Hyperfine State

Full control of the quantum state has been an invaluable tool in ultracold atom physics; it is therefore highly important to develop similar methods for ultracold molecules, which allows us to fully address the complex rotational and hyperfine structure. Such control is at the heart of nearly all proposals for applications of ultracold polar molecules. For example, the rotational states of molecules might be used as pseudo-spins to simulate quantum magnetism [18, 22]. This requires a coherent superposition of opposite-parity states to generate dipolar interactions [18], which may be probed by microwave spectroscopy [74, 173]. Similarly, hyperfine states in the rotational ground state have been proposed as potential qubits for quantum computation [23, 81, 174]. In this context, robust coherent transfer between the hyperfine states is essential. Such transfer can be achieved using a scheme proposed by Aldegunde *et al.* [175] which employs microwave fields to manipulate the molecular hyperfine states. This approach has been implemented for the fermionic heteronuclear molecules ^{40}K^{87}Rb [70, 176] and ^{23}Na^{40}K [177], leading to ground-breaking studies of the dipolar spin-exchange interaction [74] and nuclear spin coherence time [81].

In this chapter, we report microwave spectroscopy of bosonic ^{87}Rb^{133}Cs in its ground vibrational state, and demonstrate our ability to coherently transfer our molecules from the absolute rovibrational and hyperfine ground state to a chosen single hyperfine state in either the first-excited, second-excited, or ground rotational states. We begin by discussing the selection rules which dictate which transitions are allowed between rotational and hyperfine states (5.1). We then show the high precision with which we can map out the rotational energy structure of $^{87}\text{Rb}^{133}\text{Cs}$ in the lowest vibrational state using externally applied microwave fields. We use these spectroscopic measurements to obtain new values for the rotational constant, scalar spin-spin coupling constant, electric quadrupole coupling constants, and nuclear g-factors (including shielding) for the molecule (5.2). With this understanding of the molecule, we are able to predict the transition frequencies between hyperfine levels in neighbouring low-lying rotational levels to typically less than 1 kHz. Transfer between these hyperfine levels is carried out using microwave π-pulses. With one-photon excitation, we are able to transfer the molecules to a range of single hyperfine levels in the first excited rotational state. We also extend this to use a two-photon pulse sequence to transfer molecules to either a different hyperfine level of the rovibrational ground state, or a single hyperfine level of the second rotationally excited state (5.3). Finally, we discuss the use of superposition states created using external microwaves, and demonstrate work done on this topic in the experiment so far (5.4).

5.1 Quantum Numbers and Allowed Transitions

As discussed in section 2.5, the hyperfine structure of molecules is far more complex than for a single atom. The total number of hyperfine states present depends upon both the nuclear spins of the constituent nuclei and the rotational energy of the molecule, and the quantum numbers that can be used to identify these states depends on the external magnetic field present. The nuclear spins in $^{87}\text{Rb}^{133}\text{Cs}$ are $I_{\text{Rb}} = 3/2$ and $I_{\text{Cs}} = 7/2$. At zero field, the total angular momentum $\boldsymbol{F} = \boldsymbol{N} + \boldsymbol{I}_{\text{Rb}} + \boldsymbol{I}_{\text{Cs}}$ is conserved. For the rotational ground state ($N = 0$), the total nuclear spin $\boldsymbol{I} = \boldsymbol{I}_{\text{Rb}} + \boldsymbol{I}_{\text{Cs}}$ is very nearly conserved, and there are 4 hyperfine states with $I = 2$, 3, 4 and 5 with separations determined by c_4 [145] (as shown earlier in Fig. 2.8). For excited rotational states, however, only F is conserved and I is a poor quantum number.

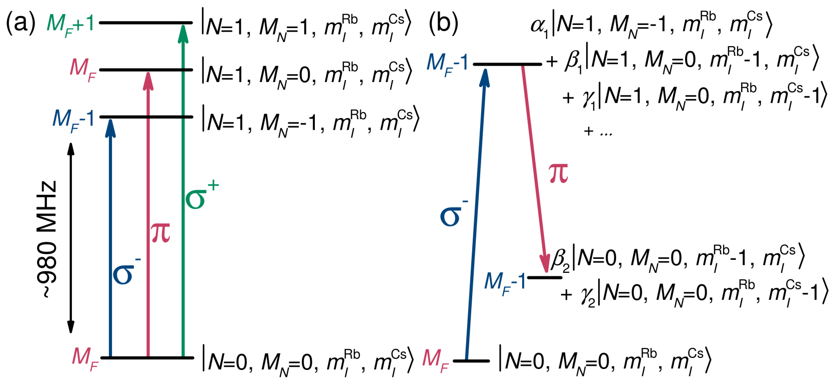

Figure 5.1: Electric dipole transitions in ^{87}Rb^{133}Cs between the $N = 0$ and $N = 1$ rotational levels in the vibrational ground state. (a) Electric dipole transitions between $N = 0$ and $N = 1$ rotational levels in the absence of hyperfine coupling. (b) Two-photon pulse sequence used to transfer population to a different hyperfine level of $N = 0$, taking advantage of the mixing caused by hyperfine coupling.

An external magnetic field splits each rotational manifold into $(2N+1)(2I_{\text{Rb}}+1)(2I_{\text{Cs}}+1)$ Zeeman-hyperfine sublevels, so there are 32 levels for $N = 0$ and 96 levels for $N = 1$. Assignment of quantum numbers to the individual hyperfine levels is non-trivial and depends on the magnetic field regime [145]. The field mixes states with different values of F that share the same total projection M_F. At low field, the levels are still approximately described by F and M_F (equivalent to I and M_I for $N = 0$). At high field, however, the nuclear spins decouple and the individual projections M_N, m_I^{Rb} and m_I^{Cs} become nearly good quantum numbers, with $M_F = M_N + m_I^{\text{Rb}} + m_I^{\text{Cs}}$. The only quantum number that is good in all field regimes is M_F, and this is the only good quantum number at the magnetic field at which we operate our experiment.

A microwave field induces electric dipole transitions between rotational levels. At low field, all transitions allowed by the selection rules $\Delta F = 0, \pm 1$ and $\Delta M_F = 0, \pm 1$ have significant intensity. At higher field, however, additional selection rules emerge. If hyperfine couplings are neglected, electric dipole transitions leave the nuclear spin states unchanged ($\Delta m_I^{\text{Rb}} = \Delta m_I^{\text{Cs}} = 0$) and are allowed only between neighboring rotational states such that $\Delta N = \pm 1$, $\Delta M_N = 0, \pm 1$ for microwave polarizations $\pi, \sigma^{\pm}$. In the absence of hyperfine interactions (where M_N would be a good quantum number) we would be able to drive at most three transitions from any given hyperfine level, as shown in Fig. 5.1(a). Hyperfine coupling mixes states with different values of M_N, m_I^{Rb} and m_I^{Cs}, and additional transitions become allowed. The couplings are principally due to scalar spin-spin coupling in $N = 0$ and nuclear quadrupole coupling in $N = 1$. The mixing allows us to use a multi-photon scheme to move the population to different hyperfine states of the rotational ground state. Fig. 5.1(b) shows a simple example of this scheme, using two microwave photons to change the hyperfine state by $\Delta M_F = -1$.

5.2 Spectroscopy of $N = 1$

Our apparatus is equipped with two omnidirectional $\lambda/4$ antennas placed close to the outside of the fused silica cell as described in section 3.5. The polarization from each is roughly linear at the position of the molecules. They are oriented perpendicular to each other and aligned with respect to the static magnetic field such that one preferentially drives transitions with $\Delta M_F = 0$ and the other drives those with $\Delta M_F = \pm 1$. Each antenna is connected to a separate signal generator, which is frequency referenced to an external 10 MHz GPS reference. Fast (∼ns) switches are used to generate microwave pulses of well-defined duration (typically 1 µs - 500 µs). The antenna design and other experimental setup details are described in more detail in Section 3.5.

To avoid AC Stark shifts of the transition centres, the optical trap is switched off throughout the spectroscopy; the transition frequencies are thus measured in free space[1]. This limits the maximum available interrogation times with a single microwave pulse to < 1 ms before we observe significant heating and loss of the molecules. In addition, the large dipole moment of the molecule (1.225 D [29]) makes it remarkably easy to drive fast Rabi oscillations between neighboring rotational states. These Rabi oscillations do not dephase over the timescales available in the experiment due to the large wavelength of the microwaves ~ 30 cm and high uniformity of the magnetic bias field. To perform the final spectroscopy, therefore, we pulse on the microwave field for a time (t_{pulse}) which is less than the duration of a π-pulse for the relevant

---

[1] The effect of the dipole trapping light on the microwave transitions will be investigated later in chapter 6.

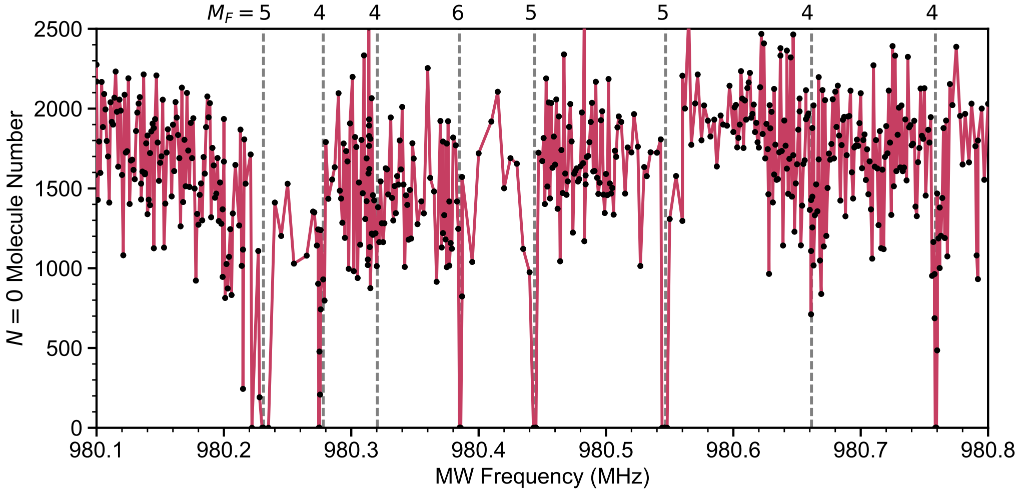

Figure 5.2: Initial microwave spectroscopy between the $|N = 0, M_F = 5\rangle$ rotational and hyperfine ground state to the various hyperfine sublevels of the first rotationally excited state. Vertical dashed lines show the measured transition frequencies from the final spectroscopy shown in Fig. 5.4.

transition ($< t_\pi$). We then observe the transition as an apparent loss of molecules as they are transferred into the first-excited rotational state. In order to find t_π we begin by pulsing the microwaves on at high power where the transition is relatively broad; by varying t_{pulse} with fixed frequency, we can observe Rabi oscillations and from there determine the appropriate pulse length for spectroscopy.

An early attempt at microwave spectroscopy was performed using a fixed microwave pulse duration at the maximum power output by the antenna. The result of this can be seen in Fig. 5.2, and shows observable ‘loss’ of molecules close to 6 of the 8 observed transitions. However, this method was found to be unreliable due to the range of strengths of the available transitions and the possibility of driving Rabi oscillations when off-resonant due to broadening of the transitions.

To perform accurate spectroscopy, radically different t_{pulse} are required for different transitions, depending on the transition strength and antenna used. We find that the widths of all of the features we measure are Fourier-transform limited, i.e. the width is proportional to $1/t_{\text{pulse}}$, the linear relationship between pulse duration and spectroscopic width is shown in Fig. 5.3(c). To precisely measure the position of each of the transition cen-

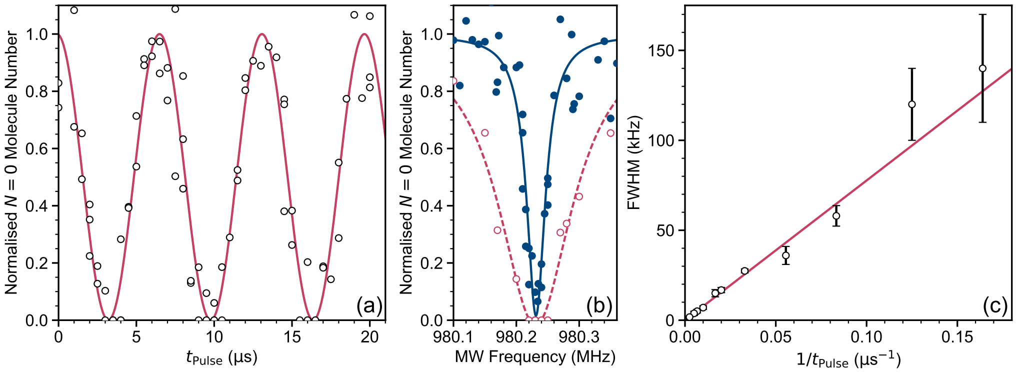

Figure 5.3: Method and Fourier-transform limiting of the microwave spectroscopy. **(a)** Fast Rabi oscillations performed close to resonance with the transition between $|N = 0, M_F = 5\rangle$ and the lowest energy $|N = 1, M_F = 5\rangle$ states. **(b)** Spectroscopy is performed by setting the pulse duration t_{Pulse} to approximately a π-pulse for a given microwave power. The full-width half-maximum (FWHM) of the Lorentzian spectroscopic feature depends upon the duration of the pulse used. Spectroscopy using a 6.1 μs pulse (red open circles and dashed line) and an 18 μs pulse (blue closed circles and solid line) are shown. **(c)** FWHM of the Lorentzian feature against inverse pulse duration for all spectroscopy performed. A linear fit is shown which is fixed to go through the origin and has a gradient of 0.78(3).

tres, we need to minimise the width of the spectroscopic feature. We therefore iteratively reduce the power to get slower Rabi oscillations and allow longer pulse durations. We are able to drive π transitions weakly using the antenna intended for $\sigma^{\pm}$ and *vice versa*, and the spectroscopy for the $M_F = 6$ transition is performed in this way to minimize the width of the spectroscopic feature. We carry out the spectroscopy at two different magnetic fields $\sim$ 23 G apart; the field is calibrated using the microwave transition frequency between the $|f = 3, m_f = +3\rangle$ and $|f = 4, m_f = +4\rangle$ states of Cs as described in Section 3.3.1.

With the population initially in the lowest hyperfine level ($M_F = 5$) of the rovibrational ground state, we expect to find a maximum of 10 transitions to the first-excited rotational state $|N = 1, M_F = 4, 5, 6\rangle$. We are able to observe 8 of these transitions, the measured centre frequencies of which are shown in Table 5.1. A complete set of experimental spectra at a magnetic field of $\sim$ 181.5 G is shown in Fig. 5.4(a-h). The intensity of each of these transitions depends on the magnitude of the component of the destination state with the same nuclear spin as the initial state. Calculations of the ex-

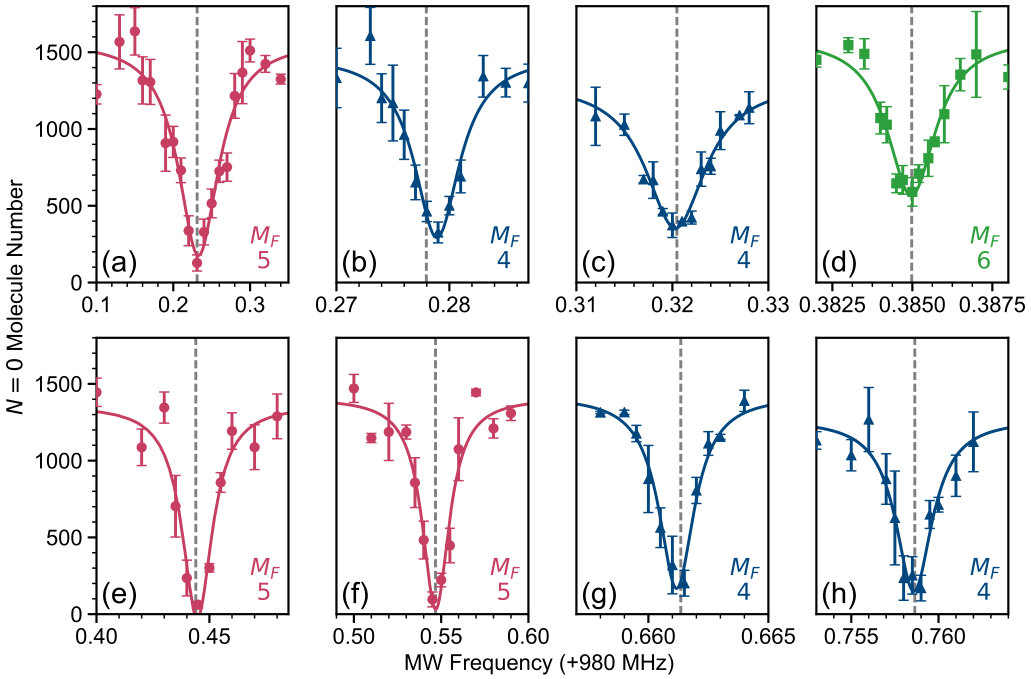

Figure 5.4: Microwave spectra at a magnetic field of 181.5 G. **(a-h)**: Experimentally observed spectra showing all of the microwave transitions from $|N=0, M_F=5\rangle$ to $|N=1, M_F=4\rangle$ observed in this work. The vertical lines shows the transition frequencies given by the least-squares fit to obtain spectroscopic constants. The pulse durations used, chosen to be less than a π-pulse for each transition, are **(a)** 12 µs, **(b)** 150 µs, **(c)** 100 µs, **(d)** 400 µs, **(e)** 60 µs, **(f)** 50 µs, **(g)** 400 µs, **(h)** 200 µs.

pected intensities of the two unseen transitions show that the relative transition probability is $\sim 10^{-4}$ lower than for those we do observe.

We fit our model to the experimental spectra by minimizing the sum of the squared quotients between each residual and the uncertainty of the line. We fit the rotational constant, nuclear quadrupole constants and scalar nuclear spin-spin constant. The nuclear g-factors and shielding coefficients are multiplied together in the Hamiltonian so it is not possible to separate them, and we therefore fit the shielded g-factors $g_{\text{Rb}} \cdot (1 - \sigma_{\text{Rb}})$ and $g_{\text{Cs}} \cdot (1 - \sigma_{\text{Cs}})$. The resulting values, along with the values of parameters held fixed at theoretical values, are given in Table 5.2.

The fitted hyperfine parameters in Table 5.2 are all within 10% of the values predicted from DFT calculations [145], except for $(eQq)_{\text{Cs}}$, which is about 15% larger than calculated. This helps to calibrate the probable accuracy of the calculations for other alkali-metal dimers. The fitted value

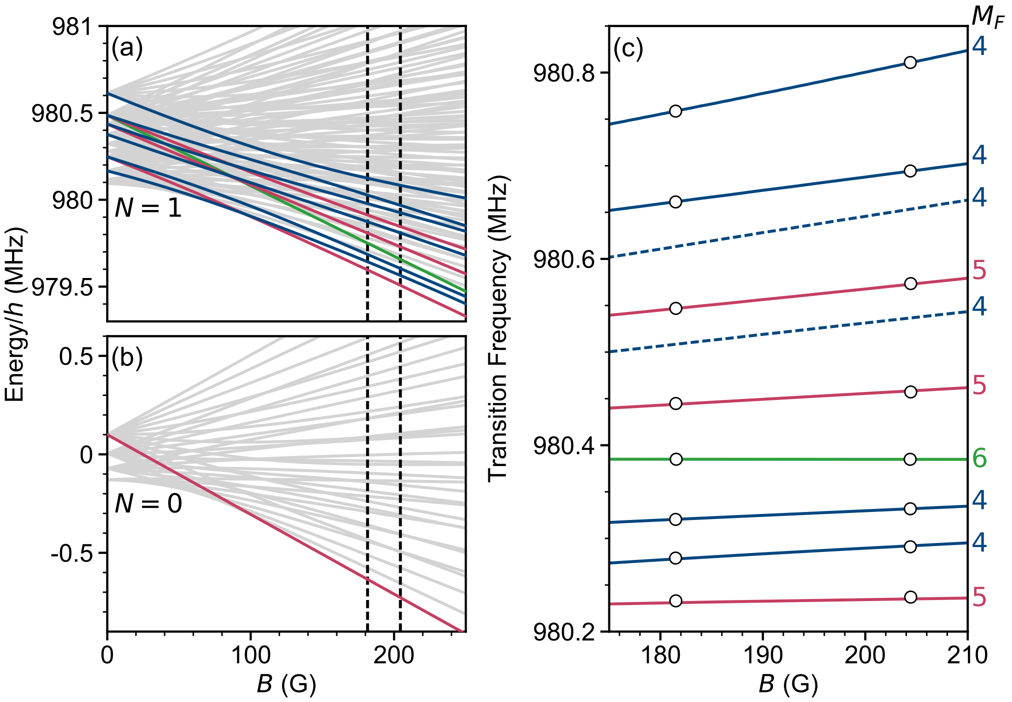

Figure 5.5: Microwave spectroscopy of ^{87}Rb^{133}Cs with varying applied magnetic field. Hyperfine Zeeman structure of the **(a)** $N = 1$ and **(b)** $N = 0$ rotational states. The $M_F = 5$ initial state in $N = 0$ is highlighted as a bold red line. The 10 states in $N = 1$ that are accessible from this initial state are shown as bold blue ($M_F = 4$), red ($M_F = 5$), and green ($M_F = 6$) lines. The vertical dotted lines mark the two magnetic fields at which spectroscopy is performed in this work. **(c)** Comparison of experimentally measured transition frequencies from $|N = 0, M_F = 5\rangle$ to $|N = 1, M_F = 4, 5, 6\rangle$ with the fitted theory. Dashed lines indicate transitions that are weakly allowed but we have not observed. Error bars are not visible at this scale.

$c_4 = 19.0(1)$ kHz removes one of the two largest sources of error in the determination of the binding energy D_0 of ^{87}Rb^{133}Cs (see 4.5). The fitted values of the shielded g-factors $g_{\mathrm{Rb}} \cdot (1 - \sigma_{\mathrm{Rb}}) = 1.829(2)$ and $g_{\mathrm{Cs}} \cdot (1 - \sigma_{\mathrm{Cs}}) = 0.733(1)$ are consistent with the corresponding atomic values, $1.827\,232(2)$ [179] and $0.732\,357(1)$ [180] (with the sign convention of Eq. 2.28c). The latter include shielding due to the electrons in the free atoms. Our values may be used in conjunction with the calculated molecular shielding factors ($\sigma_{\mathrm{Rb}} = 3531$ ppm and $\sigma_{\mathrm{Cs}} = 6367$ ppm [145]) to obtain values of the "bare" nuclear g-factors 1.836(3) and 0.738(1).

Fitting of the spectra and the observed transition intensity variation also gives the composition of the accessible hyperfine levels in either the coupled

$\boldsymbol{M_F}$	$\boldsymbol{B}$ **(G)**	$\boldsymbol{f}_{\text{The.}}$ **(kHz)**	$\boldsymbol{f}_{\text{Exp.}}$ **(kHz)**	$\boldsymbol{\Delta f}$ **(kHz)**
+5	181.507(2)	980 231.07	980 233(2)	−2(2)
	204.436(2)	980 235.14	980 237(1)	−2(1)
+4	181.484(1)	980 277.96	980 278.9(2)	−0.9(2)
	204.397(2)	980 292.08	980 291.0(2)	1.1(2)
+4	181.487(1)	980 320.47	980 320.4(2)	0.1(2)
	204.397(2)	980 331.83	980 331.8(3)	0.0(3)
+6	181.541(2)	980 384.98	980 384.97(6)	0.01(6)
	204.38(1)	980 384.87	980 384.90(5)	−0.03(5)
+5	181.507(2)	980 443.97	980 444.8(7)	−0.8(7)
	204.436(2)	980 458.35	980 457.2(8)	1.1(3)
+5	181.507(2)	980 546.75	980 546.9(7)	−0.2(7)
	204.436(2)	980 572.86	980 573.5(6)	−0.6(6)
+4	181.487(1)	980 661.35	980 661.15(6)	0.20(6)
	204.397(2)	980 694.22	980 694.35(5)	−0.13(5)
+4	181.487(1)	980 758.64	980 758.6(1)	0.0(1)
	204.397(2)	980 810.62	980 810.8(3)	−0.2(3)

Table 5.1: Microwave transitions found in ^{87}Rb^{133}Cs from $|v=0,N=0\rangle$ to $|v=0,N=1\rangle$. All transitions start from the spin-stretched $M_F=+5$ hyperfine level of the rotational ground state. Each transition is labeled by the M_F quantum number of the destination hyperfine level in the first-excited rotational state.

Constant	**Value**	**Ref.**
I_{Rb}	$3/2$	
I_{Cs}	$7/2$	
d_0	1.17(2)(4) D	[28]
	1.225(3)(8) D	This Work [29]
D_0	$h \times$ 114 268 135.25(3) MHz	This Work [172, 178]
B_v	490.155(5) MHz	[141]
	490.173 994(45) MHz	This Work [178]
D_v	213.0(3) Hz	[141]
$(eQq)_{\mathrm{Rb}}$	−872 kHz	[145]
	−809.29(1.13) kHz	This Work [178]
$(eQq)_{\mathrm{Cs}}$	51 kHz	[145]
	59.98(1.86) kHz	This Work [178]
c_{Rb}	29.4 Hz	[145]
c_{Cs}	196.8 Hz	[145]
c_3	192.4 Hz	[145]
c_4	17.3 kHz	[145]
	19.019(105) kHz	This Work [178]
g_r	0.0062	[145]
$g_{\mathrm{Rb}} \cdot (1 - \sigma_{\mathrm{Rb}})$	1.8295(24)	This Work [178]
$g_{\mathrm{Cs}} \cdot (1 - \sigma_{\mathrm{Cs}})$	0.7331(12)	This Work [178]

Table 5.2: Constants involved in the molecular Hamiltonian for ^{87}Rb^{133}Cs. Parameters not varied in the least-squares fit are taken from the literature. The majority of the fixed terms are calculated using density-functional theory (DFT) [145], with the exception of the centrifugal distortion constant D_v, which is obtained from laser-induced fluorescence combined with Fourier transform spectroscopy (LIF-FTS) [141]). The constants shown in this table are defined in Eq. 2.27.

M_F	**State Composition**
3	$+\ 0.972 \times \|0, 0, +3/2, +3/2\rangle\ +\ 0.428 \times \|0, +1, +1/2, +5/2\rangle\ +\ 0.899 \times \|0, +1, -1/2, +7/2\rangle$
3	$+\ 0.360 \times \|0, 0, +3/2, +3/2\rangle\ +\ 0.827 \times \|0, +1, +1/2, +5/2\rangle$ - $0.433 \times \|0, +1, -1/2, +7/2\rangle$
4	$+\ 0.947 \times \|0, 0, +1/2, +7/2\rangle\ +\ 0.321 \times \|0, 0, +3/2, +5/2\rangle$
3	$+\ 0.928 \times \|0, 0, +3/2, +3/2\rangle$ - $0.365 \times \|0, +1, +1/2, +5/2\rangle\ +\ 0.736 \times \|0, +1, -1/2, +7/2\rangle$
4	$+\ 0.321 \times \|0, 0, +1/2, +7/2\rangle\ +\ 0.947 \times \|0, 0, +3/2, +5/2\rangle$
5	$+\ 1 \times \|0, 0, +3/2, +7/2\rangle$

Table 5.3: State composition in the uncoupled basis for the hyperfine states currently accessible in $N = 0$ at 181.5 G. The state notation used here is $|N, M_N, m_I^{\mathrm{Rb}}, m_I^{\mathrm{Cs}}\rangle$. The states for each value of M_F are presented in the same order so that the coefficients can be compared. All coefficients are rounded to 3 significant figures. Relative intensity of each transition is proportional to the square of the coefficient for the $\Delta m_{\mathrm{I}} = 0$ term present in that transition; this is the first term presented in each case.

M_F	**State Composition**					
4	+	$0.382 \times \|1, -1, +3/2, +7/2\rangle$	+	$0.046 \times \|1, 0, +3/2, +5/2\rangle$	+	$0.067 \times \|1, +1, +3/2, +3/2\rangle$
	-	$0.265 \times \|1, 0, +1/2, +7/2\rangle$	+	$0.296 \times \|1, +1, +1/2, +5/2\rangle$	+	$0.830 \times \|1, +1, -1/2, +7/2\rangle$
4	-	$0.208 \times \|1, -1, +3/2, +7/2\rangle$	+	$0.260 \times \|1, 0, +3/2, +5/2\rangle$	+	$0.242 \times \|1, +1, +3/2, +3/2\rangle$
	+	$0.727 \times \|1, 0, +1/2, +7/2\rangle$	+	$0.540 \times \|1, +1, +1/2, +5/2\rangle$	-	$0.102 \times \|1, +1, -1/2, +7/2\rangle$
4	-	$0.017 \times \|1, -1, +3/2, +7/2\rangle$	+	$0.116 \times \|1, 0, +3/2, +5/2\rangle$	+	$0.413 \times \|1, +1, +3/2, +3/2\rangle$
	-	$0.555 \times \|1, 0, +1/2, +7/2\rangle$	+	$0.578 \times \|1, +1, +1/2, +5/2\rangle$	-	$0.416 \times \|1, +1, -1/2, +7/2\rangle$
5	$-$	$0.304 \times \|1, 0, +3/2, +7, 2\rangle$	+	$0.416 \times \|1, +1, +3/2. + 5/2\rangle$	-	$0.857 \times \|1, +1, +1/2, +7/2\rangle$
4	+	$0.015 \times \|1, -1, +3/2, +7/2\rangle$	-	$0.235 \times \|1, 0, +3/2, +5/2\rangle$	+	$0.870 \times \|1, +1, +3/2, +3/2\rangle$
	+	$0.089 \times \|1, 0, +1/2, +7/2\rangle$	-	$0.410 \times \|1, +1, +1/2, +5/2\rangle$	+	$0.110 \times \|1, +1, -1/2, +7/2\rangle$
5	$-$	$0.229 \times \|1, 0, +3/2, +7, 2\rangle$	+	$0.905 \times \|1, +1, +3/2. + 5/2\rangle$	-	$0.358 \times \|1, +1, +1/2, +7/2\rangle$
6	+	$1 \times \|1, +1, +3/2, +7/2\rangle$				
4	+	$0.687 \times \|1, -1, +3/2, +7/2\rangle$	+	$0.635 \times \|1, 0, +3/2, +5/2\rangle$	+	$0.0782 \times \|1, +1, +3/2, +3/2\rangle$
	+	$0.133 \times \|1, 0, +1/2, +7/2\rangle$	-	$0.210 \times \|1, +1, +1/2, +5/2\rangle$	-	$0.241 \times \|1, +1, -1/2, +7/2\rangle$
4	-	$0.582 \times \|1, -1, +3/2, +7/2\rangle$	+	$0.677 \times \|1, 0, +3/2, +5/2\rangle$	+	$0.0604 \times \|1, +1, +3/2, +3/2\rangle$
	-	$0.260 \times \|1, 0, +1/2, +7/2\rangle$	-	$0.273 \times \|1, +1, +1/2, +5/2\rangle$	+	$0.240 \times \|1, +1, -1/2, +7/2\rangle$
5	+	$0.925 \times \|1, 0, +3/2, +7/2\rangle$	+	$0.087 \times \|1, +1, +3/2, +5/2\rangle$	-	$0.370 \times \|1, +1, +1/2, +7/2\rangle$

Table 5.4: State composition in the uncoupled basis for the hyperfine states currently accessible in $N = 1$ at 181.5 G. The state notation used here is $|N, M_N, m_I^{\mathrm{Rb}}, m_I^{\mathrm{Cs}}\rangle$. The states for each value of M_F are presented in the same order so that the coefficients can be compared. All coefficients are rounded to 3 significant figures. Relative intensity of each transition is proportional to the square of the coefficient for the $\Delta m_{\mathrm{I}} = 0$ term present in that transition; this is the first term presented in each case.

$|N, I, F, M_F\rangle$ or uncoupled $|N, M_N, m_I^{\mathrm{Rb}}, m_I^{\mathrm{Cs}}\rangle$ basis sets. As we have already discussed earlier, the calculation in the uncoupled basis in particular can be used to predict the relative strengths of the transitions by comparing the magnitude of the nuclear spin preserving component of the destination hyperfine state. The composition of the immediately accessible hyperfine states in $N = 0$ and $N = 1$ (i.e. those accessible with 1- or 2-photon transfer respectively) are shown in Tables 5.3 and 5.4. This information may also help to explain why our STIRAP transfer only has strong enough coupling to efficiently transfer our molecules to two of the available six hyperfine levels.

The calculations of the hyperfine and rotational structure presented, along with the fitting to the experimental results, were performed by Jesús Aldegunde at the University of Salamanca and in close collaboration with Jeremy Hutson in the Department of Chemistry, Durham University.

5.3 Coherent Population Transfer

Our STIRAP transfer (see 4.2) produces molecules in a spin-stretched state, where $|m_I^{\mathrm{Rb}} + m_I^{\mathrm{Cs}}|$ has its maximum possible value and $M_N, m_I^{\mathrm{Rb}}, m_I^{\mathrm{Cs}}$ are all good quantum numbers. However, the other hyperfine states of $N = 0$, 1, and 2 are significantly mixed in the uncoupled basis set at the fields considered here, and have no good quantum numbers other than M_F. In this section we demonstrate complete transfer of the molecular population between these mixed-character hyperfine states.

The simplest transfer we can demonstrate in our system is one which only requires a single photon. This form of transfer has effectively already been shown in the previous section as it is the method by which we perform the spectroscopy. We are able to perform Rabi oscillations on all 8 transitions which we have observed between $N = 0$ and $N = 1$. Given the available microwave power and high transition strengths, the duration of a π-pulse on many of these transitions can be driven in less than <10 µs. However, the rate at which the transfer can be carried out is typically limited by the requirement that we do not want to couple to neighboring transitions. To ensure this, the Fourier width of the microwave pulse must be significantly

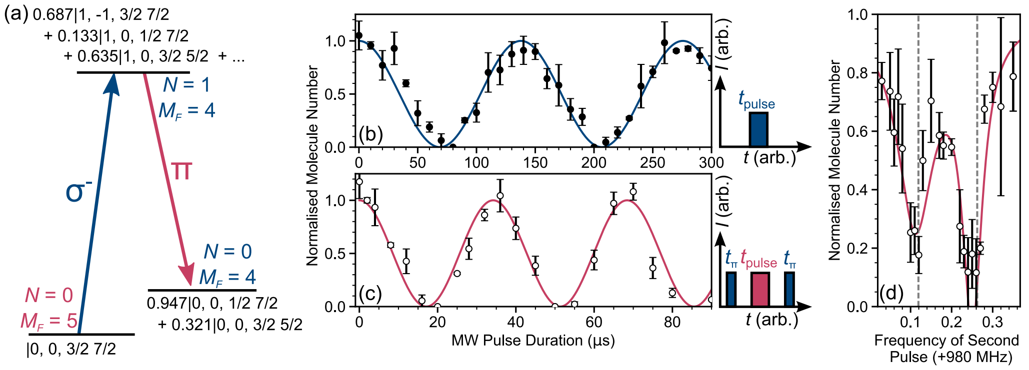

Figure 5.6: Coherent population transfer of molecules between specific hyperfine states in rotational levels $N = 0$ and $N = 1$. **(a)** Transfer scheme followed in this work. All molecules start in the lowest hyperfine state ($M_F = 5$) of $N = 0$. States are described in the uncoupled basis set $|N, M_N, m_I^{\mathrm{Rb}}, m_I^{\mathrm{Cs}}\rangle$. **(b)** Rabi oscillations in one-photon transfer of molecules to the single hyperfine level of $N = 1$ shown in (a). **(c)** Rabi oscillations in two-photon transfer, using a π-pulse on the first transition and a second microwave pulse with different frequency and polarization to drive transitions to the $M_F = +4$ hyperfine state of $N = 0$ shown in (a). **(d)** Effect of scanning the frequency of the second microwave pulse with duration $< t_\pi$. Both M_F=4 transitions in $N = 0$ are accessible with similar coupling strengths[2]. A double Lorentzian fit is shown. Dashed grey lines show the expected transition frequencies given the molecular constants fitted to the $N = 1$ spectroscopy.

less than the separation between available nearby states. As such, higher transfer speeds could be achieved by operating the experiment at a higher magnetic field, where the separation between neighbouring hyperfine levels is greater.

We can expand on this transfer method by introducing a second microwave field. As outlined in section 5.1, in the absence of hyperfine coupling, the electric-dipole selection rules demand that the nuclear spin projections m_I^{Rb} and m_I^{Cs} remain unchanged. However, a two-photon transfer can utilize a mixed character intermediate state to allow these nuclear spin projections to be changed by driving transitions to and from different components of that intermediate state. In Fig. 5.6, we demonstrate such a two-photon transfer sequence to change the populated hyperfine level in the rovibrational ground state. We begin by transferring the molecules to an $M_F = 4$ level of $N = 1$ (transition frequency = 980320.47 kHz, shown in Fig. 5.4(e)). The eigenvector component of the uncoupled basis function that couples to our initial $N = 0$ hyperfine level is $\sim$ 0.687. To ensure we do not off-

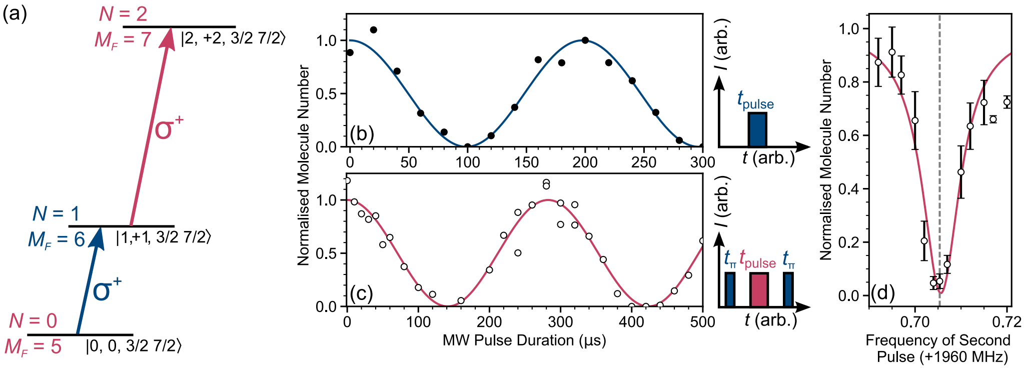

Figure 5.7: Two-step transfer between the spin-stretched and lowest energy hyperfine levels of $N = 0, 1$ and 2. **(a)** Transfer scheme followed in this work. All molecules start in the lowest hyperfine state ($M_F = 5$) of $N = 0$. States are described in the uncoupled basis set $|N, M_N, m_I^{\mathrm{Rb}}, m_I^{\mathrm{Cs}}\rangle$. **(b)** Rabi oscillations in one-photon transfer of molecules to the spin-stretched $M_F = 6$ state of $N = 1$ shown in (a). **(b)** Rabi oscillations in two-photon transfer, using a π-pulse on the first transition and a second microwave pulse with different frequency to drive a second transition to the $M_F = 7$ hyperfine level of $N = 2$ shown in (a). **(d)** Effect of scanning the frequency of the second microwave pulse with duration $< t_\pi$. The dashed grey line shows the expected transition frequency given the molecular constants fitted to the $N = 1$ spectroscopy.

resonantly couple to neighboring states we tune the microwave power such that the Rabi frequency of the transition is $\Omega_{01}/2\pi = 7.26(5)$ kHz, as shown in Fig. 5.6(b). Single π-pulses allow complete transfer of the population to the destination hyperfine level. We subsequently transfer the molecules to a different hyperfine level of $N = 0$ by applying the second microwave field with a different polarization and frequency. We choose to use π-polarized microwaves to transfer the molecules to the higher-energy of the two $M_F = 4$ levels of $N = 0$ (transition frequency 980119.14 kHz). At this field, the composition of this final level is $0.947\,|0, 0, 1/2, 7/2\rangle + 0.321\,|0, 0, 3/2, 5/2\rangle$ in the uncoupled basis $|N, M_N, m_I^{\mathrm{Rb}}, m_I^{\mathrm{Cs}}\rangle$. We observe Rabi oscillations on the second transition by pulsing on the π-polarized microwaves between two π-pulses on the σ^--polarized microwave transition, as shown in Fig. 5.6(c). Coherent transfer is achieved with a Rabi frequency of $\Omega_{10}/2\pi = 29.2(3)$ kHz.

---

[2] In fact, coupling to the lower energy $M_F = 4$ hyperfine level is the strongest. The relative coupling strengths are $0.321 \times 0.133 + 0.947 \times 0.635 \approx 0.64$ and $0.974 \times 0.133 + 0.321 \times 0.635 \approx 0.33$ for the states in order of increasing energy. The compositions of the states involved are given in tables 5.3 and 5.4.

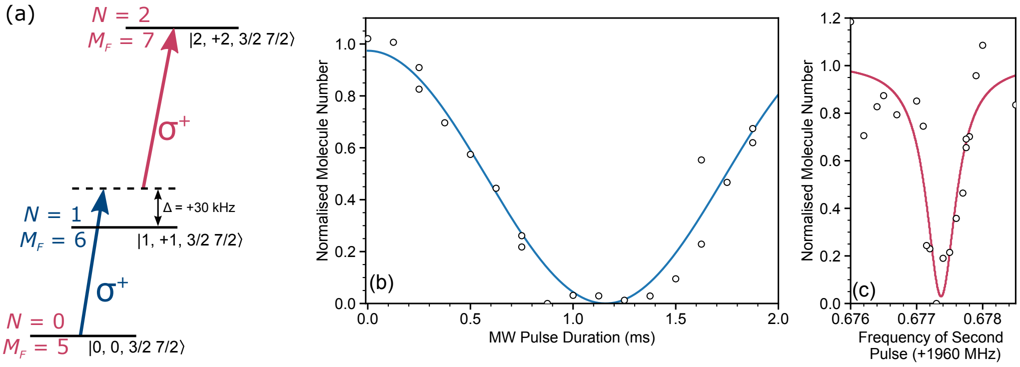

Figure 5.8: Two-photon transfer between the spin-stretched states of $N = 0$ and 2. (a) Scheme followed in the transfer. To avoid population build up in the intermediate $N = 1$ level, both microwaves are detuned by +30 kHz. The intensity in each frequency of microwaves is tuned such that both transitions are driven with a similar Rabi frequency when on resonance. (b) Observation of two-photon Rabi oscillations. At this microwave intensity, the Rabi frequency is much slower than is observed in one-photon transfer. We are therefore unable to observe a complete Rabi cycle in free-space as after ∼1 ms we begin to lose molecules during retrapping; the molecule number has been normalised to compensate for this loss in the fitting. The solid line is a cosine curve fitted to the results up to 1 ms. (c) Effect of scanning the second higher microwave frequency. A 'loss' of molecules is observed when on two-photon resonance due to molecules being transferred to the higher rotational state from which they can no longer be dissociated.

We can use a similar protocol to transfer molecules to the second rotationally excited state $N = 2$. The second microwave transition in this case has a frequency of $\sim$ 1960 MHz and is supplied using a microwave horn originally installed for spectroscopy of Rb atoms. Rabi oscillations between spin-stretched hyperfine states in $N = 0$ and 1, and $N = 1$ and 2 are shown in Fig. 5.7. We measure Rabi frequencies of $\Omega_{01}/2\pi = 5.05(5)$ kHz and $\Omega_{12}/2\pi = 3.55(4)$ kHz respectively. Fig. 5.7(d) shows the effect of scanning the frequency of the second microwave frequency with $t_{\text{pulse}} = t_{\pi}$, i.e. spectroscopy of a single hyperfine state in $N = 2$. The dashed vertical line shows the theory prediction for the centre frequency using the molecular constants fitted to the spectroscopy of $N = 1$. We find that the theory is able to predict the energy of this hyperfine state in $N = 2$ to < 1 kHz.

It is also possible to perform two-photon transfer of molecules in a single step by pulsing the two microwave frequencies on simultaneously. We investigate this approach for the spin-stretched state transfer to $N = 2$. To avoid population of the intermediate state we detune both beams to an energy 30 kHz above the intermediate state as shown in Fig. 5.8. The powers for each microwave frequency are tuned such that the on-resonance Rabi frequency for both transitions are similar and are around $\Omega/2\pi \approx 5$ kHz. Two-photon Rabi oscillations are observed with a Rabi frequency of $\Omega_{02}/2\pi = 0.40(1)$ kHz. Note, that the time required for a π pulse using these parameters is over 1 ms, and so in free-space we are unable to observe a complete Rabi cycle due to loss of molecules from the trap. Transfer by this method for a given microwave intensity is therefore significantly slower than the two-step approach shown in Fig. 5.6 and 5.7, this is due to the reduction in coupling strength when off-resonance from the narrow hyperfine transitions. This approach may be useful if population of an intermediate state is particularly undesirable. In particular, the superposition of states $N = 0$ and 2 have no associated dipole moment, whereas the superposition of either of those states with $N = 1$ does. In the case where dipole-dipole interactions are strong enough to affect microwave transfer, e.g. through blockade effects, complete population transfer between rotational states may only be possible using a single two-photon pulse.

Although π pulses offer one method of transferring the population between states, the transfer efficiency is limited by how well we can measure the required duration of a π pulse. In addition, the stability of the transfer over long timescales depends upon the reproducibility of the microwave intensity and external electromagnetic fields. In practice, such pulses are useful for producing superpositions of states as we will move on to discuss in the next section. However, when requiring as close to 100% transfer efficiency as possible (as is necessary when investigating lifetimes of molecules in a range of states) a more robust method may be to use adiabatic rapid passage (ARP). We are looking to implement this in the near future.

5.4 Superpositions of Molecule States

As no state with well-defined parity may possess a dipole moment, superpositions of opposite-parity rotational states are necessary to access the electric dipole moment of the molecule. Such a superposition can be easily achieved

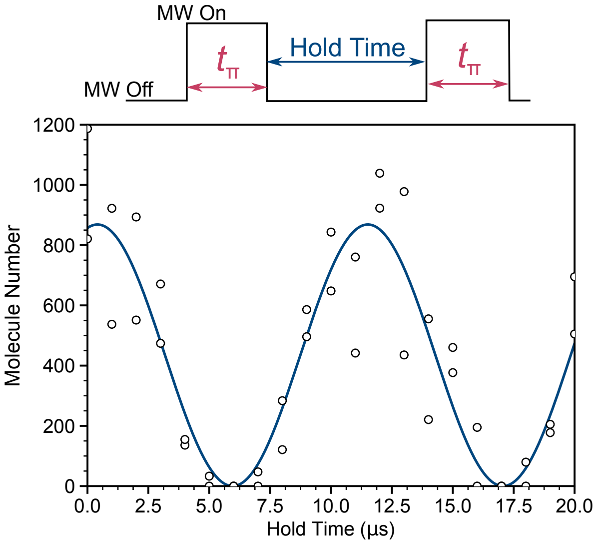

Figure 5.9: Oscillations observed in population when using a short high power microwave pulse to transfer molecules between $N = 0$ and $N = 1$. The duration of a π pulse $t_\pi = 3.29\,\mu\mathrm{s}$ which leads to a Fourier width much wider than the spacing between neighbouring hyperfine states.

using $\pi/2$ pulses to create 50:50 superpositions of the two states coupled by the microwaves. Such control leads to the possibility of using Ramsey interferometry as a sensitive probe to the collisional and dipolar processes undergone by the molecules.

In our experiment, we find that the production of superposition states limits the maximum speed at which we can transfer molecules between rotational states. Specifically, the maximum rate of transfer depends upon the proximity of neighbouring transitions to other hyperfine levels in the target rotational state. An example of this can be seen when trying to transfer molecules between $N = 0, M_F = 5$ and $N = 1, M_F = 4$. This uses a transition at 980.320 MHz, the same as that used in the first step of Fig. 5.6. Our initial attempt at this transfer was performed using high intensity microwaves which enabled a Rabi frequency of $\Omega_{01}/2\pi = 152(2)$ kHz, i.e. the duration of a single π pulse was $3.29\,\mu\mathrm{s}$. The Fourier width of this pulse is 304 kHz which is significantly larger than the spacing between neighbouring hyperfine states in $N = 1$ at this magnetic field. We therefore lose the ability to resolve the hyperfine structure, and the microwaves can couple to any hyperfine states which possesses appropriate values of M_F. This leads to a

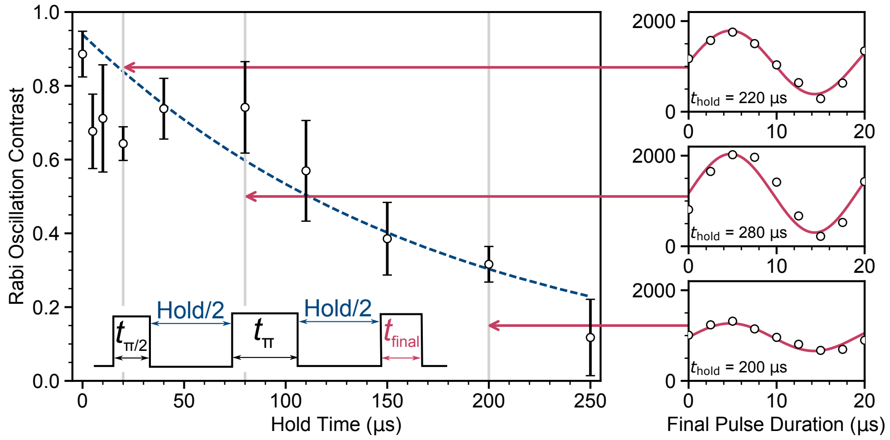

Figure 5.10: Contrast of Rabi oscillations driven between $N = 0$ and 1 against the hold time of the molecules in a superposition state. A spin-echo pulse sequence is used to reduce the effect of dephasing from the variable AC Stark shift across the 3D optical trap. The contrast of the Rabi oscillations is found by varying the duration of the final microwave pulse and fitting a sine wave to the result. The contrast is defined as the ratio of the amplitude to the number offset from zero of the fitted sine curve. The blue dashed line is an exponential fitted to the data with a time constant of 0.18(3) ms to be used as a guide to the eye.

production of a superposition of states. We demonstrate the production of a superposition by performing two π pulses with a variable hold time between them. This gives a hold time in $N = 1$ as shown in Fig. 5.9. We observe oscillations in the molecule population are observed at a rate of 90 kHz as a result of the superposition of states - comparable to the hyperfine splitting in the first rotationally excited state at $B \approx 180$ G.

We are also able to produce superposition states in a more controlled fashion by performing $\pi/2$ microwave pulses. Here we first present an initial measurement performed by preparing the molecules in a superposition of the two lowest energy $M_F = 5$ hyperfine levels of $N = 0$ and 1. Note, this preliminary work was performed with the molecules held in our optical dipole trap throughout the microwave pulse sequence; the effect of the dipole trap on the molecules will be discussed in detail in the next chapter. We perform a spin-echo pulse sequence on the molecules as shown in Fig. 5.10; this is a sequence which is designed to remove the dephasing caused by differential AC Stark shifts across the trap. We vary the duration of the final $\pi/2$ pulse and look at the contrast in the observed Rabi oscillations as a function of

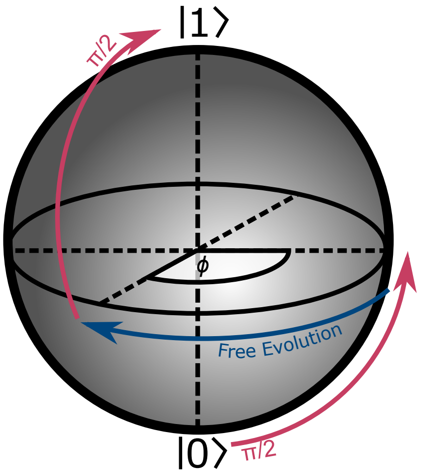

Figure 5.11: Bloch sphere representation of Ramsey spectroscopy. The molecules are placed into a superposition of two states using a $\pi/2$ microwave pulse. The phase of this superposition is allowed to freely evolve which corresponds to rotation around the equator of the bloch sphere, during which the superposition accumulates a phase ϕ. The second microwave pulse must have a phase offset from the first of ϕ for the molecules to be successfully transferred to the excited state as shown. Varying the phase of the second pulse allows inspection of the phase and coherence of the superposition state. Ramsey spectroscopy may also be performed by varying the frequency of the microwave pulses. In this case, the first $\pi/2$ pulse places molecules at a different latitude on the sphere, which leads to a variation on the rate of precession during free-evolution and subsequently maps the precession rate onto the molecule number. This method is demonstrated in Fig. 5.12.

hold time in the superposition state. We find that the coherence of the superposition appears to decay over around 180 µs. This is seemingly shorter than the coherence times previously observed in KRb molecules confined to a 3D optical lattice [74]. The cause of this is not clear. Dephasing rather than decoherence could be due to the motion of the molecules around the trap which the spin-echo pulse does not account for. However, we would expect this to operate on the timescale of the trap period which in this case is ∼1 ms. In addition, there appears to be some oscillatory behaviour, though this may be due to poor signal to noise at the time of running the experiment.

A better approach and the logical continuation to this measurement is to perform a Ramsey measurement where we can directly probe the free-evolution of the superposition phase. Ramsey interferometry may be performed by fixing the duration of both microwave pulses (such that they are each a $\pi/2$

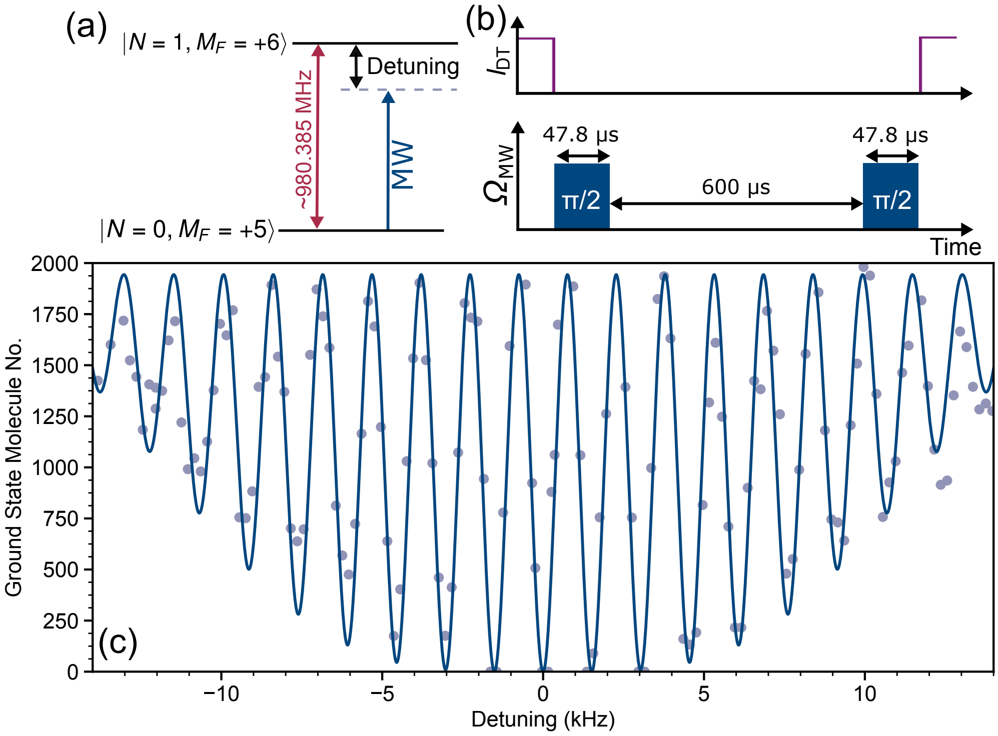

Figure 5.12: Ramsey interferometry between the two lowest hyperfine states of the $N = 0$ and $N = 1$ rotational levels of ^{87}Rb^{133}Cs in free-space. (a) The relevant hyperfine levels in ^{87}Rb^{133}Cs. We vary the detuning of the microwaves from the on-resonance transition frequency. (b) The relevant timings for the observation of kHz separated Ramsey fringes. The two microwave pulses are set such that they each drive a $\pi/2$ pulse when on resonance. The duration of 47.8 µs corresponds to a Rabi frequency of $\Omega/2\pi = 5.2(1)$ kHz. The pulses are separated by a free-space evolution time of 600 µs. (c) By varying the frequency of both microwave pulses, Ramsey fringes separated by ~ 1.5 kHz are observed. Each point is the result of a single run of the experiment, the solid blue line is a least-squares fit to the data using Eq. 5.1 with two free parameters: the centre frequency and the peak number of molecules.

pulse on-resonance with the transition) and subsequently varying either the phase or frequency of the second pulse. Either of these variables maps the phase of the superposition onto the final population of molecules in each state as shown in Fig. 5.11. We demonstrate this approach by varying the frequency of the microwave pulses. Note that this time the molecules are not recaptured in the dipole trap and the whole sequence is performed in free space. In the absence of the dipole trapping light there is little reduction in contrast of the Ramsey fringes even at hold times of up to 1400 µs. In

Fig. 5.12, we show a wide scan of the detuning away from the resonant frequency δ for a free-evolution time of $T = 600\,\mu\text{s}$. The spacing of the fringes observed is inversely proportional to the free-evolution time used, and the width of the envelope is inversely proportional to the duration of the $\pi/2$ pulses used, τ (i.e. the Fourier-limited width of the microwave pulses). We fit the number of remaining molecules N with [88]

$$N(\delta) = \frac{4\pi^2 \sin^2\left(\frac{X}{4}\right)}{X^4}\left[X\cos\left(\frac{X}{4}\right)\cos\left(\frac{\delta T}{2}\right) - 2\delta\tau\sin\left(\frac{X}{4}\right)\sin\left(\frac{\delta\tau}{2}\right)\right]^2, \tag{5.1}$$

where $X = \sqrt{\pi^2 + 4\delta^2\tau^2}$. Future experiments will likely look towards directly controlling the phase of the microwave pulses, as this removes the dependency of the feature spacings and widths on the pulse timings.

5.5 Summary

In summary, we have performed high-precision microwave spectroscopy of ultracold ^{87}Rb^{133}Cs molecules in the vibrational ground state, and have accurately determined the hyperfine coupling constants for the molecule. Our results confirm that the hyperfine coupling constants calculated by Aldegunde *et al.* [145] are generally accurate to within ±10%, calibrating the probable accuracy of the calculations for other alkali-metal dimers. The resulting understanding of the hyperfine structure enables full control of the quantum state, and we have demonstrated coherent transfer to a chosen hyperfine state in either the second-excited, first-excited or ground rotational state. Such complete control is essential for many proposed applications of ultracold polar molecules, and opens the door to a range of exciting future experimental directions, including studies of quantum magnetism [18, 22] and novel many-body phenomena [181, 182].

Chapter 6

Polarisability, Trapping, and the AC Stark Effect

Many of the applications for ultracold molecules rely on coherent microwave transfer between rotational states of optically trapped molecules. In the last chapter we developed the tools to perform microwave transfer between hyperfine and rotational states in free-space. Now we will investigate the effect of the trapping light on this transfer and on the hyperfine structure of the molecules.

All molecules that have been prepared at ultracold temperatures so far [26, 28–30, 32] have nuclei with non-zero spins, resulting in complex hyperfine and Zeeman structure [70, 145, 175, 177, 178, 183]. In such cases, the laser fields used to confine the molecules have important effects through the AC Stark effect, particularly for molecules in rotationally excited states. A thorough understanding of these effects is essential in order to eliminate differential Stark shifts detrimental to internal state transfer and thus to develop ultracold polar molecules into a controllable resource for use in quantum science.

The key quantity that determines the AC Stark effect is the molecular polarisability. Following a theoretical proposal by Kotochigova and DeMille [184], Neyenhuis *et al.* [176] have carried out parametric heating experiments at fixed laser intensity to determine the polarisabilities of different molecular states. They showed that there exists a *magic* angle for the linear polarisation of optical trapping light. In analogy with magic-wavelength traps in atomic systems, at the magic angle, the AC Stark shift of hyperfine levels of different rotational states are the same. This allowed Ramsey interferometry between two rotational levels of the molecule with a reasonably long coherence time, and led to a pivotal study of the dipolar spin-coherence time in a 3D optical lattice [74]. More recently, Deiß *et al.* [185, 186] have carried out parametric heating experiments on aligned triplet Rb_2 molecules and extracted both isotropic and anisotropic polarisabilities.

In this chapter, we explore the dependence of the AC Stark effect on laser intensity both experimentally and theoretically, using microwave spectroscopy of the chemically stable and bosonic $^{87}\mathrm{Rb}^{133}\mathrm{Cs}$ molecule. We begin by outlining the theory behind the AC Stark effect in ultracold molecules (6.1). We show that there is a subtle interplay between the AC Stark effect and the hyperfine structure. The trapping light couples neighbouring hyperfine states, giving rich and complex structure with many avoided crossings as a function of laser intensity. We use our measurements to extract a precise value for the anisotropic component of the molecular polarisability (6.2). We complete the characterization of the polarisability tensor by performing parametric heating and spectroscopic measurements to extract the isotropic component of the polarisability (6.3). We demonstrate how varying the polarisation of the trapping laser allows us to tune strength of avoided crossings between neighbouring hyperfine states (6.4). Our findings will allow us to engineer trapping potentials suitable for internal state transfer with long coherence times and have implications for experiments with other molecular species.

6.1 The AC Stark Effect in Molecules

The AC Stark effect arises from the interaction of the electric field due to a laser of intensity I with the polarisability α of an atom or molecule, and results in a perturbation in energy of $-\alpha I$. By contrast with the atomic case, the molecular polarisability is anisotropic; in the case of a linear diatomic molecule like $^{87}\mathrm{Rb}^{133}\mathrm{Cs}$, the highest polarisability is along the internuclear axis. We apply a magnetic field B_z in the vertical z direction, and the orientation of the molecule is defined with respect to this magnetic field.

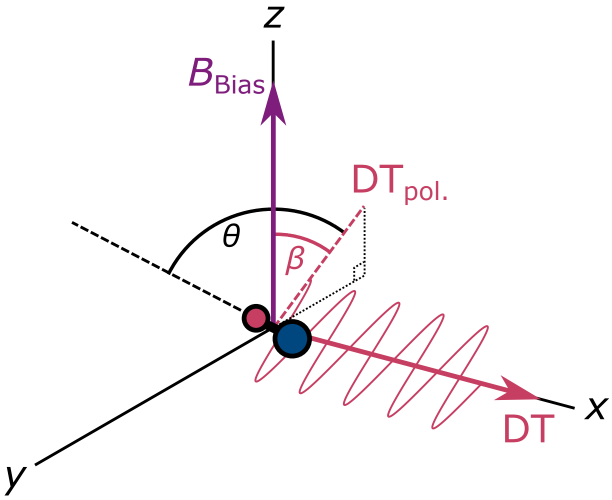

Figure 6.1: Coordinate system used in this work. A homogeneous magnetic bias field is applied in the vertical (z) direction. A single trapping beam (DT) propagates along the x axis and has polarisation defined with respect to the magnetic field by the angle β. The angle between the internuclear axis of the molecule and the laser polarisation is given by the angle θ. We apply microwaves polarised parallel to the z and y axes.

The polarisability of the molecule at an angle θ to the internuclear axis is

$$\begin{aligned}\alpha(\theta) &= \alpha_{\|}\cos^2\theta + \alpha_{\perp}\sin^2\theta \\ &= \alpha^{(0)} + \alpha^{(2)}P_2(\cos\theta),\end{aligned} \tag{6.1}$$

where $\alpha_{\|}$ and $\alpha_{\perp}$ are the polarisability parallel and perpendicular to the internuclear axis respectively, $\alpha^{(0)} = \frac{1}{3}(\alpha_{\|} + 2\alpha_{\perp})$ and $\alpha^{(2)} = \frac{2}{3}(\alpha_{\|} - \alpha_{\perp})$, and $P_2(\cos\theta)$ is the Legendre polynomial equivalent to $\frac{1}{2}(3\cos^2\theta - 1)$. The trapping light is linearly polarised in the xz plane at an angle β to the magnetic field. We therefore rotate the polarisability tensor through an angle β and find matrix elements

$$\begin{gathered}\langle N', M_N'|I\alpha|N, M_N\rangle = I\alpha^{(0)}\delta_{NN'}\delta_{M_N M_N'} \\ +I\alpha^{(2)}\sum_M d^2_{0M}(\beta)(-1)^{M_N'}\sqrt{(2N+1)(2N'+1)} \\ \begin{pmatrix} N' & 2 & N \\ 0 & 0 & 0 \end{pmatrix}\begin{pmatrix} N' & 2 & N \\ -M_N' & M & M_N \end{pmatrix},\end{gathered} \tag{6.2}$$

where N is the rotational angular momentum of the molecule, with projection M_N along the magnetic field axis, and $d^2(\beta)$ is a reduced rotation matrix.

To calculate the hyperfine levels in the presence of an AC Stark effect, we construct the Hamiltonian matrix in a decoupled basis $|NM_N\rangle|I_{\mathrm{Rb}}m_I^{\mathrm{Rb}}\rangle|I_{\mathrm{Cs}}m_I^{\mathrm{Cs}}\rangle$, where $I_{\mathrm{Rb}} = 3/2$, $I_{\mathrm{Cs}} = 7/2$ and m_I^{Rb}, m_I^{Cs} are the corresponding projections. We supplement the Zeeman and hyperfine matrix elements described in section 2.5.3 with the AC Stark terms of Eq. 6.2, which are diagonal in and independent of m_I^{Rb} and m_I^{Cs}. We include all basis functions with $N \leq 3$ in the calculation. Diagonalizing the resulting Hamiltonian gives us both energy levels and wavefunctions in the presence of off-resonant trapping light. We then use the wavefunctions to calculate spectroscopic transition strengths for the required polarisation of microwaves.

The representation in terms of $\alpha^{(0)}$ and $\alpha^{(2)}$ conveniently separates the effects of the two components of the polarisability. The isotropic component $\alpha^{(0)}$ shifts all diagonal matrix elements by the same amount and has no effect on transition frequencies, though it does contribute to optical trapping. The anisotropic component $\alpha^{(2)}$, on the other hand, mixes different hyperfine states through matrix elements diagonal and off-diagonal in M_N and dependent on β. For $N = 0$, the matrix elements of $\alpha^{(2)}$ are zero, so the polarisability is simply $\alpha^{(0)}$ for all hyperfine states. For $N = 1$, however, $\alpha^{(2)}$ has important effects; if we neglect terms off-diagonal in N, the matrix of the polarisability tensor between basis functions with $N = 1$, $M_N = 0$, $+1$ and -1 is

$$\langle 1, M_N'|I\alpha|1, M_N\rangle = I\alpha^{(0)}+ \\ \frac{I\alpha^{(2)}}{5}\begin{pmatrix} 2P_2(\cos\beta) & -\frac{3}{\sqrt{2}}\sin\beta\cos\beta & +\frac{3}{\sqrt{2}}\sin\beta\cos\beta \\ -\frac{3}{\sqrt{2}}\sin\beta\cos\beta & -P_2(\cos\beta) & \frac{3}{2}\sin^2\beta \\ +\frac{3}{\sqrt{2}}\sin\beta\cos\beta & \frac{3}{2}\sin^2\beta & -P_2(\cos\beta) \end{pmatrix}. \tag{6.3}$$

In the absence of the trapping laser, $M_F = M_N + m_I^{\mathrm{Rb}} + m_I^{\mathrm{Cs}}$ is a good quantum number, but M_N, m_I^{Rb} and m_I^{Cs} are not individually conserved. When the trap laser is polarised along B_z, corresponding to $\beta = 0$, M_F is still conserved. However, when $\beta \neq 0$, the AC Stark effect mixes levels with different values of M_F and there are no good quantum numbers.

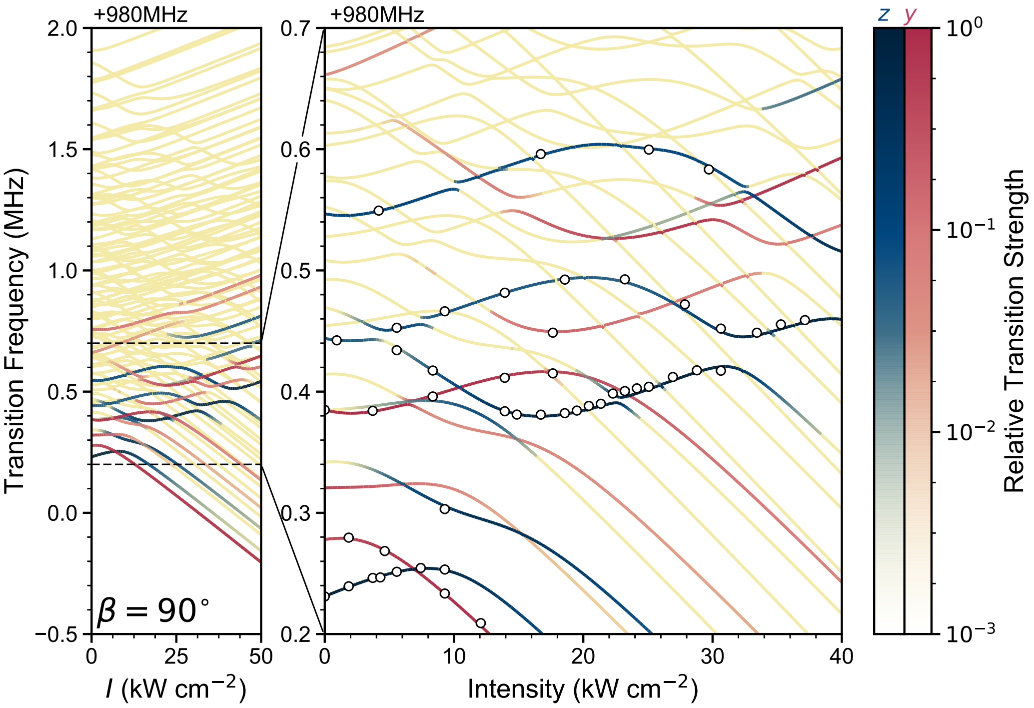

Figure 6.2: Transition frequencies from the lowest energy hyperfine level of the rovibronic ground state $N = 0, M_F = 5$ to the 96 hyperfine states for $N = 1$ as a function of laser intensity, for laser polarisation perpendicular to the magnetic field, $\beta = 90°$. The relative transition strengths for microwaves polarised along z and y and are shown as blue and red color maps respectively. The data points show experimental microwave frequencies. The magnitude of the applied magnetic field is $B = 181.5$ G.

6.2 Anisotropic Component of Polarisability $\alpha^{(2)}$

The differential AC Stark shift between $N = 0$ and $N = 1$ gives a direct measurement of the anisotropic component of the polarisability. To measure this, we perform microwave spectroscopy (see Chapter 5) in the presence of the dipole trapping light. A single beam ($\lambda = 1550$ nm, waist $= 95$ μm) is switched on for 500 μs before the microwave pulse to allow the intensity of the trapping light to stabilize. The laser polarisation is tunable to a precision of ±1° by a $\lambda/2$ waveplate. The molecules experience a reasonably homogeneous laser intensity within 2% of the peak intensity. With the molecules initially in the spin-stretched rotational and hyperfine ground state ($N = 0, M_N = 0, m_I^{\mathrm{Rb}} = 3/2, m_I^{\mathrm{Cs}} = 7/2$), we pulse on the microwave field for a time (t_{pulse}) that is less than the duration of a π pulse for the relevant transition. We measure the number of molecules remaining in the

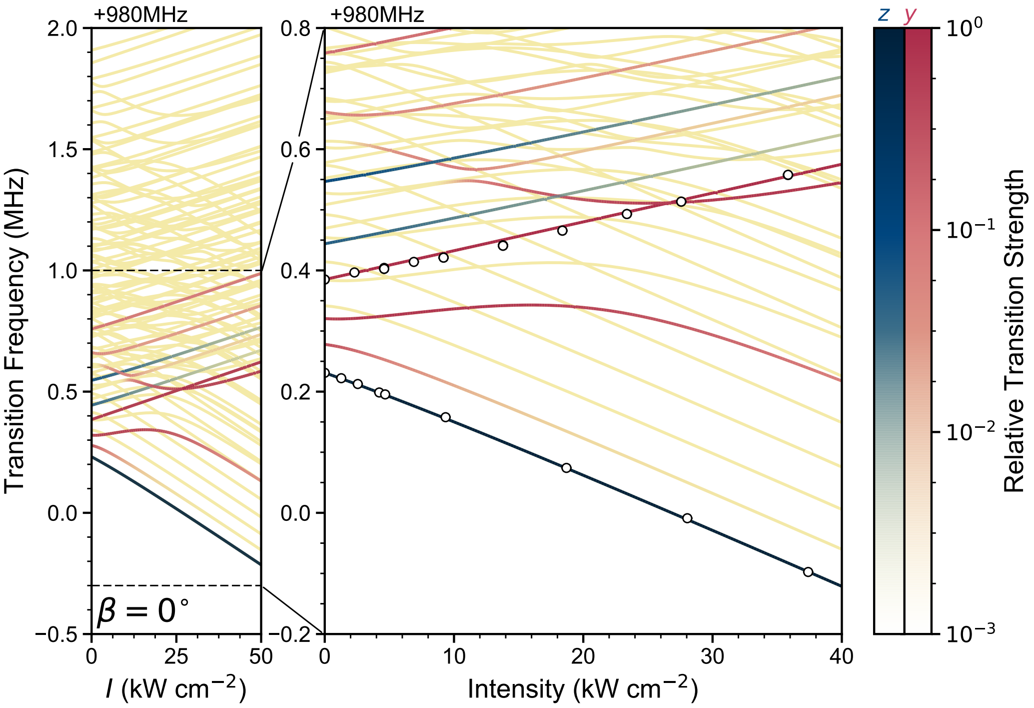

Figure 6.3: Transition frequencies from $N = 0, M_F = 5$ to $N = 1$ as a function of laser intensity, for laser polarisation parallel to the magnetic field, $\beta = 0°$. The relative transition strengths are coded as in Fig. 6.2. The data points show experimental microwave frequencies. The magnitude of the applied magnetic field is $B = 181.5$ G.

ground state by reversing the STIRAP sequence to dissociate the molecules and using absorption imaging to detect the resulting atoms. We observe the microwave transition as an apparent loss of ground-state molecules. The widths of all features we measure are Fourier-transform limited, i.e. the width is proportional to $1/t_{\text{pulse}}$. The microwave power is tuned to allow pulse times of 100-180 μs, yielding Lorentzian lines with 5-10 kHz full width at half maximum. We observe transitions due to microwaves polarised along the z and y axes, when the dipole trap is off these correspond to π and $\sigma^\pm$ polarisations respectively.

We begin by setting the laser polarisation perpendicular to the magnetic field, i.e. $\beta = 90°$. Fig. 6.2 shows the measured transition frequencies for $B_z = 181.5\,$G as a function of laser intensity. These are superimposed on calculations of the 96 hyperfine levels of $N = 1$, using molecular constants fitted to the experiments as described below. Calculated transition strengths are shown for microwaves polarised along z (blue) and y (red). Many avoided crossings appear in the region where $I\alpha^{(2)}$ is comparable to the hyperfine couplings and Zeeman splittings. The basis functions that carry the spectroscopic intensity cut through the manifold of states, resulting in a complicated variation in transition strengths as each state brightens and fades. At sufficiently high laser intensities, the AC Stark effect dominates the Zeeman splittings; N eventually requantizes along the laser polarisation axis, and the pattern of transition strengths and frequencies simplifies.

Fig. 6.3 shows analogous results for laser polarisation parallel to the applied magnetic field, $\beta = 0°$. A single beam is used at low intensities, as in Fig. 6.2. At the highest intensities shown, however, two beams are used to form a crossed optical dipole trap. The beams propagate in the xy plane and cross at an angle of $\sim 27°$. In this case M_F is a good quantum number even in the presence of the trapping laser. The three $M_F = 5$ hyperfine states for $N = 1$ (blue) diverge as a function of laser intensity, and there are no avoided crossings between them. At high intensity M_N becomes an increasingly good quantum number, and the two states with $M_N = \pm 1$ lose intensity for microwaves polarised along z. Nevertheless, strong avoided crossings still exist where states with the same M_F cross.

The experimental uncertainties are not visible on the scale presented in Figs. 6.2 and 6.3. The statistical uncertainties in the transition frequencies are typically ±0.5 kHz. The dominant uncertainty in the laser intensity on the other hand is systematic and due to the uncertainty in the beam waist at the position of the molecules. We estimate this uncertainty to be ±3% of the peak intensity.

We have fitted the experimental results of Figs. 6.2 and 6.3 independently to obtain $\alpha^{(2)}$, while holding the hyperfine constants fixed at the values of ref. [178]. For laser polarisation $\beta = 0°$ and 90°, we obtain values of $\alpha^{(2)}_{\beta=0°}/4\pi\epsilon_0 = 507(1)\,a_0^3$ and $\alpha^{(2)}_{\beta=90°}/4\pi\epsilon_0 = 602(2)\,a_0^3$ respectively. The uncertainties given are the statistical uncertainties found during fitting, but both results are subject to the same systematic uncertainty in intensity described above. The difference between the two fitted values of $\alpha^{(2)}$ is not understood; it is not due to hyperpolarisabilty effects or to uncertainties in the molecular hyperfine constants. Nevertheless, despite the difference between the two fitted values, the theory in each individual case describes the observed AC Stark shift well.

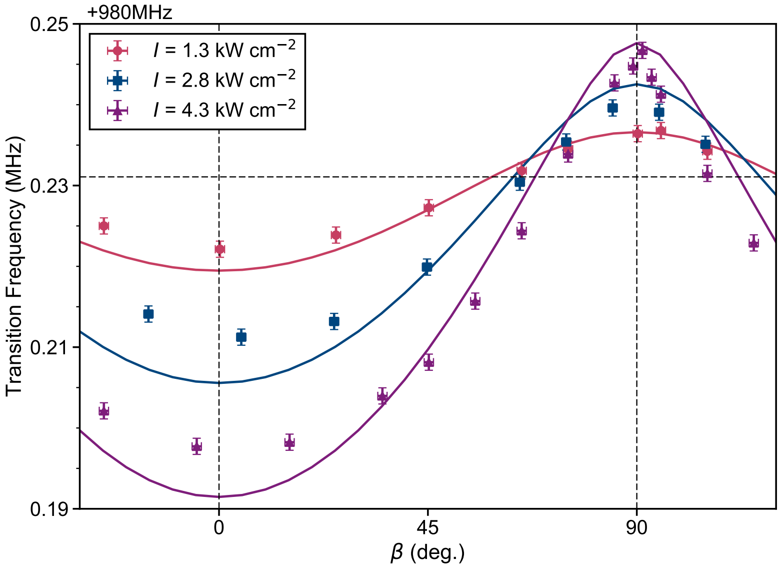

Figure 6.4: AC Stark shift of the transition to the lowest energy hyperfine level of $N = 1$ with varying laser polarisation β. Squares show experimentally measured transition frequencies at intensities of 1.3 kW cm^{-2}, 2.8 kW cm^{-2} and 4.3 kW cm^{-2} in the single beam trap. The solid lines are the theory prediction using the value of $\alpha^{(2)}$ found in the $\beta = 90°$ case shown in Fig. 6.2. The horizontal dashed line shows the frequency of the transition when measured in free space.

To more closely examine the dependence of the AC Stark shift on the laser polarisation, we fix the single beam laser intensity and vary β. Fig. 6.4 shows the AC Stark shift of transition to the lowest energy hyperfine level of $N = 1$ for three intensities in the single beam trap. All three intensities used are relatively weak such that the overall shift is smaller than the spacing between neighbouring hyperfine levels. The theory lines in Fig. 6.4 are calculated using the $\alpha^{(2)}$ fitted to the $\beta = 90°$ result shown in Fig. 6.2, as such they systematically predict a larger AC Stark shift than we observe in the experiment when at $\beta = 0°$. This result corroborates the conclusion that there is some unexpected dependency on β which our model does not include. The horizontal dashed line shows the transition frequency when measured in free space. The angle at which our measured AC Stark shift crosses this frequency depends strongly upon intensity; this crossing point is therefore not an indication of a magic laser polarisation angle.

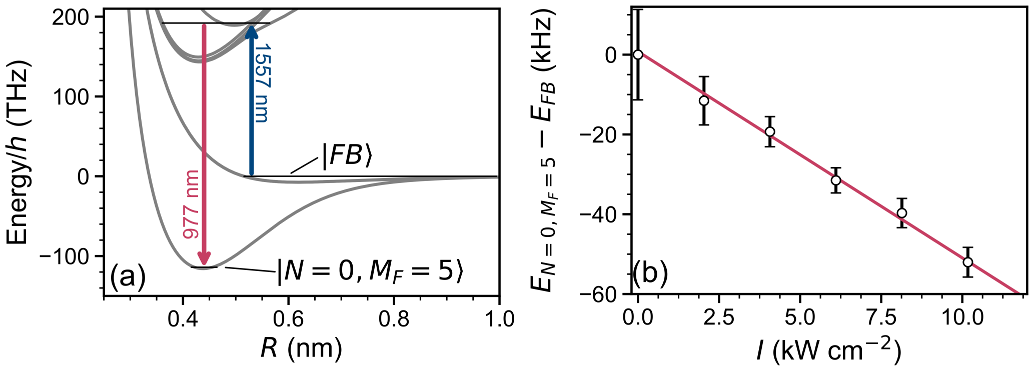

Figure 6.5: Measurement of the isotropic component $\alpha^{(0)}$ with spectroscopy. (a) Transitions used in STIRAP of molecules to the lowest hyperfine sublevel of the rovibronic ground state. (b) AC Stark shift of the STIRAP dark-state resonance.

6.3 Isotropic Component of Polarisability $\alpha^{(0)}$

To characterize the polarisability of the molecule fully, we must also measure the *isotropic* component $\alpha^{(0)}$. To do this, we perform several complementary measurements. First, we observe the energy shift of $N = 0$, $M_F = 5$ with respect to an initial weakly bound Feshbach state. This is given by the AC Stark shift of the two-photon transition used in STIRAP [140], shown in Fig. 6.5. This energy shift gives the difference in polarisability between the two molecular states, and the polarisability of the Feshbach state is simply the sum of the polarisabilities of the constituent atoms, which are well known [187]. Note that we have also used this method to determine the trap frequency experienced by atoms in the lowest hyperfine sublevel of $N = 1$ when $\beta = 0°$. This was reported in [188], and by compensating for the known value of $\alpha^{(2)}$ we find the same value for the isotropic component within our experimental uncertainty using either rotational state.

In addition to this spectroscopic method, we perform parametric heating on the molecular sample. Here, we retrap $N = 0$ molecules in their lowest hyperfine state with two beams with $\beta = 0°$ and total intensity $I = 36$ kW cm^{-2}. The intensity of one of the beams is then modulated sinusoidally by $\pm 20\%$ for 1 s. When the modulation frequency is twice the trapping frequency, we resonantly heat the molecules and observe evaporative loss from the trap as shown in Fig. 6.6. If the AC Stark shift is linear, the trap frequency ω

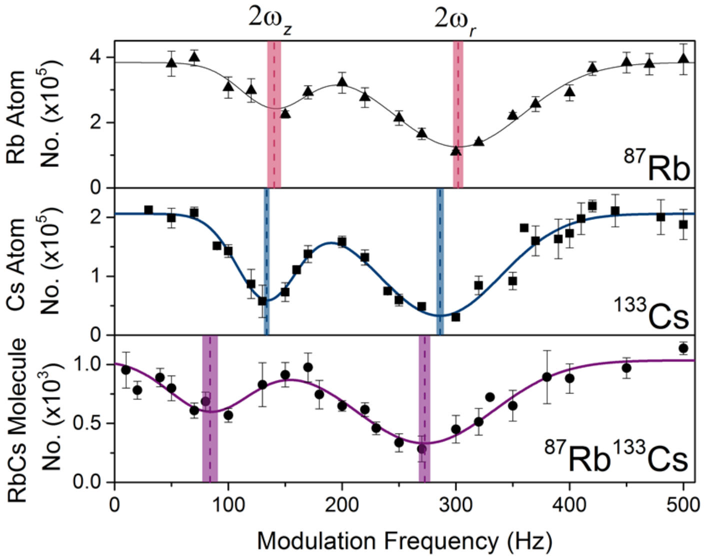

Figure 6.6: Measurement of the isotropic component $\alpha^{(0)}$ through parametric heating. Parametric heating measurements of trap frequency experienced by molecules in the lowest-energy hyperfine state of $N = 0$, and ^{87}Rb and ^{133}Cs ground state atoms in traps with the same peak laser intensity. The dotted lines and shaded regions show the fitted trap frequencies and uncertainties, respectively, for each data set.

is proportional to $\sqrt{\alpha/m}$, where m is the mass. We compare the trap frequency for molecules with those for ^{87}Rb and ^{133}Cs atoms in a dipole trap of the same intensity in Fig. 6.6 to find the absolute polarisabilities of the molecules in both states. We find $\alpha^{(0)}/4\pi\epsilon_0 = 8.8(1) \times 10^2\ a_0^3$, in reasonable agreement with theoretical predictions [184, 189, 190]. Note that the parametric heating approach does not require knowledge of the absolute intensity of the trapping beams and thus gives a smaller uncertainty in $\alpha^{(0)}$.

6.4 Tuning Avoided Crossings and Experimental Considerations

The avoided crossings between laser-dressed levels can cause trap loss if the molecules undergo Landau-Zener transitions to different hyperfine states as they move around the trap, or if the intensity of the dipole trap is changed dynamically. This is particularly important when retrapping molecules that have been manipulated in free space. Since in our experiment trapping re-

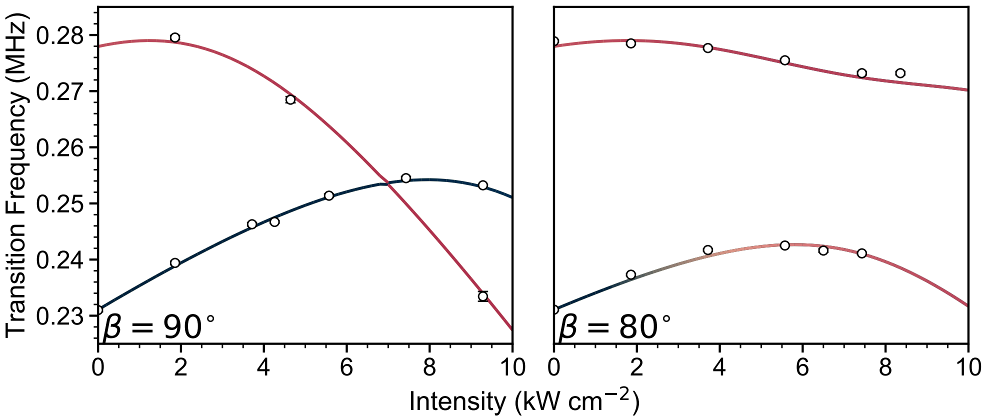

Figure 6.7: Transition frequencies from $N = 0, M_F = 5$ to the two lowest energy hyperfine states of $N = 1$ for $\beta = 90°$ and $80°$. Transition strengths are coded as in Figs. 6.2 and 6.3.

quires a minimum laser intensity around 15 kW cm^{-2}, such losses occur for example when attempting to retrap the spin-stretched $N = 1, M_F = 6$ state with $\beta = 90°$. Avoided crossings will also produce anharmonic and anisotropic trapping potentials, which may result in complicated density profiles for molecular clouds and cause coupling between translational and rotational degrees of freedom in optical lattices. The strengths of avoided crossings may be tuned by varying β; for example, Fig. 6.7 shows how the avoided crossing between the two lowest energy hyperfine levels of $N = 1$ varies due to a 10° change in laser polarisation. Understanding the avoided crossings will allow us to identify optimum laser intensities and polarisations for optical trapping. Furthermore, given sufficient broadening of the avoided crossing and precise control of the laser intensity, it may be possible to traverse the avoided crossings in a controlled manner during the retrapping of molecules. This may allow access to hyperfine states that are not easily produced with microwave transfer.

A further consequence of the AC Stark effect is that the frequencies of microwave transitions depend on the position within an optical trap. This has important ramifications for the design of experiments to achieve coherent control of trapped molecules. Neyenhuis *et al.* demonstrated coherence times in Ramsey interferometry up to 1.5 ms in ^{40}K^{87}Rb by optimizing a "magic angle" between the magnetic field and the laser polarisation [176]. To achieve longer coherence times, it is desirable to find excited states that

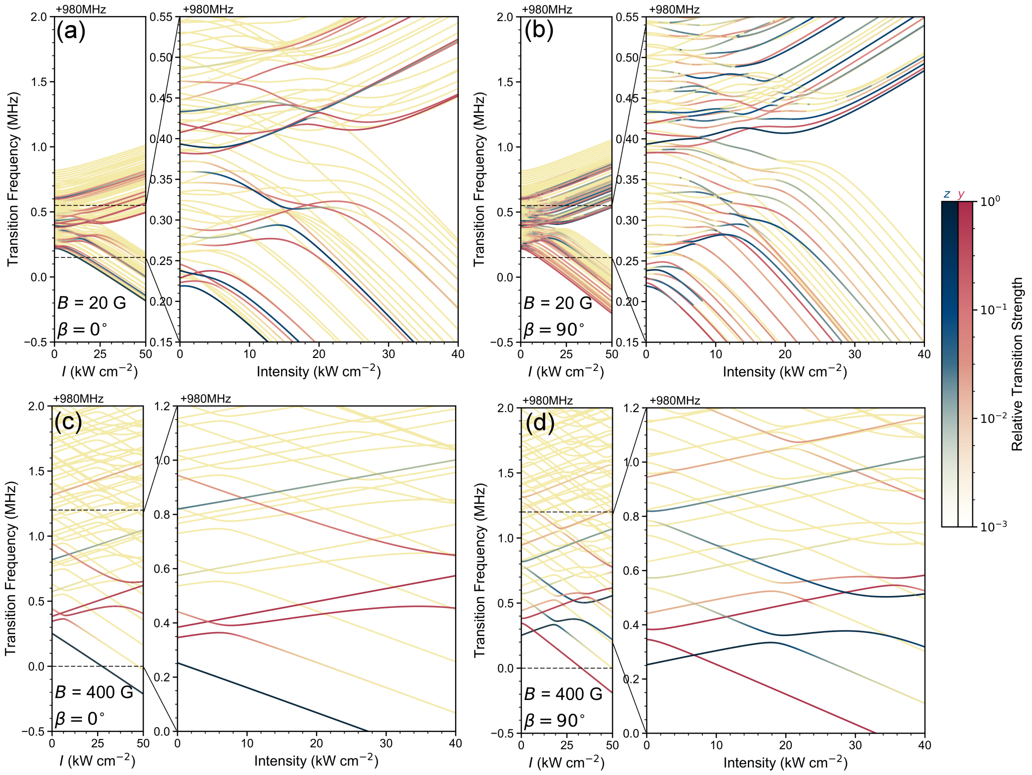

Figure 6.8: Effect of varying the magnetic field on the AC Stark shift in the first rotationally excited state. The AC Stark shift for the transition from $N = 0, M_F = 5$ to the various hyperfine states of $N = 1$ is shown for experimental parameters (a) $B = 20$ G, $\beta = 0^\circ$, (b) $B = 20$ G, $\beta = 90^\circ$, (c) $B = 400$ G, $\beta = 0^\circ$, (d) $B = 400$ G, $\beta = 90^\circ$. At low dipole trap intensities, the structure of avoided crossings is somewhat simplified at higher magnetic fields due to the larger Zeeman separation of the hyperfine states. However, low magnetic fields may sometimes be beneficial as the AC electric field of the off-resonant trapping light dominates the behaviour at lower intensities.

are parallel to the ground state as a function of laser intensity. This condition is met at the turning point of an avoided crossing. This will make it possible to achieve longer coherence times by controlling laser intensity as well as polarisation. A specific example of such magic conditions can be seen in Fig. 6.3. The red $M_F = 4$ hyperfine state with transition frequency $\sim$ 980.32 MHz in free space shows a very broad turning point at around 20 kW cm^{-2}. When trapping close to this turning point, the transition frequency is relatively insensitive to variations in the intensity of the trapping light, i.e. the variable AC Stark shift across the cloud is minimised, which should lead to long coherence times.

An additional parameter which may be tuned is the magnitude of the applied magnetic field. The effect of changing the magnetic field is shown in Fig. 6.8. At low magnetic fields, the dipole trap dominates at correspondingly lower trapping intensities. In this case, trapping the molecules at intensities over $\sim$ 20 kW cm^{-2} is greatly simplified. However, the small initial Zeeman splitting of the states makes navigating the structure of avoided crossings in the lowest intensity regions far more difficult. Retrapping of molecules would be further complicated by working at lower magnetic fields, as the number of available avoided crossings is greater. Increasing the magnetic field on the other hand increases the Zeeman splitting between hyperfine states. This simplifies the structure in the regions between 0 and 20 kW cm^{-2}, and is clearly preferential for retrapping of molecules. However, creating deeper traps for the molecules, i.e. working at higher intensity, would require a similar increase in the magnetic field to ensure that the magnetic field continues to dominate over the AC electric field of the off-resonant trapping light. These plots indicate that changing the magnetic field is a powerful tool in controlling the structure of rotationally excited molecules. In the future, we plan to also look at the effect of DC electric fields. The strong coupling of the molecules electric dipole moment to the DC electric field should dominate over both the magnetic field and trapping light and could be used to further control the behaviour of the molecular structure.

6.5 Summary

In summary, we have completely characterized the anisotropic polarisability of ^{87}Rb^{133}Cs for $\lambda = 1550$ nm. We have measured microwave spectra of several hyperfine components of the $N = 0 \rightarrow 1$ microwave transition as a function of laser intensity and used them to extract precise values of the anisotropic component $\alpha^{(2)}$ of the molecular polarisability. We have supplemented this with parametric heating and spectroscopic measurements to determine the isotropic component $\alpha^{(0)}$. We have discovered a subtle interplay between the AC Stark effect and the hyperfine structure, which produces a rich and complex pattern of avoided crossings between levels as a function of laser intensity and polarisation. Understanding this pattern has allowed us to trap molecules in well-defined hyperfine states and control their polarisability. This lays the foundations for enhanced coherent microwave control of the internal state of polar molecules confined in optical traps and lattices, which will underpin many exciting proposed applications of ultracold molecules.

Chapter 7

Lifetimes and Collisions of Ultracold Molecules

The earliest works studying collisions of heteronuclear molecules in the ultracold regime were conducted with fermionic ^{40}K^{87}Rb molecules at JILA [26, 68, 71, 191]. As this molecule is chemically unstable to the atom exchange reaction 2KRb $\rightarrow$ K_2 + Rb_2 [69], the lifetime of the molecules was limited to 200(40) ms [71] in a 3D optical dipole trap. However, recent works have reported loss even in systems of chemically stable molecules [28, 30, 32]. Although such loss can be suppressed by confining the molecules to a 3D optical lattice [73], the mechanism of the loss is still unknown and is a hot topic in the field of ultracold molecules.

In this chapter we will study the lifetime of ^{87}Rb^{133}Cs molecules in our 3D optical dipole trap. We begin by reviewing the types of collisions which can exist in an ultracold quantum gas (7.1), and in particular we will look at the possible mechanism of 'sticky collisions' in systems of ultracold molecules (7.1.1). We will then look at experimental results from our experiment, examining the lifetime of the molecules as a function of dipole trap intensity (7.2.1), magnetic field (7.2.2), and hyperfine and rotational state (7.2.3). Finally we will discuss a future proposal for our experiment - to study collisions between atoms and molecules (7.3).

7.1 Collision Processes Between Ultracold Molecules

Lossy collision processes undergone in an ultracold gas can be categorised as either one-, two- or three-body in nature, and whichever of these is dominant dictates the rate at which molecules are lost from the trap. A one-body collision for example, could either be a collision of a molecule with an untrapped atom or molecule from the background gas, or due to absorption of a photon from the optical trapping light. Such collisions cause an exponential decay of the number of trapped molecules

$$\dot{N}_{\mathrm{mol}} = -\frac{N_{\mathrm{mol}}}{\tau}, \tag{7.1}$$

where the trap lifetime τ is typically on the order of minutes in ultra-high vacuum systems. Two-body and three-body collisions on the other hand rely upon the collision between optically trapped molecules.

Two-body collisions can lead to loss in a number of different ways. In the case of chemically reactive species like $^{40}\mathrm{K}^{87}\mathrm{Rb}$, dimers are lost as trimers and single atoms are produced in the trap. For chemically stable molecules however, loss may be observed due to dipolar spin relaxation as colliding molecules exchange angular momentum and are scattered into an undetected hyperfine state. The rate for two-body loss increases with density and so molecules are lost preferentially from the densest regions. This leads to 'anti-evaporation' and results in heating of the remaining sample as each molecule lost takes away on average, $\frac{9}{4}k_{\mathrm{B}}T$ of energy (see Appendix A) - less than the average thermal energy of the cloud. Two-body loss occurs with a characteristic heating and loss rate K_2 as

$$\begin{aligned} \dot{N}_{\mathrm{mol}} &= -\frac{K_2}{2^{3/2}}\left(\frac{m\bar{\omega}^2}{2\pi k_{\mathrm{B}}}\right)^{3/2}\frac{N_{\mathrm{mol}}^2}{T^{3/2}}, \\ \dot{T} &= \frac{K_2}{2^{3/2}}\left(\frac{m\bar{\omega}^2}{2\pi k_{\mathrm{B}}}\right)^{3/2}\frac{N_{\mathrm{mol}}}{T^{1/2}}, \end{aligned} \tag{7.2}$$

where m is the molecule mass and $\bar{\omega}$ is the geometrically averaged trap frequency. There is a special case for the two-body loss rate when there is unity probability of loss during a collision [192–194]. This is known as 'universal loss' and is the case for chemically reactive species [70, 192]. This special case puts an upper bound on the observable value of K_2. The universal loss rate depends only on the quantum scattering by the long range potential at distances greater than the van der Waals length. For identical bosons, the rate is given by

$$K_{\text{Univ.}} = \frac{16\pi\hbar}{m}\bar{a}. \tag{7.3}$$

Here, $\bar{a}$ is the characteristic van der Waals length

$$\bar{a} \approx 0.47799 \left(\frac{mC_6}{\hbar^2}\right)^{1/4}, \tag{7.4}$$

which in turn depends upon C_6 [193]. For most species (including ^{87}Rb^{133}Cs), the rotational dipole component dominates the value of C_6, and so [19]

$$C_6 \approx C_6^{\text{rot.}} = \frac{d_0^4}{6B_v}, \tag{7.5}$$

i.e. the universal loss rate depends mainly upon the molecule frame dipole moment d_0, rotational constant B_v, the mass of the scattering molecules m, and whether the molecule is a boson or a fermion. The universal loss rate for ^{87}Rb^{133}Cs is predicted to be $\sim 10^{-10}$ cm^3 s^{-1} in the absence of a DC electric field [193].

In the case of three molecules colliding, even 'chemically stable' molecules such as ^{87}Rb^{133}Cs may still be reactive. As such, molecules can be lost from the sample as quads, trimers, homonuclear dimers, and single atoms are created during the collision. However, as such a collision requires three molecules to be sufficiently close together, three-body collisions have a stronger dependence on density than two-body collisions. This process therefore results in greater heating of the remaining molecules as each lost molecule only carries away on average, $2k_{\text{B}}T$ of energy (see Appendix A). Three-body loss occurs with a characteristic heating and loss rate K_3 as

$$\begin{aligned} \dot{N}_{\text{mol}} &= -\frac{K_3}{\sqrt{27}}\left(\frac{m\bar{\omega}^2}{2\pi k_{\text{B}}}\right)^3 \frac{N_{\text{mol}}^3}{T^3}, \\ \dot{T} &= \frac{K_3}{\sqrt{27}}\left(\frac{m\bar{\omega}^2}{2\pi k_{\text{B}}}\right)^3 \frac{N_{\text{mol}}^2}{T^3}\frac{(T+T_{\text{h}})}{3}, \end{aligned} \tag{7.6}$$

where T_h is the recombination heating associated with the loss [195]. This process usually only plays a minor role for uncondensed clouds. As an example, for ^{87}Rb atoms in their lowest hyperfine state, the measured three-body

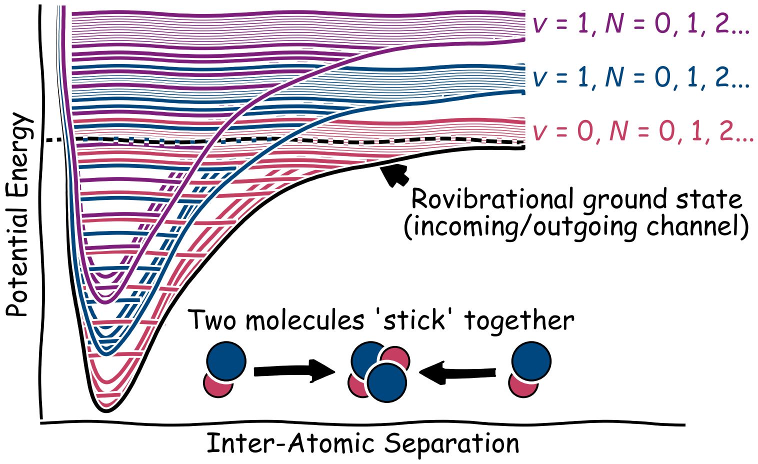

Figure 7.1: Cartoon (not to scale) illustrating the origin of sticky collisions. Molecules colliding in their rovibrational ground state experience a very high density of states in the 4 atom collision complex, this leads them to become 'stuck' together for some time. Figure adapted from [197]

loss rate is $K_3 = 4 \times 10^{-29}$ cm^6 s^{-1} [196]. For peak densities less than $\sim 10^{13}$ cm^{-3}, this translates to a decay rate of less than 1 atom per minute.

7.1.1 Sticky Collisions

The addition of rotational and vibrational degrees of freedom logically leads to a far higher density of Feshbach resonances in molecules than in comparable atomic systems. Collisions between two relatively heavy molecules may have such a high density of resonant states in fact, that tens of vibrational levels and hundreds of rotational levels may be energetically accessible [197]. This leads to a big unanswered question as to whether it could be possible to experimentally resolve the individual resonances.

Theoretical work by Prof. John Bohn's group at JILA relies on the assumption that individual resonances between ^{87}Rb^{133}Cs molecules cannot be resolved. As a result, a statistical approach may be taken as all observables become averaged over many resonances whose average spacing is dictated by the density of states [197, 198]. This method allows the system to effectively be described using non-resonant scattering calculations. In ^{87}Rb^{133}Cs, the extremely narrow resonances in the rovibrational ground state lead to long-lived two-molecule collision complexes. This leads to so-called 'sticky' collisions where two colliding molecules remain associated with each other for some time as their collision complex explores the high density of rotational and vibrational states energetically available to them [199]. The lifetimes of these collision complexes γ is hard to estimate, but may be on a timescale relevant to experiments [198, 200]. This is particularly important as molecules which occupy these collision complexes would be hidden from our hyperfine-state selective imaging techniques, and would appear to be lost from the experiment. In addition, as the collision complex is long-lived, a third molecule may collide with the complex. This delayed three-body collision process could lead to an enhancement of the energetically allowed three-body chemical reactions or to molecules being ejected from the trap. The number of 'free' molecules and collision complexes remaining in the sample can be modelled by the coupled rate equations

$$\begin{aligned}\dot{N}_{\mathrm{mol}} &= -\left(\frac{m\bar{\omega}^2}{4\pi k_{\mathrm{B}}T}\right)^{3/2}\left(N_{\mathrm{mol}}^2 K_{\mathrm{mm}} + N_{\mathrm{mol}}N_{\mathrm{com}}K_{\mathrm{mc}}\right) + 2\gamma N_{\mathrm{com}},\\ \dot{N}_{\mathrm{com}} &= +\left(\frac{m\bar{\omega}^2}{4\pi k_{\mathrm{B}}T}\right)^{3/2}\left(\frac{1}{2}N_{\mathrm{mol}}^2 K_{\mathrm{mm}} - N_{\mathrm{mol}}N_{\mathrm{com}}K_{\mathrm{mc}}\right) - \gamma N_{\mathrm{com}}.\end{aligned} \tag{7.7}$$

Here, K_{mm} and K_{mc} are the molecule-molecule and molecule-complex two-body rate coefficients respectively; the molecule-molecule rate constant must be summed over all available partial waves L, M_L. Each of the rate equations has three components. The first, proportional to N_{mol}^2, is a two-body process which gives the rate of production of collision complexes as pairs of molecules collide with each other. The second, proportional to $N_{\mathrm{mol}}N_{\mathrm{com}}$, is a second two-body process which gives the rate at which those collision complexes collide with the remaining molecules, after which both the complex and the 'free' molecule are removed from the sample. The final component, proportional to N_{com}, is a one-body decay process of the collision complexes dissociating back to free molecules.

The time dependence of loss from sticky collisions depends on all three components K_{mm}, K_{mc} and γ, and the ratio between these coefficients may determine how similar this loss mechanism appears to a generic two-body loss process. Discerning 'sticky' collisions from another loss process is difficult;

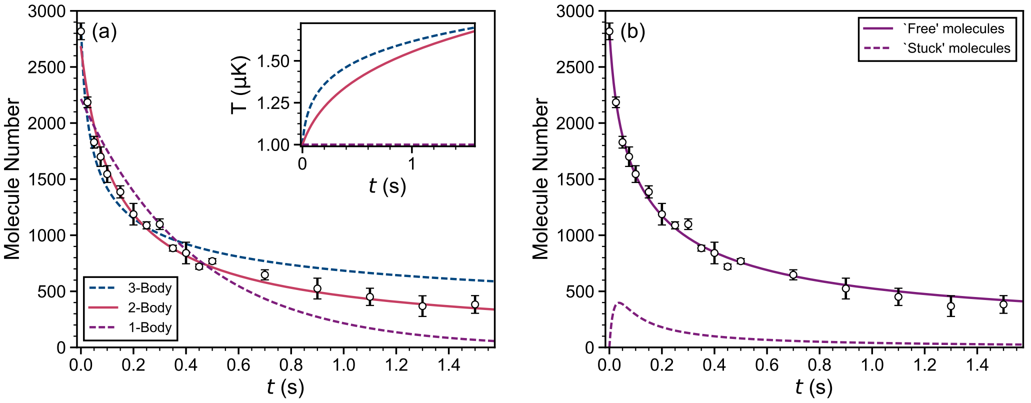

Figure 7.2: Example lifetime results for molecules in the rovibronic and hyperfine ground state. Each experimental data point is an average of at least three experimental measurements, higher averaging is likely required for meaningful statistics on fitted rate constants. The initial peak density of the sample is $\sim 1.4 \times 10^{11}$ cm^{-3}. (a) Fitting of the results as one-, two- and three- body loss as described in section 7.1. This result appears to fit best to a two-body loss curve though the difference between two-body and three-body are not statistically significant given our current signal to noise. Relevant rate coefficients are given in the main text. The inset shows the evolution of temperature; in our experiment we can only measure the initial temperature of the molecules. (b) Fitting of the results using the rate equations for 'sticky' collisions as given in Eq. 7.7. The number of molecules available for imaging is plotted as the solid line while the dashed line shows those molecules 'stuck' in dark collision complexes. Each collision complex contains two molecules so the number of complexes is half the number plotted.

the mechanism may be identifiable by the dependence of the loss rate on the induced dipole moment of the molecule [198, 201].

7.2 Experimental Measurements of Molecule Loss

In our experiment we observe the number of ground state molecules remaining in our 3D optical dipole trap as a function of time. An example plot of such a measurement may be seen in Fig. 7.2, with an initial peak density of 1.3×10^{11} cm^{-3}, initial temperature of 1.0 μK, and applied magnetic bias field of 181.5 G. In Fig. 7.2(a), we fit the results using the rate equations for one-, two- and three-body loss as given in section 7.1. The initial temperature is fixed during the fitting but its time evolution is a free parameter; as the molecule number decreases so does the optical depth of our absorption images which makes taking temperature measurements difficult.

We find that given our initial densities and signal to noise, it is hard to discern between the different possible loss mechanisms. The one-body process describes the experimental results least well; this is expected as our trapping light is far detuned from any available molecular transitions [202, 203]. In addition, our vacuum is good enough to allow lifetimes for ^{87}Rb atoms in a similar trap greater than 400 s, so the fitted 1-body time is therefore inconsistent with measurements on atoms. Similarly, we can also try to fit the result as a three-body process. Here we find a rate coefficient $K_3 = 7(1) \times 10^{-21}$ cm^6 s^{-1}, which is 8 orders of magnitude greater than the three-body loss rate measured in ^{87}Rb [196]. Fitting the results as a two-body process appears to generally describe the results best as shown in Fig. 7.2, though the difference in χ^2 is not statistically significant. For the results shown, we find a two-body fit gives a rate coefficient $K_2 = 1.7(1) \times 10^{-10}$ cm^3 s^{-1}. However, there is significant variation (up to a factor of ~ 2 variation) in the rate we measure day to day. This is rate is close to universal loss and is remarkably similar to all rate coefficients so far measured in other ultracold and optically trapped chemically stable bialkali species [28, 30, 32].

We can also fit the same results using the rate equations for 'sticky' collisions given in Eq. 7.7 as shown in Fig. 7.2(b). The fitting of two simultaneous decay processes enables this fit to better reproduce the fast loss we observe at short hold times. We can extract rate coefficients of $K_{\mathrm{mm}} = 9(5) \times 10^{-11}$ cm^3 s^{-1} and $K_{\mathrm{mc}} = 2(2) \times 10^{-10}$ cm^3 s^{-1}. The large uncertainty on K_{mc} is due to the low signal to noise when measuring low molecule numbers, which limits the amount of data which can be taken with long hold times. The fit also indicates that the lifetime of the collision complexes γ would likely be on the order of seconds, and significantly longer than the experimental times used here. However, similarly good fits to the results can be obtained using any multi-process fit such as a combination of one- and three-body loss.

Throughout the rest of this work, the loss will be assumed to be dominated by a two-body process and fits to the results will be given by solving the rate equations in Eq. 7.2. This will allow us to simply parametrise the loss by the single rate coefficient K_2.

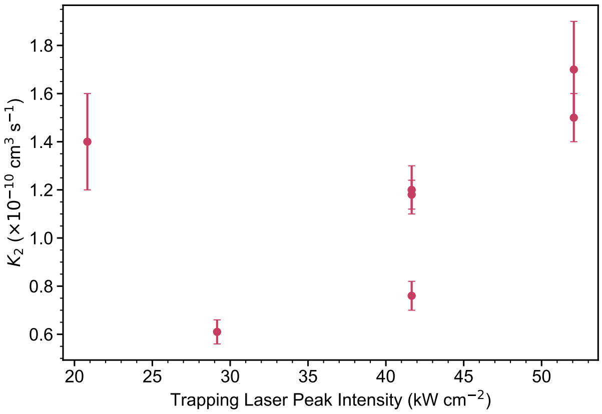

Figure 7.3: Dependence of two-body molecule loss rate K_2 on the intensity of the trapping laser. Error bars shown are those found during the fitting of the results. The real uncertainty in loss rate is likely significantly higher.

7.2.1 Dependence on Optical Trap Laser Intensity

To investigate the collision processes which are causing loss of molecules from our trap, we can change certain parameters in our experiment and observe how those parameters affect the rate of loss. The first parameter we investigate is the intensity I of our optical trapping beams. Varying the intensity of our trapping beams varies both the trap depth $\propto I$ and trap frequency $\propto \sqrt{I}$ observed by the molecules, it therefore leads to a variation in both temperature and density of the molecules. The variation of the two-body loss rate K_2 for rovibronic and hyperfine ground state molecules with intensity is shown in Fig. 7.3. The range of intensities over which we are able to trap molecules is limited by the minimum intensity we require to support the molecules against gravity, and by the maximum laser power we currently have available from our fibre laser. This intensity range corresponds to a variation of temperature of the molecules from $0.5\,\mu$K to $1.7\,\mu$K, and a variation in density between 1.1×10^{11} cm^{-3} and 1.5×10^{11} cm^{-3}. This further suggests that the loss mechanism may be a multi-body process, as this would lead to the observed lack of variation with intensity in the laser while our signal to noise may not be good enough to observe the change in loss over such a small variation in density.

At present, we observe significant day to day variation in the fitted value of K_2, much greater than the uncertainty given in the fit parameter. In Fig. 7.3

for example, we show three repeat measurements all with the same intensity dipole trap of ~ 42 kW cm^{-2}, yet one of the measurements differs from the others by a factor of two. Due to this variation, we are unable to identify any significant change in the loss with varying dipole trap intensity.

7.2.2 Magnetic Field Dependent Lifetime in the Rotational Ground State

Next we investigate the dependence of the lifetime of molecules in the $N = 0, M_F = 5$ state as a function of magnetic field. At 181.5 G, where our molecules are produced, this state is both the rotational and hyperfine ground state. It is no longer the hyperfine ground state below magnetic fields of ~ 90 G. At magnetic fields below this value, there is the possibility of loss of molecules to a lower energy hyperfine state. However, we would expect that such loss should have a relatively high energy centrifugal barrier associated with it and so loss by this mechanism is likely suppressed due to the low Zeeman energy released in changing hyperfine state.

In Fig. 7.4, we show measured molecular lifetimes for three different values of magnetic field. We note that at magnetic fields of 181.5 G and 25.6 G, we observe similar loss rates which agree even within the uncertainties in the fits. However, reducing the magnetic field to 3.5 G results in significantly increased loss, with over an order of magnitude increase in K_2. To see how the loss increases with magnetic field more carefully, in the inset we fix the hold time in the ground state to be 200 ms. We then vary the magnetic field and observe that the molecule number is relatively constant above 25 G but drops below this value corresponding to the increased loss rate.

Conveniently, a similar measurement has also been performed on the same molecule in a similar trap geometry by the group of Prof. Hanns-Christoph Nägerl at the University of Innsbruck. In their work [28], the molecules are at a higher temperature of 8.7 µK but similar density of 1.1×10^{11} cm^{-3} to our experiment. In the Innsbruck experiment, an increase in K_2 of similar magnitude to that which we observe is found. However, the magnetic field dependence is different as the transition occurs at a much higher magnetic field of 90 G; the point at which the $M_F = 5$ hyperfine state is no longer

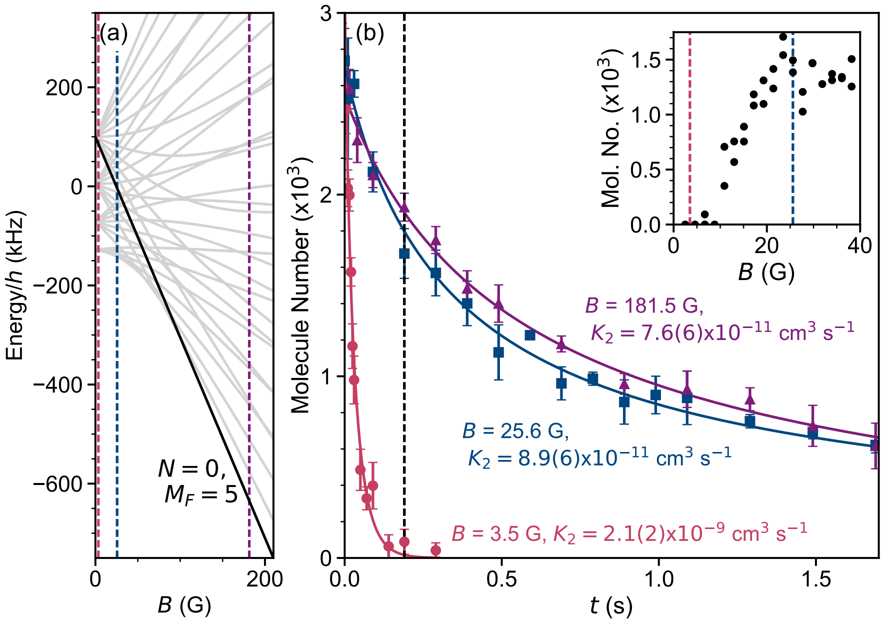

Figure 7.4: Dependence of the two-body molecule loss rate K_2 on the magnetic field. (a) Hyperfine structure of the rotational ground state of ^{87}Rb^{133}Cs. At $\sim$ 90 G the $N = 0, M_F = 5$ hyperfine state our molecules populate is no longer the hyperfine ground state. Vertical dashed lines show the magnetic fields at which we have performed full lifetime measurements. (b) Lifetime measurements at three different magnetic fields. The solid lines show two-body loss curves fitted to each result. Similar loss rates are measured at magnetic fields of 181.5 G and 25.6 G, but a much higher loss rate is observed at 3.5 G. Inset: The remaining molecules after a fixed hold time of 200 ms in the optical dipole trap as a function of magnetic field. A significant reduction in molecule number indicating a higher scattering rate is observed below 25 G.

the ground state. The original interpretation of the Innsbruck results was that hyperfine-changing collisions lead to loss once the initially populated hyperfine state is no longer the lowest in energy. This does not consider the presence of a centrifugal barrier which should energetically suppress such changes in hyperfine state as at the crossing point between the two states. There is no energy to enable to molecules to overcome this barrier. In addition, we observe similar lifetimes with the molecules in either the $M_F = 4$ and $M_F = 5$ hyperfine states at a magnetic field of 181.5 G, this would not be the case if the Innsbruck interpretation was correct. Our work demonstrates that this critical magnetic field appears to have some temperature dependence, though the real interpretation behind the result is still unknown and the subject of on-going investigations.

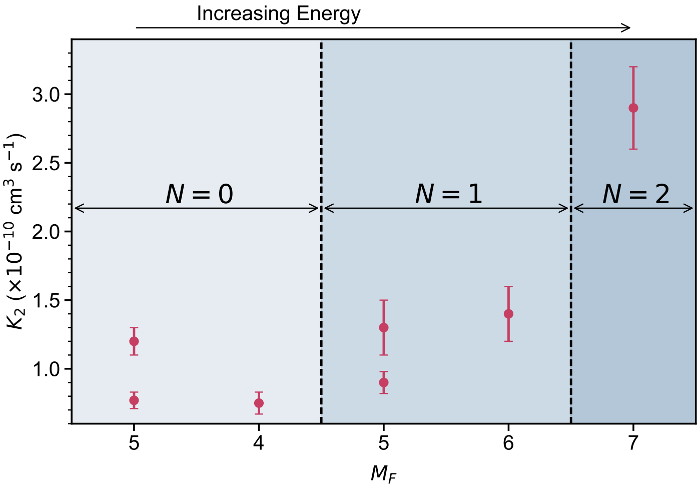

Figure 7.5: Two-body decay rates K_2 for molecules in a range of rotational and hyperfine states. The bias field is fixed at 181.5 G for all measurements, and the trap intensity and laser polarisation is chosen such that the trap frequency experienced by the molecules is similar independent of its state.

7.2.3 Lifetime in a Range of Rotational and Hyperfine States

Using a fixed dipole trap intensity and magnetic bias field of 181.5 G, we investigate the lifetime of molecules in a range of rotational and hyperfine states. In a similar way to the magnetic field variation, we might expect that in states which are not the ground state the loss rate may increase as they may decay to those states with lower energy. We transfer the molecules between states using π-pulses in free space as described in chapter 5. The polarisation of both beams in the crossed optical dipole trap are set to be parallel to the applied magnetic field; the AC Stark shift of each of the states we investigate is linear with no observed avoided crossings which enables efficient retrapping of the molecules (see Fig. 6.3). The intensity of the dipole trap is chosen independently for each state such that the molecules always experience a similar trap frequency, and are therefore trapped at the same temperature and density (although as previously discussed, the loss rate appears to be relatively insensitive to these parameters). Fig. 7.5 shows the fitted two-body rate coefficients for loss data taken for molecules in two hyperfine states in each of $N = 0$ and $N = 1$ and a single hyperfine level of $N = 2$. The rate coefficient for molecules in $N = 2$ is around twice that for molecules in the the first excited and ground rotational states. However, this is still within the normal variation we have observed in day to day measurements of the loss rate. This shows that the loss process we observe dominates over any hyperfine or rotational state changing collisions which may also take place. It also indicates that this may not be the reason why we observe increased loss as we reduce the magnetic field as shown in section 7.2.2, as at fixed magnetic field we can put the molecules in a higher energy hyperfine state and no increase in loss rate is observed.

7.3 Collisions Between Atoms and Molecules

The lifetime of a collision complex in a ‘sticky’ collision depends upon the density of states; the higher the density of states, the longer the complex lives and the more dominant the process becomes. To properly identify the role of such collisions, it may be helpful to vary the density of states. An obvious conclusion is to look at the case of atom-molecule collisions as an intermediate case between the incredibly high density of states of molecule-molecule collisions, and the relatively low density of states of atom-atom collisions. This could be achieved by removing the Stern-Gerlach separation step from the experimental routine, leaving the molecules and atoms together in the same trap. However, in practice it is preferable to study collisions between the molecules and only a single atomic species at a time. This can be achieved quite simply by only removing one atomic species from the trap following association using resonant light. However, we do not yet have the capability to do this in our experiment; a system to do this is currently in development.

When this is possible, we will be able to consider collisions of $^{87}\text{Rb}^{133}\text{Cs}$ molecules with the two available atomic collision partners in our experiment. For the case of molecule collisions with ^{87}Rb, the reaction

$$^{87}\text{Rb}^{133}\text{Cs} + {}^{87}\text{Rb} \rightarrow {}^{87}\text{Rb}_2 + {}^{133}\text{Cs} \tag{7.8}$$

is exothermic. We might therefore expect that a mixture of $^{87}\text{Rb}^{133}\text{Cs}$ and ^{87}Rb would be shorter lived than the molecule-only mixture if the molecule-molecule collision loss mechanism is not already universal. Collisions of the molecules with ^{133}Cs atoms on the other hand are chemically stable such that the reaction

$$^{87}\mathrm{Rb}^{133}\mathrm{Cs} + {}^{133}\mathrm{Cs} \rightarrow {}^{87}\mathrm{Rb} + {}^{133}\mathrm{Cs}_2 \tag{7.9}$$

is endothermic. This mixture therefore offers the perfect opportunity to study the dependence of our observed loss on the density of states. In addition, if we can find a way to suppress the loss of molecules, it may in the future be possible to use the ^{133}Cs atoms for sympathetic cooling.

7.4 Summary

In summary, we observe loss of molecules from our 3D optical dipole trap with a lifetime of the order of ~ 1 s. We have discussed the available collision processes which may take place in an ultracold gas, and how they may be characterised as one-, two-, or three-body loss. We have also outlined how the high density of states which may contribute to the behaviour in molecule-molecule collisions can lead to long-lived two-molecule collision complexes, and a delayed but enhanced three-body loss of molecules due to the so-called 'sticky' collisions. We have studied the loss of molecules as a function of intensity of the trapping light, magnetic field, and rotational and hyperfine state. Most significantly, we observe an increase in the loss rate for molecules in the rotational ground state at magnetic fields below 25 G. This contradicts the results from similar experiments performed on the same molecule at Innsbruck [28], and indicates that this behaviour likely has some dependence on temperature of the molecules. Finally, we have discussed the next step we hope to take in our experiment - to study collisions in a mixture of molecules and atoms.

Chapter 8

Conclusion

In this work we have developed the tools to precisely control the motion and internal quantum state of polar molecules. Such control is at the heart of many applications proposed for systems of ultracold polar molecules, and this work represents a key evolutionary step for our experiment from a machine designed to produce ultracold molecules to one which can exploit those molecules to achieve new scientific goals. We have demonstrated the crossing of this boundary by studying the collision processes which may occur between the optically trapped molecules, and there are many more possibilities for the future.

8.1 Summary

We have described an apparatus which, by associating molecules from a pre-cooled atomic mixture, produces up to 4000 optically trapped ^{87}Rb^{133}Cs molecules in their rovibronic and hyperfine ground state, at a temperature of 1 µK and a peak density of 10^{11} cm^{-3}. We measure the binding energy of the molecules in the rovibronic ground state to be $h \times 114\,268\,135.24(4)(3)$ MHz; achieved by measuring the frequency of the lasers used in ground-state transfer with reference to an optical frequency comb. In addition, by applying a DC electric field to the molecular sample, we observe the DC Stark shift of the rovibrational ground state and determine a molecule-frame electric dipole moment of 1.225(3)(8) D. Given the maximum electric field we currently have accessible in our experiment, this corresponds to a laboratory-frame dipole moment of 0.355(4) D.

The transitions between the low-energy rotational states of the molecule have been probed using external microwave fields. With the molecules starting in the hyperfine ground state, we initially performed microwave spectroscopy of the first rotationally excited state in free space. We were able to resolve hyperfine states spaced by $\sim$ 40 kHz, and with precision down to $\sim$ 50 Hz. Transitions to 8 of the 96 available hyperfine levels available were both selection-rule allowed and had sufficient coupling strength to be observable. By performing the spectroscopy at two magnetic fields we were able to measure the Zeeman shifts and, by fitting of theory to experiment, obtain new experimental values for the rotational constant, scalar spin-spin coupling constant, electric quadrupole coupling constants, and nuclear g-factors (including shielding) for the molecule.

We have shown that one- and two-photon π-pulses may be used to transfer the population between the ground, first, and second rotationally excited states with unity efficiency. In addition, the mixing of states that arises from nuclear quadrupole coupling offers a method of changing hyperfine state via two-photon transfer. We have also briefly investigated how coherent superpositions of states can be generated in our experiment; a superposition of rotational states can be used to activate dipole-dipole interactions even in the absence of a DC electric field. In addition, we have discussed how Ramsey interferometry may be a vital and highly sensitive tool to investigate interactions within the ultracold molecular gas.

The effect of the trapping light on the molecules has been investigated, and both the isotropic and anisotropic components of the polarisability completely characterised for the ^{87}Rb^{133}Cs molecule. We have found that the trapping light couples neighbouring hyperfine states, giving rich and complex structure with many avoided crossings as a function of laser intensity. This coupling may be controlled by varying the laser polarisation which enables the possibility of engineering avoided crossings if and when experiments require. In contrast to previous works which propose the existence of a *magic* angle between the laser polarisation and magnetic field, in our experiment no such angle appears to exist as these two quantities compete to take the role of the angular momentum quantisation axis.

Finally, we have investigated the lifetime of molecules in our 3D optical trap as a function of laser intensity, magnetic field, and internal state. Despite the chemical stability of the molecules, we observe surprisingly high loss rates leading to lifetimes for the molecules of around 1 s. At present, we are unable to discern the dominant loss process. We have found that the lifetime of molecules in the spin-stretched $M_F = 5$ hyperfine level of the rotational ground state depends upon magnetic field; the rate of loss of molecules appears to increase significantly below 25 G. The magnetic field at which this occurs is lower than has been observed in similar experiments performed at the University of Innsbruck, which were performed at a similar density but significantly higher temperature. The cause of the unexpectedly short lifetimes of chemically stable molecules is one of the big unanswered questions of the field, and one which may have highly important implications for many future experiments. We have outlined the next step we would like to take in our quest to understand these collisions; studying the collisions between atomic and molecular species.

8.2 Outlook

The future of experiments with polar molecules in our group is bright, and we have many varied goals which we hope to achieve in the near future. Here we will discuss some of the key directions which are being investigated as a continuation of the experiments presented in this thesis.

8.2.1 Optical Lattices

Collisional loss of molecules may be investigated and even suppressed by confinement to optical traps with reduced dimensionality. In addition, the majority of applications for ultracold molecules in quantum computing and quantum simulation require the loading of molecules into optical lattices such that interactions must occur over long-range. At present a single retro-reflected 1064 nm beam may be used as a 1D optical lattice in our experiment (see Fig. 3.3). So far, ^{87}Rb atoms have been successfully loaded into this trap and there is the possibility of loading molecules after ground state transfer into this same geometry. However, we are currently in the process of replacing this setup with a pair of retro-reflected beams to create a 2D optical lattice instead. In this new geometry, the molecules would be confined to a series of vertical tubes. Given the density of the molecules we currently achieve and spacing of the tubes at this wavelength we could expect to trap on average only two molecules in each site. This should therefore be the perfect test bed to determine whether the loss process we observe in our experiments is one-, two-, or three-body. In addition, we can then attempt to control collisions between these small numbers of molecules by applying DC electric fields parallel or perpendicular to the long axis of these tubes. Another natural direction is to control these collisions not just with the trap geometry, but by using the dipole-dipole interactions. By transferring the molecules to a microwave dressed state for instance, it is possible to tune the collisions between molecules to be either attractive or repulsive [204]. This could give us further insight into the collision mechanisms which dominate the ultracold molecular gas, or at least enable further cooling of the molecules by sympathetic cooling with atomic Cs.

Further ahead in the future, the addition of a third retro-reflected beam would give access to a full 3D optical lattice. This could be useful for suppressing loss of molecules all together and is also a requirement for many proposed applications, enabling the exploration of exotic quantum phases [205–207], quantum magnetism [18, 208], and quantum simulation [19] - i.e. the long-term goal we are working towards in our experiment. Achieving a high filling factor in such a lattice has proved difficult in similar molecule experiments; typically a filling factor of around 30% has been achievable [209–211] by forming a double atomic Mott insulator prior to molecule formation.

8.2.2 Other Bialkali Species

Working with ^{87}Rb^{133}Cs has two primary limitations. Firstly, the mixture of ^{87}Rb^{133}Cs is difficult to work with at high phase-space densities; the high interspecies scattering length leads to immiscibility of a quantum degenerate mixture [115], which leads to low efficiency during the magnetoassociation of molecules [167]. This problem may be circumvented by using the more abundant ^{85}Rb isotope. Our experiment has already performed measurements to determine the positions of magnetic Feshbach resonances in an ultracold mixture of ^{85}Rb and ^{133}Cs. However, cooling of ^{85}Rb is much more difficult than for ^{87}Rb; creating a mixture with sufficiently high phase-space density for magnetoassociation is therefore non-trivial and may require alternative cooling techniques such as Raman sideband cooling for ^{133}Cs.

The second limitation is that the two isotopes ^{87}Rb^{133}Cs and ^{85}Rb^{133}Cs available in our current experiment are bosonic. A molecule which has both fermionic and bosonic isotopes may be very useful for future investigations. As discussed in section 2.1, there are a limited number of chemically stable bialkali molecules, and even fewer also have fermionic isotopes; the only options available are NaK and KCs molecules. During the course of this work, one group has reported the creation of a chemically stable ultracold gas of fermionic polar molecules; the group of Prof. Martin Zwierlein at MIT work with ^{23}Na^{40}K. However, promising Feshbach resonances for magnetoassociation have been predicted for ^{40}K^{133}Cs molecules [79], and this molecule ties in well with the wealth of experience in working with ^{133}Cs in our group [115, 212–214]. An experiment to investigate an atomic mixture of K and Cs is currently under construction. Preliminary work on spectroscopy of potassium was published in [215].

8.2.3 Optical Tweezers

Optical microtraps are a powerful tool which have been used by many groups in the capture of single atoms [216, 217]. However, they may also be useful to the field of ultracold molecules. By preparing exactly the number of molecules required for an experiment, the species involved in a reaction could unambiguously be determined [218]. In addition, this method greatly simplifies the creation of ordered arrays of molecules with unity site filling.

Loading of molecules into optical microtraps may be performed following either direct or indirect cooling methods - both methods are currently being investigated as part of ‘Quantum Science with Ultracold Molecules’ (QSUM), a new initiative between Durham University and Imperial College

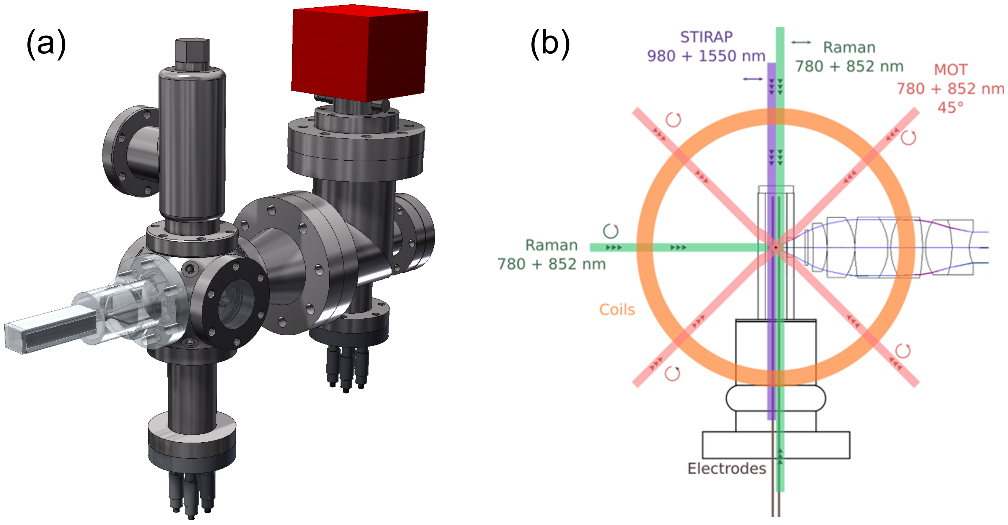

Figure 8.1: Design for the Durham molecule tweezer experiment. (a) Compact single chamber vacuum system for the experiment. An array of four rod electrodes will be placed in vacuum, enabling electric fields to be applied to the molecules with minimal charge build up on the walls of the cell. (b) Optical layout for beams entering the glass cell. A high objective (NA~ 0.5) lens is positioned outside of the glass cell to focus the light down for the optical tweezer trap and to collect light for detection of atoms and molecules. MOT beams, Raman cooling beams and the STIRAP beams necessary for the experiment are also shown.

London [219]. The indirect approach which follows on directly from the work presented in this thesis will involve the loading of ^{87}Rb and ^{133}Cs atoms into individual tweezer traps. Following cooling of each species to their motional ground states by Raman sideband cooling, these traps could then be merged and a single molecule produced via magnetoassociation followed by STIRAP. The newly designed system for the Durham molecule tweezer experiment is shown in Fig. 8.1.

8.2.4 Molecular Quantum Gas Microscope

Quantum gas microscopes are capable of imaging atoms in a single plane of an optical lattice with single-site and single-atom resolution [220]. An equivalent molecular microscope will enable us to detect individual molecules in a lattice. Such a device may be used for the detection of the novel quantum phases predicted for polar molecules in optical lattices where spatial correlations are expected. The microscope will also make is possible to address the individual

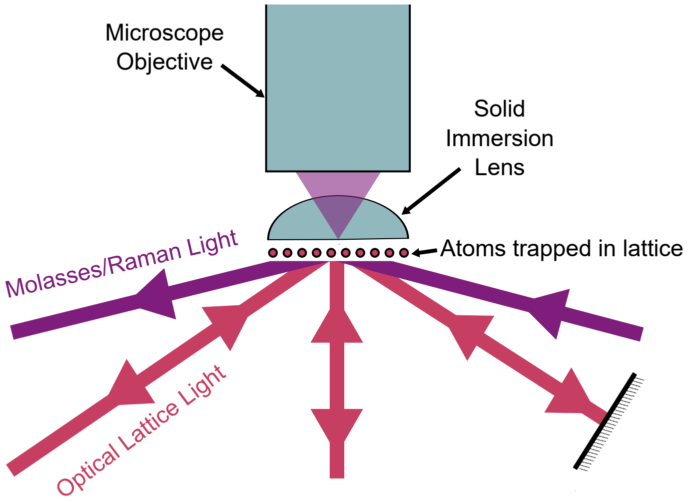

Figure 8.2: Typical experimental apparatus for an atomic quantum gas microscope. A combination of a microscope objective and solid immersion lens close to the atoms typically achieves an effective numerical aperture of ∼ 0.8 [220]. The atoms are illuminated from the side by molasses/Raman light, and the scattered fluorescence light is collected by the objective lens and projected onto a CCD camera.

molecules in the lattice. For example, by creating a local AC Stark shift using a focussed off-resonant laser beam, a microwave pulse can be used to transfer a single molecule to an excited rotational state. This technique has been demonstrated for atoms [221] and allows the direct monitoring of the quantum tunneling dynamics of individual particles.

The atomic quantum gas microscope consists of a high-resolution optical imaging system integrated with a 2D optical lattice for confining the atoms. The spacing between lattice sites is typically ∼ 500 nm. Resolving individual sites requires a custom microscope objective lens with a very high numerical aperture situated close to the place of the lattice as shown in Fig. 8.2. Microscopes have been used to observe directly the spatial structures and ordering associated with the Mott-insulator transition [222, 223] in the Bose-Hubbard model and to investigate the correlations and dynamics in such systems [224, 225].

Adapting the methods developed for atoms to a molecular system will be a complex task, however our group is working towards this goal also as part of the QSUM project [219]. One particular problem of note arises from the fact that we cannot image the molecules directly due to the absence of sufficiently

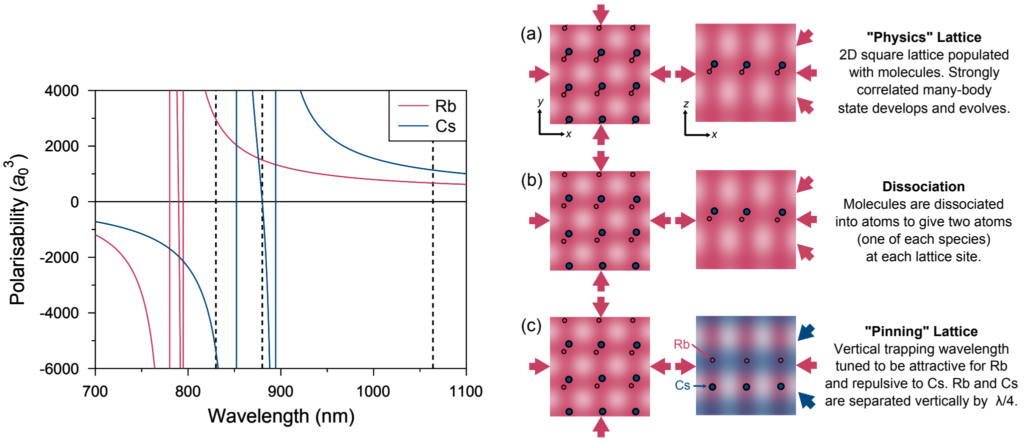

"Physics" Lattice
2D square lattice populated with molecules. Strongly correlated many-body state develops and evolves.

Dissociation
Molecules are dissociated into atoms to give two atoms (one of each species) at each lattice site.

"Pinning" Lattice
Vertical trapping wavelength tuned to be attractive for Rb and repulsive to Cs. Rb and Cs are separated vertically by λ/4.

Figure 8.3: Trapping scheme for a molecular quantum gas microscope. Left: Polarisability of ^{87}Rb and ^{133}Cs atoms. The black dashed lines indicate the primary trapping wavelengths which may be useful in future experiments. Right: Scheme for separating ^{87}Rb and ^{133}Cs atoms for imaging. Coloured arrows indicate direction of lattice beams. (a) We begin by loading a 2D square lattice with molecules. (b) Following the evolution in the lattice, the molecules are dissociated back into atoms. We choose a trapping wavelength where both ^{87}Rb and ^{133}Cs seek the high intensity regions, and hence share lattice sites. (c) By switching the lattice light in the vertical (z) direction to 830 nm, the ^{87}Rb and ^{133}Cs are spatially separated for imaging.

closed cooling transitions. We will therefore need to dissociate the molecules back to atoms as we do in our current experimental procedure. However, during the imaging process, light assisted collisions between pairs of atoms would cause both atoms to be ejected from the trap within ~100 µs while exposure times of typically 100-1000 ms are required to scatter sufficient photons to be detected. The atoms will therefore need to be separated by using species-specific trapping techniques. One possibility is to separate the two species into different vertical sites during the imaging sequence, through careful choice of wavelength. Fig. 8.3 (left) shows the polarisability of ^{87}Rb and ^{133}Cs as a function of wavelength. At 1064 nm, both have positive polarisabilities and are attracted to the high-intensity antinodes of the lattice. Around 830 nm, the polarisability of ^{87}Rb is positive, whereas for ^{133}Cs it is negative. This wavelength can be used to separate the two species because ^{87}Rb is attracted to the antinodes, while ^{133}Cs is repelled. Fig. 8.3 (right) shows how we can use the species-specific lattice to implement the microscope imaging.

A further challenge is to be able to apply uniform electric fields to the molecules in the lattice. This requirement negates the option of using a solid immersion lens as shown in Fig. 8.2, as charge can easily build up on the dielectric surface of the lens. This would generate stray electric fields which would interfere with experiments; a problem which we have already experienced in the current apparatus using electrodes placed out of vacuum. To circumvent this problem, a high resolution objective lens which also has a reasonably long distance must be used. The implementation of a quantum gas microscope for molecules will require the development of a new dedicated apparatus as our existing setup does not have the optical access to add high-resolution imaging optics.

8.3 Concluding Remarks

In this thesis we have developed the methods for producing and optically trapping ultracold polar molecules in well-defined controllable quantum states. The techniques presented here represent a step forward for our ^{87}Rb^{133}Cs experiment towards the long-term goal of creating a quantum simulator with polar molecules. However, as is often the case in science, the development of new tools opens up numerous alternative avenues also worthy of exploration. As such, now is a very exciting time to be a part of the burgeoning field of ultracold molecules, and our experiment is one of the first few to investigate this previously uncharted territory.

Appendix A

Collision Heating Rates

In chapter 7, loss processes associated with one-, two-, and three-body collisions are discussed and specifically we state the average mean energy that each molecule carries away with it when lost during each sort of process. To calculate these energies we use the Boltzmann distribution function for a gas confined to an axially symmetric potential,

$$f(\vec{x}, \vec{v}) = \frac{N m^3 \omega_r^2 \omega_z}{8\pi^3 k_B^3 T^3} \exp\left(-\frac{mv^2}{2k_B T} - \frac{m}{2k_B T}(\omega_r^2 r^2 + \omega_z^2 z^2)\right). \tag{A.1}$$

Here, $\vec{x}$ and $\vec{v}$ are vectors describing the position and velocity of a single particle in the ensemble, N is the total number of particles, T is the temperature of the ensemble, ω_r and ω_z are the radial and axial trap frequencies respectively, and k_B is Boltzmann's constant. To calculate the average energy of each molecule in our sample, we calculate the total kinetic and potential energy and divide by the total number of molecules

$$\bar{E} = \frac{1}{N} \int d^3x \; d^3v \left(\frac{1}{2}mv^2 + \frac{1}{2}m(\omega_r^2 r^2 + \omega_z^2 z^2)\right) f(\vec{x}, \vec{v}) = 3k_B T, \tag{A.2}$$

which is also equal to the average energy taken away by a molecule lost by a one-body process (i.e. a process with no density dependence). Two-body loss processes depend upon the square of the density n^2, and therefore the average energy taken away during a two-body process is calculated as

$$\bar{E}_{\text{2-body}} = \frac{1}{N^2} \int d^3x \; d^3v \left(\frac{1}{2}mv^2 + \frac{1}{2}m(\omega_r^2 r^2 + \omega_z^2 z^2)\right) f(\vec{x}, \vec{v})^2 = \frac{9}{4}k_B T. \tag{A.3}$$

Similarly, three-body loss processes depend on n^3 and the average energy is therefore

$$\bar{E}_{\text{3-body}} = \frac{1}{N^3}\int d^3x\; d^3v \left(\frac{1}{2}mv^2 + \frac{1}{2}m(\omega_r^2 r^2 + \omega_z^2 z^2)\right) f(\vec{x},\vec{v})^3 = 2k_B T. \tag{A.4}$$

Bibliography

[1] M. H. Anderson, J. R. Ensher, M. R. Matthews, C. E. Wiemann, and E. A. Cornell, Science **269**, 198 (1995).

[2] C. C. Bradley, C. A. Sackett, J. J. Tollett, and R. G. Hulet, Phys. Rev. Lett. **75**, 1687 (1995).

[3] K. B. Davis, M. O. Mewes, M. R. Andrews, N. J. van Druten, D. S. Durfee, D. M. Kurn, and W. Ketterle, Phys. Rev. Lett. (1995).

[4] F. Dalfovo, S. Giorgini, L. P. Pitaevskii, and S. Stringari, Rev. Mod. Phys. **71**, 463 (1999).

[5] E. A. Cornell and C. E. Wiemann, Rev. Mod. Phys. **74**, 875 (2002).

[6] W. Ketterle, Rev. Mod. Phys. **74**, 1131 (2002).

[7] I. Bloch, J. Dalibard, and W. Zwerger, Rev. Mod. Phys. **80**, 885 (2008).

[8] D. Jaksch, Contemporary Physics **45**, 367 (2004).

[9] I. Bloch, Nature **453**, 1016 (2008).

[10] I. Bloch, Nature Physics **1**, 23 (2005).

[11] M. Lewenstein, A. Sanpera, V. Ahufinger, B. Damski, A. Sen(De), and U. Sen, Advances in Physics **56**, 243 (2007).

[12] K. Aikawa, A. Frisch, M. Mark, S. Baier, A. Rietzler, R. Grimm, and F. Ferlaino, Phys. Rev. Lett. **108**, 210401 (2012).

[13] S. Baier, M. J. Mark, D. Petter, K. Aikawa, L. Chomaz, Z. Cai, M. Baranov, P. Zoller, and F. Ferlaino, Science **352**, 201 (2016).

[14] M. Lu, S. H. Youn, and B. L. Lev, Phys. Rev. Lett. **104**, 063001 (2010).

[15] M. Saffman, T. G. Walker, and K. Mø lmer, Rev. Mod. Phys. **82**, 2313 (2010).

[16] R. V. Krems, Phys. Chem. Chem. Phys. **10**, 4079 (2008).

[17] N. Balakrishnan, J. Chem. Phys. **145**, 150901 (2016).

[18] R. Barnett, D. Petrov, M. Lukin, and E. Demler, Phys. Rev. Lett. **96**, 190401 (2006).

[19] A. Micheli, G. K. Brennen, and P. Zoller, Nature Physics **2**, 341 (2006).

[20] H. P. Büchler, A. Micheli, and P. Zoller, Nature Physics **3**, 726 (2007).

[21] G. K. Brennen, A. Micheli, and P. Zoller, New J. Phys. **9**, 138 (2007).

[22] A. V. Gorshkov, S. R. Manmana, G. Chen, J. Ye, E. Demler, M. D. Lukin, and A. M. Rey, Phys. Rev. Lett. **107**, 115301 (2011).

[23] D. DeMille, Phys. Rev. Lett. **88**, 067901 (2002).

[24] S. F. Yelin, K. Kirby, and R. Côté, Phys. Rev. A **74**, 050301(R) (2006).

[25] T. E. Wall, J. Phys. B: At. Mol. Opt. Phys. **49**, 243001 (2016).

[26] K.-K. Ni, S. Ospelkaus, M. H. G. de Miranda, A. Pe'er, B. Neyenhuis, J. J. Zirbel, S. Kotochigova, P. S. Julienne, D. S. Jin, and J. Ye, Science **322**, 231 (2008).

[27] J. Deiglmayr, A. Grochola, M. Repp, K. Mörtlbauer, C. Glück, J. Lange, O. Dulieu, R. Wester, and M. Weidemüller, Phys. Rev. Lett. **101**, 133004 (2008).

[28] T. Takekoshi, L. Reichsöllner, A. Schindewolf, J. M. Hutson, C. R. Le Sueur, O. Dulieu, F. Ferlaino, R. Grimm, and H.-C. Nägerl, Phys. Rev. Lett. **113**, 205301 (2014).

[29] P. K. Molony, P. D. Gregory, Z. Ji, B. Lu, M. P. Köppinger, C. R. Le Sueur, C. L. Blackley, J. M. Hutson, and S. L. Cornish, Phys. Rev. Lett. **113**, 255301 (2014).

[30] J. W. Park, S. A. Will, and M. W. Zwierlein, Phys. Rev. Lett. **114**, 205302 (2015).

[31] T. Shimasaki, M. Bellos, C. D. Bruzewicz, Z. Lasner, and D. DeMille, Phys. Rev. A **91**, 021401(R) (2015).

[32] M. Guo, B. Zhu, B. Lu, X. Ye, F. Wang, R. Vexiau, N. Bouloufa-Maafa, G. Quéméner, O. Dulieu, and D. Wang, Phys. Rev. Lett. **116**, 205303 (2016).

[33] W. D. Phillips, Rev. Mod. Phys. **70**, 721 (1998).

[34] J. T. Bahns, W. C. Stwalley, and P. L. Gould, J. Chem. Phys. **104**, 9689 (1996).

[35] A. Trabesinger, Nature Physics **6**, 719 (2010).

[36] J. Brown and A. Carrington, *Rotational Spectroscopy of Diatomic Molecules* (Cambridge University Press, Cambridge, U.K., 2003).

[37] M. R. Tarbutt, New J. Phys. **17**, 015007 (2015).

[38] M. R. Tarbutt and T. C. Steimle, Phys. Rev. A **92**, 053401 (2015).

[39] E. S. Shuman, J. F. Barry, and D. DeMille, Nature **467**, 820 (2010).

[40] L. R. Hunter, S. K. Peck, A. S. Greenspon, S. Saad Alam, and D. DeMille, Phys. Rev. A **85**, 012511 (2012).

[41] J. F. Barry and D. DeMille, 491 **491**, 539 (2012).

[42] M. T. Hummon, M. Yeo, B. K. Stuhl, C. L. Alejandra, Y. Xia, and J. Ye, Phys. Rev. Lett. **110**, 143001 (2013).

[43] J. F. Barry, D. J. McCarron, E. B. Norrgard, M. H. Steinecker, and D. DeMille, Nature **512**, 286 (2014).

[44] D. J. McCarron, E. B. Norrgard, M. H. Steinecker, and D. DeMille, New. J. Phys. **17**, 035014 (2015).

[45] V. Zhelyazkova, A. Cournal, T. E. Wall, A. Matsushima, J. J. Hudson, E. A. Hinds, M. R. Tarbutt, and B. E. Sauer, Phys. Rev. A **89**, 053416 (2014).

[46] R. V. Krems, W. C. Stwalley, and B. Friedrich, eds., *Cold Molecules: Theory, Experiment, Applications* (CRC Press, 2009).

[47] S. K. Tokunaga, J. M. Dyne, E. A. Hinds, and M. R. Tarbutt, New J. Phys. **11**, 055038 (2009).

[48] T. E. Wall, J. F. Kanem, J. M. Dyne, J. J. Hudson, B. E. Sauer, E. A. Hinds, and M. R. Tarbutt, Phys. Chem. Chem. Phys. **13**, 18991 (2011).

[49] N. Vanhaecke, U. Meier, M. Andrist, B. H. Meier, and F. Merkt, Phys. Rev. A **75**, 031402(R) (2007).

[50] E. Lavert-Ofir, S. Gersten, A. B. Henson, I. Shani, L. David, J. Narevicius, and E. Narevicius, New J. Phys. **13**, 103030 (2011).

[51] E. Lavert-Ofir, L. David, A. B. Henson, S. Gersten, J. Narevicius, and E. Narevicius, Phys. Chem. Chem. Phys. **13**, 18948 (2011).

[52] N. Akerman, M. Karpov, L. David, E. Lavert-Ofir, J. Narevicius, and E. Narevicius, New J. Phys. **17**, 065015 (2015).

[53] J. D. Weinstein, R. deCarvalho, T. Guillet, B. Friedrich, and J. M. Doyle, Nature **195**, 148 (1998).

[54] S. M. Skoff, R. J. Hendricks, C. D. J. Sinclair, M. R. Tarbutt, J. J. Hudson, D. M. Segal, B. E. Sauer, and E. A. Hinds, New J. Phys. **11**, 123026 (2009).

[55] A. C. Vutha, W. C. Campbell, Y. V. Gurevich, N. R. Hutzler, M. Parsons, D. Patterson, E. Petrik, B. Spaum, J. M. Doyle, G. Gabrielse, and D. DeMille, J. Phys. B: At. Mol. Opt. Phys. **43**, 074007 (2010).

[56] S. M. Skoff, R. J. Hendricks, C. D. J. Sinclair, J. J. Hudson, D. M. Segal, B. E. Sauer, E. A. Hinds, and M. R. Tarbutt, Phys. Rev. A **83**, 023418 (2011).

[57] C. H. Raymond Ooi, K.-P. Marzlin, and J. Audretsch, Eur. Phys. J. D **22**, 259 (2003).

[58] M. Zeppenfeld, M. Motsch, P. W. H. Pinkse, and G. Rempe, Phys. Rev. A **80**, 041401(R) (2009).

[59] M. Zeppenfeld, G. U. Englert, Barbara, R. Glöckner, A. Prehn, M. Mielenz, C. Sommer, L. D. van Burren, M. Motsch, and G. Rempe, Nature **491**, 570 (2012).

[60] F. K. Fatemi, K. M. Jones, P. D. Lett, and E. Tiesinga, Phys. Rev. A **66**, 053401 (2002).

[61] A. J. Kerman, J. M. Sage, S. Sainis, T. Bergeman, and D. DeMille, Phys. Rev. Lett. **92**, 033004 (2004).

[62] J. M. Sage, S. Sainis, T. Bergeman, and D. DeMille, Phys. Rev. Lett. **94**, 203001 (2005).

[63] R. Ciurylo, E. Tiesinga, S. Kotochigova, and P. S. Julienne, Phys. Rev. A **70**, 062710 (2004).

[64] K. M. Jones, E. Tiesinga, P. D. Lett, and P. S. Julienne, Rev. Mod. Phys. **78**, 483 (2006).

[65] T. Köhler, K. Góral, and P. S. Julienne, Rev. Mod. Phys. **78**, 1311 (2006).

[66] J. G. Danzl, E. Haller, M. Gustavsson, M. J. Mark, R. Hart, N. Bouloufa, O. Dulieu, H. Ritsch, and H.-C. Nägerl, Science **321**, 1062 (2008).

[67] F. Lang, K. Winkler, C. Strauss, R. Grimm, and J. Hecker Denschlag, Phys. Rev. Lett. **101**, 133005 (2008).

[68] K.-K. Ni, *A Quantum Gas of Polar Molecules*, Ph.D. thesis, University of Colorado (2009).

[69] P. S. Zúchowski and J. M. Hutson, Phys. Rev. A **81**, 060703(R) (2010).

[70] S. Ospelkaus, K.-K. Ni, G. Quéméner, B. Neyenhuis, D. Wang, M. H. G. de Miranda, J. L. Bohn, J. Ye, and D. S. Jin, Phys. Rev. Lett. **104**, 030402 (2010).

[71] K.-K. Ni, S. Ospelkaus, D. J. Nesbitt, J. Ye, and D. S. Jin, Phys. Chem. Chem. Phys. **322**, 231 (2009).

[72] K.-K. Ni, S. Ospelkaus, D. Wang, G. Quéméner, B. Neyenhuis, M. H. G. de Miranda, J. L. Bohn, J. Ye, and D. S. Jin, Nature **464**, 1324 (2010).

[73] M. H. G. de Miranda, A. Chotia, B. Neyenhuis, D. Wang, G. Quéméner, S. Ospelkaus, J. L. Bohn, J. Ye, and D. S. Jin, Nature Physics **7**, 502 (2011).

[74] B. Yan, S. A. Moses, B. Gadway, J. P. Covey, K. R. A. Hazzard, A. M. Rey, D. S. Jin, and J. Ye, Nature **501**, 521 (2013).

[75] A. Barenco, D. Deutsch, A. Ekert, and R. Jozsa, Phys. Rev. Lett. **74**, 4083 (1995).

[76] E. Urban, T. A. Johnson, T. Henage, L. Isenhower, D. D. Yavuz, T. G. Walker, and M. Saffman, Nature Physics **5**, 110 (2009).

[77] M. Gröbner, P. Weinmann, F. Meinert, K. Lauber, E. Kirilov, and H.-C. Nägerl, Journal of Modern Optics **63**, 1829 (2015).

[78] D. Borsalino, R. Vexiau, M. Aymar, E. Luc-Koenig, O. Dulieu, and N. Bouloufa-Maafa, J. Phys. B: At. Mol. Opt. Phys. **49**, 055301 (2016).

[79] H. J. Patel, C. L. Blackley, S. L. Cornish, and J. M. Hutson, Phys. Rev. A **90**, 032716 (2014).

[80] M. Aymar and O. Dulieu, J. Chem. Phys. **122**, 204302 (2005).

[81] J. W. Park, Z. Z. Yan, L. Huanqian, S. A. Will, and M. W. Zwierlein, arXiv:1606.04184 (2016).

[82] I. Bloch, J. Dalibard, and S. Nascimbéne, Nature Physics **8**, 267 (2012).

[83] R. Blatt and C. F. Roos, Nature Physics **8**, 277 (2012).

[84] A. Aspuru-Guzik and P. Walther, Nature Physics **8**, 285 (2012).

[85] A. A. Houck, H. E. Türeci, and J. Koch, Nature Physics **8**, 292 (2012).

[86] J. J. Hudson, D. M. Kara, I. J. Smallman, B. E. Sauer, M. R. Tarbutt, and E. A. Hinds, Nature **473**, 493 (2011).

[87] The ACME Collaboration, J. Baron, W. C. Campbell, D. DeMille, J. M. Doyle, G. Gabrielse, Y. V. Gurevich, P. W. Hess, N. R. Hutzler, E. Kirilov, I. Kozyryev, B. R. O'Leary, C. D. Panda, M. F. Parsons, E. S. Petrik, B. Spaun, A. C. Vutha, and A. D. West, Science **343**, 269 (2014).

[88] S. Truppe, R. J. Hendricks, S. K. Tokunaga, H. J. Lewandowski, M. G. Kozlov, C. Kenkel, E. A. Hinds, and M. R. Tarbutt, Nature Communications **4** (2013), 10.1038/ncomms3600.

[89] H. Hideaki, Y. Takasu, Y. Yamaoka, J. M. Doyle, and Y. Takahashi, Phys. Rev. Lett. **106**, 205304 (2011).

[90] K. L. Butler, *A dual species MOT of Yb and Cs*, Phd thesis, Durham University, UK (2014).

[91] A. Guttridge, S. A. Hopkins, S. L. Kemp, D. Boddy, R. Freytag, M. P. A. Jones, M. R. Tarbutt, E. A. Hinds, and S. L. Cornish, J. Phys. B: At., Mol. Opt. Phys. **49**, 145006 (2016).

[92] G. Igel-Mann, U. Wedig, P. Fuentealba, and H. Stoll, J. Chem. Phys. **84**, 5007 (1986).

[93] J. Dieglmayr, M. Ayman, R. Wester, M. Wedemüller, and O. Dulieu, J. Chem. Phys. **129**, 064309 (2008).

[94] T. Takekoshi, M. Debatin, R. Rameshan, F. Ferlaino, R. Grimm, H.-C. Nägerl, C. R. Le Sueur, J. M. Hutson, P. S. Julienne, S. Kotochigova, and E. Tiemann, Phys. Rev. A **85**, 032506 (2012).

[95] D. J. Owens, T. Xie, and J. M. Hutson, Phys. Rev. A **94**, 023619 (2016).

[96] M. L. Harris, *Realisation of a cold mixture of rubidium and caesium*, Ph.D. thesis, Durham University (2008).

[97] P. Tierney, *Magnetic trapping of an ultracold Rb-Cs mixture*, Ph.D. thesis, Durham University (2009).

[98] D. J. McCarron, *A quantum degenerate mixture of ^{87}Rb and ^{133}Cs*, Ph.D. thesis, Durham University (2011).

[99] D. L. Jenkin, *Feshbach spectroscopy of an ultracold Rb-Cs mixture*, Ph.D. thesis, Durham University (2012).

[100] M. P. Köppinger, *Creation of ultracold RbCs molecules*, Ph.D. thesis, Durham University (2014).

[101] P. K. Molony, *Creation of ultracold dipolar ground-state RbCs molecules*, Ph.D. thesis, Durham University (2016).

[102] T. H. Boyer, Am. J. Phys. **56**, 688 (1988).

[103] R. Grimm, M. Weidemüller, and Y. B. Ovchinnikov, Adv. At. Mol. Opt. Phy. **42**, 95 (2000).

[104] J. Weiner, V. S. Bagnato, S. Zilio, and P. S. Julienne, Rev. Mod. Phys. **71**, 1 (1999).

[105] J. Dalibard, in *Proceedings of the International School of Physics*, Enrico Fermi, Varenna, Course CSL (1999).

[106] B. H. Bransden and C. J. Joachain, *Physics of Atoms and Molecules*, 2nd ed. (Pearson Education Limited, Essex, England, 2003).

[107] M. Weidemüller and C. Zimmermann, eds., *Interactions in Ultracold Gases* (Wiley-VCH, Weinheim, Germany, 2003).

[108] J. M. Hutson and P. Soldán, Int. Rev. Phys. Chem. **25**, 497 (2006).

[109] H. T. C. Stoof, K. B. Gubbels, and D. B. M. Dickerscheid, *Ultracold quantum fields* (Springer, Dordrecht, The Netherlands, 2009).

[110] C. Chin, R. Grimm, P. Julienne, and E. Tiesinga, Rev. Mod. Phys. **82**, 1225 (2010).

[111] H. Friedrich, ed., *Scattering Theory*, 2nd ed. (Springer-Verlag, Heidelberg, Germany, 2016).

[112] C. Strauss, T. Takekoshi, F. Lang, K. Winkler, R. Grimm, J. Hecker Denschlag, and E. Tiemann, Phys. Rev. A **82**, 052514 (2010).

[113] M. Berninger, A. Zenesini, B. Huang, W. Harm, H.-C. Nägerl, F. Ferlaino, R. Grimm, P. S. Julienne, and J. M. Hutson, Phys. Rev. A **87**, 032517 (2013).

[114] T. Weber, J. Herbig, M. Mark, H.-C. Nägerl, and R. Grimm, Science **299**, 232 (2003).

[115] D. J. McCarron, H. W. Cho, D. L. Jenkin, M. P. Köppinger, and S. L. Cornish, Phys. Rev. A **84**, 011603 (2011).

[116] S. L. Cornish, N. R. Claussen, J. L. Roberts, E. A. Cornell, and C. E. Wiemann, Phys. Rev. Lett. **85**, 1795 (2000).

[117] A. L. Marchant, S. Händel, S. A. Hopkins, T. P. Wiles, and S. L. Cornish, Phys. Rev. A **85**, 053647 (2012).

[118] K. E. Strecker, G. B. Partridge, A. G. Truscott, and R. G. Hulet, Nature **417**, 150 (2002).

[119] A. L. Marchant, T. P. Billam, T. P. Wiles, M. M. H. Yu, S. A. Gardiner, and S. L. Cornish, Nature Communications **4**, 1865 (2013).

[120] T. Kraemer, M. Mark, P. Waldburger, J. G. Danzl, C. Chin, B. Engeser, A. D. Lange, K. Pilch, A. Jaakkola, H.-C. Nägerl, and R. Grimm, Nature **440**, 315 (2006).

[121] E. Hodby, S. T. Thompson, C. A. Regal, M. Greiner, A. C. Wilson, D. S. Jin, E. A. Cornell, and C. R. Weiman, Phys. Rev. Lett. **94**, 120402 (2005).

[122] J. M. Hutson, BOUND computer program, version 5, distributed by Collaborative Conputational Project No. 6 of the EPSRC (1993).

[123] J. M. Hutson, FIELD computer program, version 1 (2011).

[124] J. M. Hutson and S. S. Greene, MOLSCAT computer program, version 14, distributed by Collaborative Computation Project No. 6 of the EPSRC (1994).

[125] M. L. González-Martínez and J. M. Hutson, Phys. Rev. A **75**, 022702 (2007).

[126] O. Docenko, M. Tamanis, R. Ferber, H. Knöckel, and E. Tiemann, Phys. Rev. A **83**, 052519 (2011).

[127] C. Chin, V. Vuletić, A. J. Kerman, S. Chu, E. Tiesinga, P. J. Leo, and C. J. Williams, Phys. Rev. A **70**, 032701 (2004).

[128] K. Pilch, A. D. Lange, A. Prantner, G. Kerner, F. Ferlaino, H.-C. Nägerl, and R. Grimm, Phys. Rev. A **79**, 042718 (2009).

[129] H.-W. Cho, D. J. McCarron, M. P. Köppinger, D. L. Jenkin, K. L. Butler, P. S. Julienne, C. L. Blackley, C. R. Le Sueur, J. M. Hutson, and S. L. Cornish, Phys. Rev. A **87**, 010703(R) (2013).

[130] P. D. Gregory, P. K. Molony, M. P. Köppinger, A. Kumar, Z. Ji, B. Lu, A. L. Marchant, and S. L. Cornish, New J. Phys. **17**, 055006 (2015).

[131] K. Bergmann, H. Theuer, and B. W. Shore, Rev. Mod. Phys. **70**, 1003 (1998).

[132] K. Bergmann, N. V. Vitanoc, and B. W. Shore, J. Chem. Phys. **142**, 170901 (2015).

[133] K. Winkler, F. Lang, G. Thalhammer, P. v. d. Straten, R. Grimm, and J. Hecker Denschlag, Phys. Rev. Lett. **98**, 043201 (2007).

[134] L. P. Yatsenko, V. I. Romanenko, B. W. Shore, and K. Bergmann, Phys. Rev. A **65**, 043409 (2002).

[135] K. Aikawa, D. Akamatsu, J. Kobayashi, M. Ueda, T. Kishimoto, and S. Inouye, New. J. Phys. **11** (2009), 10.1088/1367-2630/11/5/055035.

[136] T. Bergeman, C. E. Fellows, R. F. Gutterres, and C. Amiot, Phys. Rev. A **67**, 050501(R) (2003).

[137] W. C. Stwalley, Eur. Phys. J. D **31**, 221 (2004).

[138] S. Kotochigova and E. Tiesinga, J. Chem. Phys. **123**, 174304 (2005).

[139] O. Docenko, M. Tamanis, R. Ferber, T. Bergeman, S. Kotochigova, A. V. Stolyarov, A. d. F. Nogueira, and C. E. Fellows, Phys. Rev. A **81**, 042511 (2010).

[140] P. K. Molony, P. D. Gregory, A. Kumar, C. R. Le Sueur, J. M. Hutson, and S. L. Cornish, Chem. Phys. Chem. (2016), 10.1002/cphc.201600501.

[141] C. E. Fellows, R. F. Gutterres, A. P. C. Campos, J. Vergès, and C. Amiot, J. Mol. Spectrosc. **197**, 19 (1999).

[142] W. Demtröder, *Atoms, Molecules and Photons* (Springer-Verlag Berlin Heidelberg, Germany, 2006).

[143] N. F. Ramsay, Phys. Rev. **85**, 60 (1952).

[144] D. L. Bryce and R. E. Wasylishen, Acc. Chem. Res. **36**, 327 (2003).

[145] J. Aldegunde, B. A. Rivington, P. S. Żuchowski, and J. M. Hutson, Phys. Rev. A **78**, 033434 (2008).

[146] H. Ran, J. Aldegunde, and J. M. Hutson, New J. Phys. **12**, 043015 (2010).

[147] G. Herzberg, *Molecular Spectra and Molecular Structure*, 2nd ed. (D. Van Nostrand Company Inc., 1950).

[148] S. Händel, A. L. Marchant, T. P. Wiles, S. A. Hopkins, and S. L. Cornish, Review of Scientific Instruments **83**, 013105 (2012).

[149] C. L. Blackley, C. R. Le Sueur, J. M. Hutson, D. J. McCarron, M. P. Köppinger, H.-W. Cho, D. L. Jenkin, and S. L. Cornish, Phys. Rev. A **87**, 033611 (2013).

[150] D. J. McCarron, S. A. King, and S. L. Cornish, Measurement Science and Technology **19**, 105601 (2008).

[151] G. C. Bjorklund, Optics Letters **5**, 15 (1980).

[152] J. G. Danzl, M. J. Mark, E. Haller, M. Gustavsson, R. Hart, J. Aldegunde, J. M. Hutson, and H.-C. Nägerl, Nature Physics **6**, 265 (2010).

[153] K. Aikawa, K. Kobayashi, T. Oasa, T. Kishimoto, M. Ueda, and S. Inouye, Optics Express **19**, 14479 (2011).

[154] U. Schünemann, H. Engler, R. Grimm, M. Weidemüller, and M. Zielonkowski, Review of Scientific Instruments **70**, 242 (1999).

[155] M. Debatin, T. Takekoshi, R. Rameshan, L. Reichsöllner, F. Ferlaino, R. Grimm, R. Vexiau, N. Bouloufa, O. Dulieu, and H.-C. Nägerl, Phys. Chem. Chem. Phys. **13**, 18926 (2011).

[156] E. D. Black, American Journal of Physics **69**, 79 (2001).

[157] J. I. Thorpe, K. Numata, and J. Livas, Optics Express **16**, 15980 (2008).

[158] H. J. Metcalf and P. van der Straten, *Laser Cooling and Trapping* (Springer, 2002).

[159] P. Monk, *Finite Element Methods for Maxwell's Equations* (Oxford University Press, UK, 2003).

[160] M. W. Gempel, T. Hartmann, T. A. Schulze, K. K. Voges, A. Zenesini, and S. Ospelkaus, New J. Phys. **18**, 045017 (2016).

[161] OFCOM Frequency Allocation Table, United Kingdom (2013).

[162] A. W. Rudge, K. Milne, A. D. Olver, and P. Knight, eds., *The Handbook of Antenna Design*, 2nd ed., IEE Electromagnetic Waves Series, Vol. 1 and 2 (Peter Peregrinus Ltd., London, UK, 1986).

[163] J. D. Kraus and R. J. Marhefka, *Antennas for All Applications*, 3rd ed. (McGraw-Hill, New York, USA, 2002).

[164] J. Dyson, IRE Transactions on Antennas **7**, 181 (1959).

[165] J. Kaiser, IRE Transactions on Antennas and Propagation **8**, 312 (1960).

[166] T. A. Milligan, *Modern Antenna Design* (John Wiley & Sons, New Jersey, USA, 2005).

[167] M. P. Köppinger, D. J. McCarron, D. L. Jenkin, P. K. Molony, H. W. Cho, S. L. Cornish, C. R. Le Sueur, C. L. Blackley, and J. M. Hutson, Phys. Rev. A **89**, 033604 (2014).

[168] D. Wang, B. Neyenhuis, M. H. G. de Miranda, K.-K. Ni, S. Ospelkaus, D. S. Jin, and J. ye, Phys. Rev. A **81**, 061404(R) (2010).

[169] J. Kobayashi, K. Aikawa, T. Oasa, and S. Inouye, Phys. Rev. A **89**, 021401(R) (2014).

[170] B. E. Londoño, J. Mahecha, E. Luc-Koenig, and A. Crubellier, Phys. Chem. Chem. Phys. **13**, 18738 (2011).

[171] H. Telle, "EP1594020 - Method for generating an offset-free optical frequency comb and laser apparatus therefor," (2005).

[172] P. K. Molony, A. Kumar, P. D. Gregory, R. Kliese, T. Puppe, C. R. Le Sueur, J. Aldegunde, J. M. Hutson, and S. L. Cornish, Phys. Rev. A **94**, 022507 (2016).

[173] K. R. A. Hazzard, A. V. Gorshkov, and A. M. Rey, Phys. Rev. A **84**, 033608 (2011).

[174] A. André, D. DeMille, J. M. Doyle, M. D. Lukin, S. E. Maxwell, P. Rabl, R. J. Schoelkopf, and P. Zoller, Nature Physics **2**, 636 (2006).

[175] J. Aldegunde, H. Ran, and J. M. Hutson, Phys. Rev. A **80**, 043410 (2009).

[176] B. Neyenhuis, B. Yan, S. A. Moses, J. P. Covey, A. Chotia, A. Petrov, S. Kotochigova, J. Ye, and D. S. Jin, Phys. Rev. Lett. **109**, 230403 (2012).

[177] S. A. Will, J. W. Park, Z. Z. Yan, H. Loh, and M. W. Zwierlein, Phys. Rev. Lett. **116**, 225306 (2016).

[178] P. D. Gregory, J. Aldegunde, J. M. Hutson, and S. L. Cornish, Phys. Rev. A **94**, 041403(R) (2016).

[179] C. W. White, W. M. Hughes, G. S. Hayne, and H. G. Robinson, Phys. Rev. **174**, 23 (1968).

[180] C. W. White, W. M. Hughes, G. S. Hayne, and H. G. Robinson, Phys. Rev. A **7**, 1178 (1973).

[181] L. D. Carr, D. DeMille, R. V. Krems, and J. Ye, New J. Phys. **11**, 055049 (2009).

[182] M. A. Baranov, M. Dalmonte, G. Pupillo, and P. Zoller, Chem. Rev. **112**, 5012 (2012).

[183] J. Aldegunde and J. M. Hutson, Phys. Rev. A **79**, 013401 (2009).

[184] S. Kotochigova and D. DeMille, Phys. Rev. A **82**, 063421 (2010).

[185] M. Deiß, B. Drews, B. Deissler, and J. H. Denschlag, Phys. Rev. Lett. **113**, 233004 (2014).

[186] M. Deiß, B. Drews, J. Hecker Denschlag, N. Bouloufa-Maafa, R. Vexiau, and O. Dulieu, New. J. Phys. **17**, 065019 (2015).

[187] M. S. Safronova, B. Arora, and C. W. Clark, Phys. Rev. A **73**, 022505 (2006).

[188] P. D. Gregory, J. A. Blackmore, J. Aldegunde, J. M. Hutson, and S. L. Cornish, Phys. Rev. A **96**, 021402(R) (2017).

[189] S. Kotochigova and E. Tiesinga, Phys. Rev. A **73**, 041405(R) (2006).

[190] R. Vexiau, *Dynamique et contrôle optique des molécules froides*, Ph.D. thesis, Université Paris Sud, Paris (2012).

[191] S. Ospelkaus, K.-K. Ni, M. H. G. de Miranda, B. Neyenhuis, D. Wang, S. Kotochigova, P. S. Julienne, D. S. Jin, and J. Ye, Faraday Discussions **142**, 351 (2009).

[192] Z. Idziaszek and P. S. Julienne, Phys. Rev. Lett. **104**, 113202 (2010).

[193] P. S. Julienne, T. M. Hanna, and Z. Idziaszek, Phys. Chem. Chem. Phys. **13**, 19114 (2011).

[194] M. D. Frye, P. S. Julienne, and J. M. Hutson, New J. Phys. **17**, 045019 (2015).

[195] T. Weber, J. Herbig, M. Mark, H.-C. Nägerl, and R. Grimm, Phys. Rev. Lett. **91** (2003), 10.1103/PhysRevLett.91.123201.

[196] E. A. Burt, R. W. Ghrist, C. J. Myatt, M. J. Holland, E. A. Cornell, and C. E. Wiemann, Phys. Rev. Lett. **79**, 337 (1997).

[197] M. Mayle, B. P. Ruzic, and J. L. Bohn, Phys. Rev. A **85**, 062712 (2012).

[198] M. Mayle, G. Quéméner, B. P. Ruzic, and J. L. Bohn, Phys. Rev. A **87**, 012709 (2013).

[199] J. L. Bohn, A. V. Avdeenkov, and M. P. Deskevich, Phys. Rev. Lett. **89**, 203202 (2002).

[200] J. F. R. Croft and J. L. Bohn, Phys. Rev. A **89**, 012714 (2014).

[201] G. Quéméner, J. L. Bohn, A. Petrov, and S. Kotochigova, Phys. Rev. A **84**, 062703 (2011).

[202] H. Fahs, A. R. Allouche, M. Korek, and M. Aubert-Frécon, J. Phys. B: At. Mol. Opt. Phys. **35**, 1501 (2002).

[203] T. Bergeman, A. J. Kerman, J. Sage, S. Sainis, and D. DeMille, Eur. Phys. J. D **31**, 179 (2004).

[204] A. V. Gorshkov, P. Rabl, G. Pupillo, A. Micheli, P. Zoller, M. Lukin, and H. P. Büchler, Phys. Rev. Lett. **101**, 073201 (2008).

[205] W. Lechner and P. Zoller, Phys. Rev. Lett. **111**, 185306 (2013).

[206] A. W. Glaetzle, M. Dalmonte, R. Nath, I. Rousochatzakis, R. Moessner, and P. Zoller, Phys. Rev. X **4** (2014), 10.1103/PhysRevX.4.041037.

[207] F. Cinti, T. Macrí, W. Lechner, G. Pupillo, and T. Pohl, Nature Communications **5**, 3235 (2014).

[208] K. R. A. Hazzard, S. R. Manmana, M. Foss-Feig, and A. M. Rey, Phys. Rev. Lett. **110**, 075301 (2013).

[209] J. P. Covey, S. A. Moses, M. Gärttner, A. Safavi-Naini, M. T. Miecnikowski, Z. Fu, J. Schachenmayer, P. S. Julienne, A. M. Rey, D. S. Jin, and J. Ye, Nature Communications **7**, 11279 (2016).

[210] S. A. Moses, J. P. Covey, M. T. Miecnikowski, D. S. Jin, and J. Ye, Nature Physics **13**, 13 (2016).

[211] L. Reichsöllner, A. Schindewolf, T. Takekoshi, R. Grimm, and H.-C. Nägerl, Phys. Rev. Lett. **118**, 073201 (2017).

[212] M. P. Köppinger, P. D. Gregory, D. L. Jenkin, D. J. McCarron, A. L. Marchant, and S. L. Cornish, New J. Phys. **16**, 115016 (2014).

[213] S. L. Kemp, K. L. Butler, R. Freytag, S. A. Hopkins, E. A. Hinds, M. R. Tarbutt, and S. L. Cornish, Rev. Sci. Instrum. **87**, 023105 (2016).

[214] S. A. Hopkins, K. L. Butler, A. Guttridge, S. Kemp, R. Freytag, E. A. Hinds, M. R. Tarbutt, and S. L. Cornish, Rev. Sci. Instrum. **87**, 043109 (2016).

[215] R. K. Hanley, P. D. Gregory, I. G. Hughes, and S. L. Cornish, J. Phys. B: At. Mol. Opt. Phys. **48**, 195004 (2015).

[216] N. Schlosser, R. Georges, I. Protsenko, and P. Grangier, Nature **411**, 1024 (2001).

[217] T. Grünzweig, A. Hilliard, M. McGovern, and M. F. Andersen, Nature Physics **6**, 951 (2010).

[218] L. R. Liu, J. T. Zhang, Y. Yu, N. R. Hutzler, Y. Liu, T. Rosenband, and K. K. Ni, arXiv:1701.0312v1 (2017).

[219] EPSRC Grant Ref: EP/P01058X/1, Quantum Science with Ultracold Molecules (QSUM) (2017).

[220] W. S. Bakr, J. I. Gillen, A. Peng, S. Fölling, and M. Greiner, Nature **462**, 74 (2009).

[221] C. Weitenberg, M. Endres, J. F. Sherson, M. Cheneau, P. Schauß, T. Fukuhara, I. Bloch, and S. Kuhr, Nature **471**, 319 (2011).

[222] J. F. Sherson, C. Weitenberg, M. Endres, M. Cheneau, I. Bloch, and S. Kuhr, Nature **467**, 68 (2010).

[223] W. S. Bakr, A. Peng, M. E. Tai, J. Simon, J. I. Gillen, S. Fölling, L. Pollet, and M. Greiner, Science **329**, 547 (2010).

[224] M. Endres, M. Cheneau, T. Fukuhara, C. Weitenberg, P. Schauß, C. Gross, L. Mazza, M. C. Bañuls, L. Pollet, I. Bloch, and S. Kuhr, Science **334**, 200 (2011).

[225] M. Cheneau, P. Barmettler, D. Poletti, M. Endres, P. Schauß, T. Fukuhara, C. Gross, I. Bloch, C. Kollath, and S. Kuhr, Nature **481**, 484 (2012).